AN ABSTRACT OF THE THESIS OF

Fernando Martin-Bandin for the degree of Master of Science in Radiation Health Physics presented on August 3, 1995. Title: Environmental Assessment of Soils Contaminated with ^{238}U and/or ^{90}Sr Via Scintillation Technology: Fernald Incinerator Site - A Case Study.

Redacted for Privacy

Abstract approved: _____

Jack F. Higginbotham

A method for the rapid characterization of surface soils containing ^{238}U and ^{90}Sr has been developed and demonstrated at the Fernald Incinerator Site. The method employs an in situ scintillation detector prototype and a geostatistical assessment technique. The method aims were threefold: 1) observing the high-energy beta particles originating from the decay daughters of ^{238}U and ^{90}Sr, 2) estimating the specific levels of ^{238}U and ^{90}Sr contamination of the site on a real time basis, and 3) evaluating the detector performance in the field by comparing its results with more accurate ones obtained by laboratory analysis. Furthermore, independent laboratory investigations were conducted with the prototype at the Oregon State University Radiation Center.

The first part was accomplished through the development of a portable detector which has flat ribbons that are each composed of square scintillating fibers. These ribbons are stacked in bundles, and each bundle is coupled to two photomultiplier tubes. Its associated electronic circuitry measures both interlayer and intralayer coincident events, and thus discriminates between the highly energetic betas of interest and those of lower energy. The second and third parts were achieved by applying a geostatistical analysis based on ordinary kriging estimators to both field and laboratory collected data. Both field and laboratory results showed similar trends, which helped to verify accurate detector performance.

The detector prototype response was found to be linear for the high-energy betas of ^{238}U and ^{90}Sr, and quasi-linear for the intermediate-energy emitter ^{154}Eu. Its high-energy beta sensitivity is as low as 0.5 pCi/g. Systematic fluctuations were observed in the first three detector counts of each set of measurements.

The developed method has the unique advantage of determining concentrations of high-energy beta contaminants on a real-time basis. Its disadvantages are the impossibility of discriminating between ^{238}U and ^{90}Sr and the difficulty of assessing the system's reliability and risk associated with its estimates.

Environmental Assessment of Soils Contaminated with ^{238}U and/or ^{90}Sr Via Scintillation
Technology: Fernald Incinerator Site - A Case Study

by

Fernando Martin-Bandin

A THESIS

submitted to

Oregon State University

in partial fulfillment of
the requirements for the
degree of

Master of Science

Completed August 3, 1995
Commencement June 1996

Master of Science thesis of Fernando Martin-Bandin presented on August 3, 1995

APPROVED:

Redacted for Privacy

Major Professor, Representing Radiation Health Physics

Redacted for Privacy

Chair of Department of Nuclear Engineering

Redacted for Privacy

Dean of Graduate School

I understand that my thesis will become part of the permanent collection of Oregon State University libraries. My signature below authorizes release of my thesis to any reader upon request.

Redacted for Privacy

Fernando Martin-Bandin, Author

ACKNOWLEDGEMENTS

TABLE OF CONTENTS

TABLE OF CONTENTS (Continued)

TABLE OF CONTENTS (Continued)

LIST OF FIGURES

LIST OF FIGURES (Continued)

LIST OF TABLES

Environmental Assessment of Soils Contaminated with ^{238}U and/or ^{90}Sr Via Scintillation Technology: Fernald Incinerator Site - A Case Study

1. INTRODUCTION

The characterization and subsequent cleanup of surface soils exhibiting radioactive contamination in excess of established limits are becoming increasingly important and pose a technological challenge without an existing solution. Before any effective remedial protocol is established, a rapid and reliable method must be developed for the measurement of ^{238}U and ^{90}Sr in soils.

In response to this need for a faster characterization method, a portable detector composed of square plastic scintillating fibers has been developed and used directly on the contaminated soil of the Fernald Incinerator Site by Battelle Pacific Northwest Laboratory. The detector counts, on a real-time bases, high-energy beta particles that originate from the decay chains of ^{238}U and ^{90}Sr.

Beta-radiation dispersion data in large extensions of soils generally show the following features: 1) a highly irregular geographic distribution, 2) susceptibility to inaccurate measurements, mostly through sampling errors; 3) reference to poorly defined areas; 4) presence of outliers, whose identification may have especial radiological interest.

The advantage of beta over gamma detection systems for the purpose of soil characterization is significant. Usually gamma-ray detection is slower because of the inherent features of the equipment associated with this type of radiation detection. Gamma spectroscopy at the Fernald Site, for example, took about 2 months.

Traditional techniques for the quantitative characterization of radionuclide-contaminated soils over extended areas are often burdensome, cost prohibitive and sometimes inaccurate. In addition, these techniques are based on the detection of the gamma-ray emissions. Such methods include in-situ gamma-ray spectrometry [1.1], or areal surveys using NaI(Tl) or HPGe gamma-ray sensors for uranium detection [1.2], and hand sampling followed by gamma-ray counting or extensive radiochemistry and subsequent beta-particle counting [1.3].

1.1 The radiation detection problem

The beta-radiation-detection problem can be stated from: 1) how to efficiently detect high-energy beta radiation from radioactively contaminated soils while discriminating against cosmic and gamma radiations and 2) how to discriminate between different beta emitters such as ^{238}U and ^{90}Sr that might be mixed in the soil. With current technology, detectors cannot discriminate between ^{238}U and ^{90}Sr contaminants since they emit beta particles of similar end point energies (2.29 and 2.28 MeV respectively): the detector response functions for these two radionuclides are virtually identical.

To partially solve the problem, a scintillation detector prototype has been designed to work simultaneously on a triple-coincidence and anticoincidence modes. This mechanism is provided to ensure respectively that the high-energy beta particles are detected, and that cosmic-induced electromagnetic radiation or Compton electrons generated by the interaction of gamma rays with the detector are rejected. Only high-energy beta particles will interact to produce a three-coincidence count, and gamma rays that either interact with the anti-coincidence layer or do not interact simultaneously with the three-coincidence layers are discarded. This phenomenon would be manifested by simultaneous light output in each of the three coincidence layers and anti-coincidence layer.

Energy resolution capability would be desirable for a better site characterization. An analysis will be furnished in this work to investigate ways to provide the detector prototype with energy resolution capabilities while preserving the current design as much as possible (see section 7.1).

The basis for the scintillation process is to efficiently convert the kinetic energy of charged particles into detectable and measurable, visible light. However, not every type of produced visible light is desirable. A good scintillator would convert as large a fraction as possible of the incident radiation into prompt fluorescence (no delayed fluorescence), and would minimize the contributions of phosphorescence.

The scintillation fibers are optically coupled to a set of photomultiplier (PM) tubes to convert the weak scintillation pulses into an amplified electrical signal without adding large amounts of random noise [2.2]. Actions such as the replacement of PM tubes by photodiodes would serve the purpose of reducing this random noise. The reason for this replacement would be threefold: recent advances in the development of semiconductors [1.4 and 1.5], their higher quantum efficiency and their good advantage in energy resolution and coincidence applications.

The present prototype could be modified to operate in a quadruple-coincidence mode by adding a fourth scintillation layer to supposedly improve the beta detection sensitivity (see section 7.3). It would result in a more complex design for it would need two more PM tubes to work simultaneously with the other already existing tubes, adding instability and more weight to the detector.

The detector accuracy, stability and data reproducibility is to be investigated. The data collected with the detector have to be compared to other more accurate ones such as hand sampling and later laboratory analysis. The reproducibility can be investigated by revisiting fixed specific field locations throughout the course of the sampling campaign and comparing detector output as a function of time and environmental conditions. Its stability can be determined by running the detector several days under fixed environmental conditions and characterizing the detector response versus temperature and humidity.

1.2 Nature of beta and gamma radiations

Beta particles dissipate their energy continuously in a sequence of ionizations, excitations and scattering collisions with electrons and nuclei. They penetrate a certain distance, the range, into the absorber while depositing energy into the medium. Electromagnetic radiations, on the other hand, are absorbed or scattered in single events, and their energy dissipation is discontinuous (as opposed of those of charged particles). ^{234m}Pa and ^{90}Y each decay via the emission of a 2.3-MeV maximum-energy beta particle with 0.98 and 1 branching ratios respectively. When travelling normally

incident to the detector face at their most probable energy (approximately 800 keV), these betas of the decay chains of the ^{238}U and ^{90}Sr would be expected to penetrate roughly 3 mm of plastic scintillator (figure 1.2). Figure 1.1 illustrates the possible interactions between incident radiation and the scintillation material of the detector.
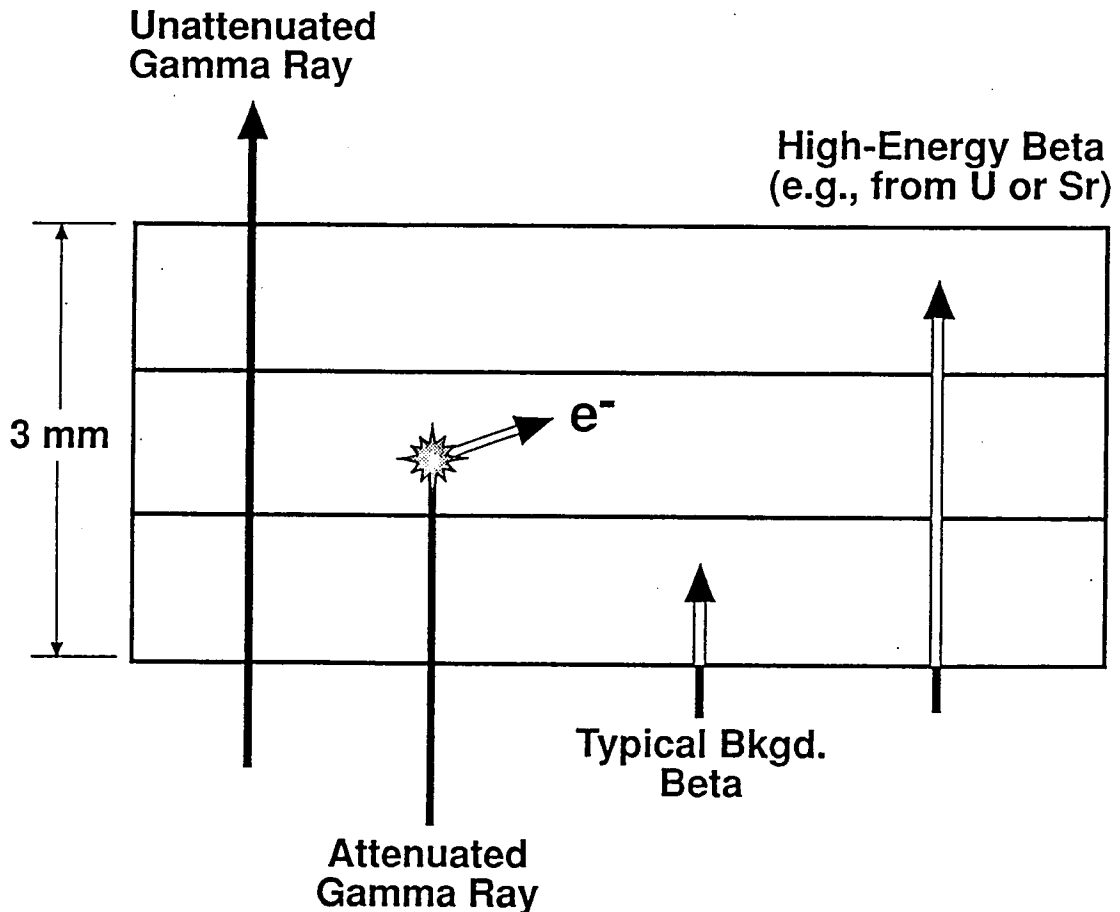
Figure 1.1 Diagram simplification of the detector's basis showing the possible interactions between the scintillation material and incident beta particles and gamma rays [1.6]. Double lines denote particle tracks that lead directly to excitations and/or ionizations and consequent scintillations.
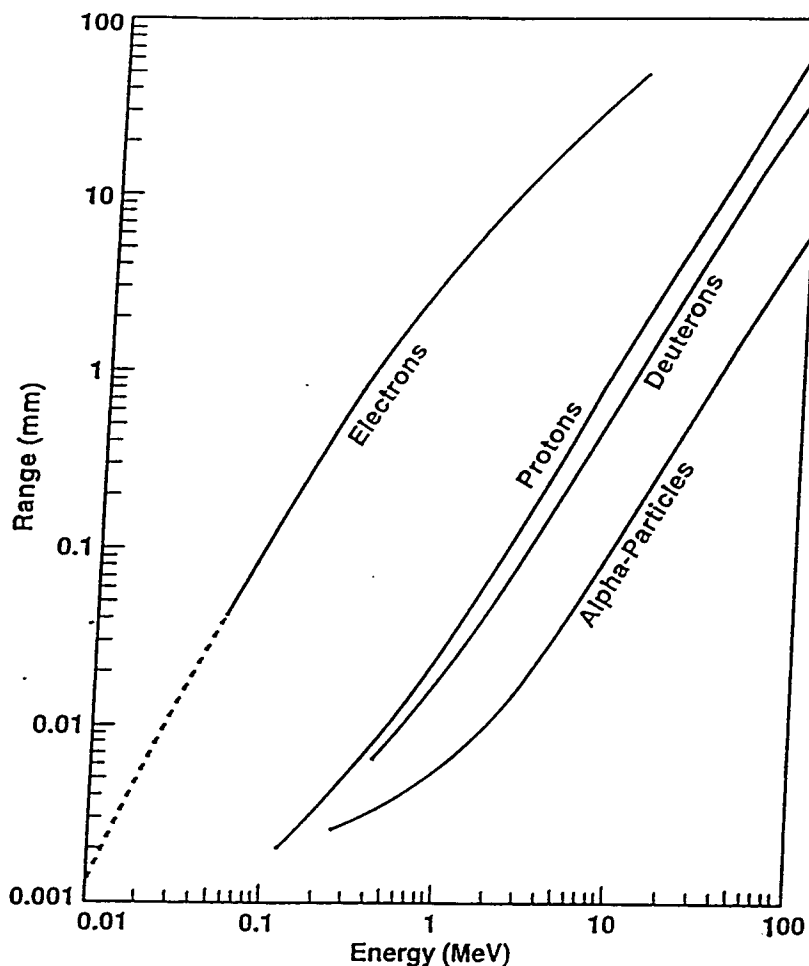
Figure 1.2 Plot of the penetration depths (range) of various charged species in scintillant plastic as a function of their energy (courtesy of BICRON Corporation, Newbury, Ohio).

1.3 The statistics problem

The problem of accurately estimating the activity distribution of a contaminant in a large extention of land, when only a limited set of samples has been obtained, is a difficult one. The limited number of samples that can be taken poses a problem which is even enlarged by the additional lack of information on the accuracy of the developing detector. It would be excessively costly and time consuming to sample the whole site's area. To solve this problem, an operative probabilistic modeling based on the spatial distribution of the radioactive contamination is to be implemented. The

optimal estimation of the spatial distributions is a formidable task to accomplish due to geostatistical considerations such as the occurrence of local and global trends, pockets of high and low radioactive pollution levels, correlated data, skewed data sets and insufficient data collection. Other factors such as soil humidity levels, soil grain size, existence of grass or sagebrushes on the surface soil and the heating of the detector components (due to high weather temperatures) add more complexity into the data analysis.

Most classical techniques to analyze an observed set of data are based on the assumption that the observed data are samples from a random function that can be represented by polynomials, and with no regard for spatial position. Any deviation from these polynomial functions are assumed to be random errors. However, this assumption is frequently violated for radioactive contamination in the environment [1.7]. Besides, it is reasonable to make estimates that take into account that nearby data points must have more influence on the estimate that data farther away. However, this type of estimate requires that the assumption of random errors be rejected, and thus eliminates most classical methods.

One way to deal with the problem of random errors is to use deterministic interpolation functions that are forced throughout the data values. However a deep knowledge of the physics of radionuclide distribution in soils is needed to permit a deterministic approach to estimation. The resulting functions are quite fluctuating, and the accuracy of the estimates is questionable since there is no objective way to measure the reliability of the interpolated estimates. Another way of tackling the problem is to use more lenient statistical assumptions and implement a more fitting-to-reality estimator by using probabilistic models.

1.4 Geostatistics and kriging

Methods based on the assumption that the covariance of the data values at their locations is a function of their space distribution have been applied with success in a variety of different situations. Such methods involve spatially distributed quantities

that could be possible outcomes of a random variable. Examples include mining [1.8], ground water studies [1.9], gene frequency mapping [1.10], acid rain deposition [1.11], air quality data [1.12], and radionuclide distribution over space [1.13]. The application of these methods which are based on the theory of regionalized variables and correlated data is the conceptual foundation of geostatistics, and it has been shown that distribution of the radionuclides in the environment could be evaluated by such a method [1.13, 1.14].

Geostatistics is concerned with the study of phenomena that fluctuate in space or time. It then consequently offers a collection of deterministic and statistical tools aimed at understanding, modeling, and predicting. One of the methods that geostatisticians have been using since 1971 is the kriging estimator [1.15] (see section 4.3). It is based on the assumption that the variance of the difference between the data values at two points is a function of the distance between them. Thus the kriging estimator of the contamination level at a point x_o in geographical space is given by the following linear function

$$\hat{z}(x_o) = \sum_{i=1}^{n} \lambda_i z(x_i)$$

where $z(x_i)$ is the observed datum at the point x_i within a local neighborhood about the point x_o, and λ_i is the weight attached to that datum. The weights, λ_i, are selected to make the kriging estimator be a best linear unbiased estimator (B.L.U.E.). This kriging estimator is unbiased since it tries to have the error equal to 0, and it is the best because it aims at minimizing the error variance.

The independence of kriging on data values makes that outlayered values do not significantly affect the estimate, a problem with some other methods. Kriging requires that the underlying correlation structure of the data be estimated and modeled. This structure, shaped in the variogram function (see section 4.4), is used to obtain the weights, λ_i, for use in the above equation. Thereby, estimating the variogram is a very important aspect of kriging and it is difficult, especially if data are highly skewed.

An accurate qualifying mapping of the radioactive material concentrations within a potentially hazardous contaminated site is fundamental to the characterization of the site. The mapping requires the knowledge of the geographical distribution of the contamination within the study site. The use of geostatistics will accurately produce estimators to generate contamination concentration maps within the reference site. The resulting map will likely be underestimated in areas of high contamination levels and overestimated in areas of low levels. But the most severe limitation of this mapping lies in the difficulty of assessing its reliability and the risk associated to its estimates.

1.5 References

1.1   Schilk A.J., Perkins R. W., Abel K. H., and Brodzinski R. L., April 1993.
        "Surface and Subsurface Characterization of Uranium Contamination at the
        Fernald Environmental Management Site." PNL-8617/UC-606, Pacific
        Northwest Laboratory, Richland, Washington.

1.2   Siemon K., Esterlund R. A.,Van Aarle J., Knaack M., Westmeier W. and
        Patzelt P., 1992. "A New Measurement of the Gamma-Ray Intensities of ^{234m}Pa
        Accompanying the Decay of ^{238}U." Appl. Radiat. Isot. Vol. 43, No.7, 873-880.

1.3   Miller K. M. and Helfer I. K., 1985. "In Situ Measurements of ^{137}Cs Inventory
        in Natural Terrain." Environmental Measurements Laboratory, U. S.
        Department of Energy, 376 Hudson St., New York, NY 10014.

1.4   Knoll G. F., 1989. "Radiation Detection and Measurement."   Chapter 11.
        John Wiley & Sons.

1.5   Sakai E., Febuary 1987. "Recent Measurements on Scintillator-Photodetector
        Systems."   IEEE Transactions on Nuclear Science, Vol. NS-34, No. 1, 418.

1.6   Schilk A. J., Knopf M. A., Thompson R. C., Hubbard C. W., Abel K. H.,
        Edwards D. R., Abraham J. R., 1993. "Real-Time, In Situ Detection of ^{90}Sr and
        ^{238}U in Soils Via Scintillating-Fiber-Sensor Technology." Unpublished. Pacific
        Northwest Laboratory, P. O. Box 999, Richland, Washington 99352.

1.7   Barnes M. G., 1978. "Statistical Design and Analysis in the Cleanup of
        Environmental Radionuclide Contamination", Desert Research Institute,
        University of Nevada System, NVO 1253-12.

1.8   David M., 1977. "Geostatistical Ore Reserve Estimation." Elsevier Publishing
        Company. New York.

1.9   Delhomme, J. P., 1978. "Kriging in the Hydrosciences", Advances in Water
        Resources 1, 251-266.

1.10   Piazza A., Menozzi P., and Cavalli-Sforza, L, 1981. "The Making and Testing
        of Geographic Gene-Frequency Maps", Biometrics 37, 635-659.

1.11   Eynon B. and Switzer, P., 1982. "The Variability of Rainfall Acidity", SIMS
        Technological Report No. 58. Department of Statistics, Stanford University,
        Stanford, CA.

1.12   Grivet C.D., 1980. "Modeling and Analysis of Air Quality Data", SIMS
        Technical Report No. 43, Department of Statistics, Stanford University,
        Stanford, CA.

1.13   Barnes M. G., 1980. "The Use of Kriging for Estimating the Spatial
        Distribution of Radionuclides and other Spatial Phenomena", TRAN-STAT:
        Statistics for Environmental Studies, No. 13. Pacific Northwest Laboratory,
        Richland, WA. PNL-SA-9051.

1.14   Gilbert R. O., 1985. "Kriging for Estimating Spatial Pattern of Contaminants:
        Potential and Problems", Environmental Monitoring and Assessment
        No. 5, 113-135.

1.15   Royle A., Clark I., Brooker P. W., Parker H., Journel A., Rendu J. M.,
        Sandefur R., Grant D. C., and Mousset-Jones P., 1980. "Geostatistics"
        Chapter 1. McGraw-Hill, Inc. New York, N. Y.

2. DETECTION SYSTEM

2.1 Detector bases

The developing detector has been conceived to only count high-energy beta particles. Based on scintillation technology, it is equipped with three layers of a plastic fiber (low-Z detector material), 1-mm thick each, which will be able to completely absorb high-energy beta radiation and operate in a triple-coincidence mode, figure 1.2. An anti-coincidence layer of equal material and thickness is also arranged on the top of the stacked scintillating layers and absorber to detect cosmic radiation and to operate in anti-coincidence mode.

The detector operates on the basis that secular equilibrium exists between the parent radionuclide (^{238}U or ^{90}Sr) and its daughter (^{234m}Pa or ^{90}Y), and therefore indirectly detects uranium and strontium activities by counting the beta events coming from their daughters in the following chain equilibrium:

$$^{238}\text{U} \ (4.5 \times 10^9 \text{y}) \longrightarrow \ ^{234}\text{Th} \ (24.1 \text{ d}) \longrightarrow \ ^{234m}\text{Pa} \ (1.17 \text{ m}) \ .... \ ... \longrightarrow \ ^{206}\text{Pb} \ (\text{stable})$$

$$^{90}\text{Sr} \ (29.1 \text{ y}) \longrightarrow \ ^{90}\text{Y} \ (2.7 \text{ d}) \longrightarrow \ ^{90}\text{Zr} \ (\text{stable})$$
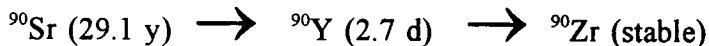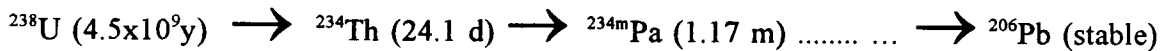
The secular equilibrium would be expected at about a time equal to seven times the half life of the species ^{234}Th and ^{90}Y. In the case of strontium-yttrium, this would occur within three weeks following initial production. Such a condition would not occur until 5 or 6 months later for the uranium-protactinium case due to the long-lived (compared to the half life of ^{234m}Pa) intermediary, ^{234}Th. With regard to the Fernald Incinerator Site, the assumption of secular equilibrium is legitimate, and the detected activity of the daughter is essentially equivalent to that of the parent isotope. This technology is not accurate when potential disequilibria exist between the parent and the daughter species.

A beta particle of high-energy dissipates its energy continuously along its way, and it will consequently score in the three layers, causing a triple-coincidence event. Lower-energy beta particles arising from natural sources such as ^{238}U daughters, ^{232}Th and its daughters, or ^{40}K will not cause triple-coincidence events due to their lower penetration power since their energy rarely exceeds 350 keV. Compton electrons that might be generated in one of the three layers will not score in all three, and thus the detector will allow discrimination against them. The photoelectric effect is virtually non-existent in solid hydrocarbons (plastic fiber). Cosmic radiation is screened out and discriminated by scoring in the anti-coincidence layer. Gamma radiation from the underlying soil will unlikely result in triple-coincidence events.

The final design thus includes three 1-mm layers and a bottom 0.5-mm layer as it is shown in figure 2.1. The bottom 0.5-mm-thick layer mitigates the effect of false signals generated by the production of particular energetic electrons in the first layer that could cause triple-coincidence events.

This three-layer design serves simply and accurately the purpose of counting highly energetic beta particles. A two-layer design would result in insufficient beta detection efficiency since the chances of counting Compton electrons would be much larger. Four layers would result in the loss of beta particles that cannot produce quadruple-coincidence events because of their insufficient angle of incidence. Its complex design would generate a more disadvantageous signal-to-noise ratio [2.1].

2.2 Photoconversion system

The weak prompt fluorescence generated in the scintillation fibers by the incident radiation energy must be converted into a measurable electrical signal. This goal is met by coupling the scintillation material to photomultipliers (PM). However, in the conversion process a random noise [2.2] is generated by the PM tubes which limits the detector sensitivity. This random noise is significant enough to mask certain levels of radiation pulses, and therefore it would degrade the efficiency and sensitivity capabilities of the detection system.
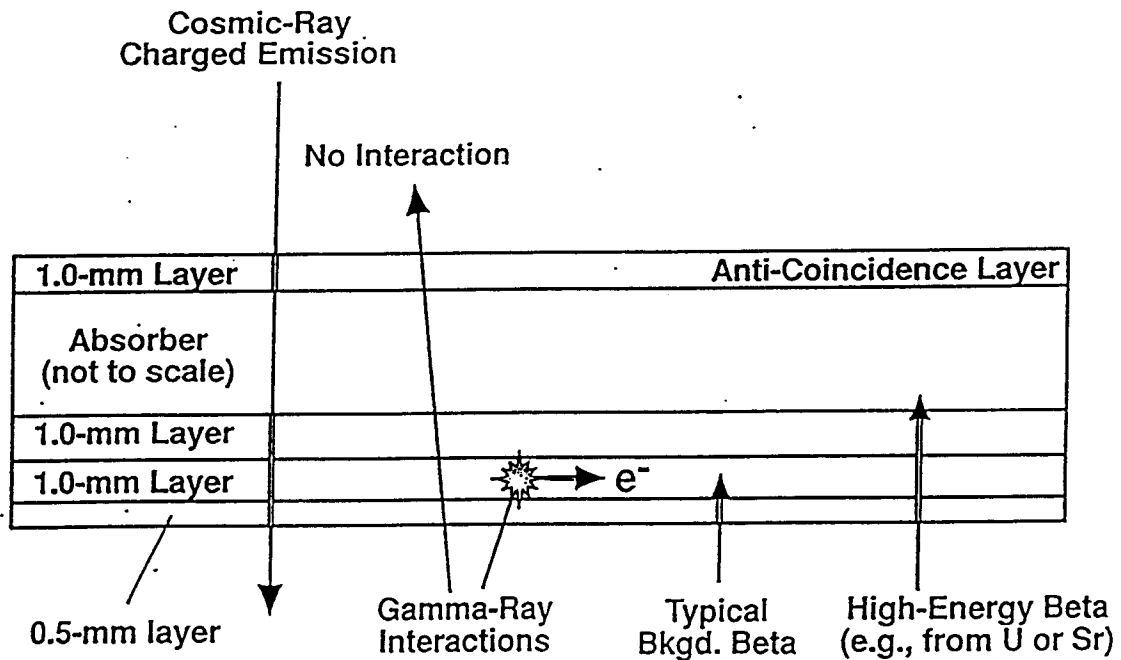
Figure 2.1 Schematic representation of the current detector prototype design highlighting potential interactions [1.6]. Double lines denote particle tracks that lead directly to excitations or ionizations and consequent scintillations.

To partially correct random-noise-related problems, the detector has been equipped, as part of its associated electronic circuitry, with a differentiator device that allows discriminating between the valid signal and that of the random noise of the PM tubes. Nonetheless, there is an inherent noise that still influences the detection sensitivity and cannot be suppressed.

The PM tubes are designed to operate at a high gain which is obtained by application of high-voltage sources (1,500 V). These sources can cause additional stability-related problems and the PM tubes gain could oscillate during the course of measurements. To detect one beta event, the 8 PM tubes must fire at once, or at least six simultaneously when no other type of radiation but high-energy beta is present. Therefore, stability-related problems in a set of 8 PM tubes, that are to work synchronously, would be likely.

2.3 The detection equipment

The current detector with an active area measuring 40 cm by 60 cm has three important parts: scintillation fibers, photoconversion system and electronic circuitry. Part of the detector circuitry is in charge of filtering the random noise of the photomultipliers and amplifying its output signal. Additionally, a 18-V battery supplies power to the detector electronics.

The detection system employs a vertical stacked configuration of scintillating fiber ribbons of plastic (figure 2.1). A 6-mm thick acrylic absorber between the triple stack and the anti-coincidence layer ensures that no energetic charged species originating from the underlying source can reach the uppermost layer and thereby be discarded. The ribbons are milled flat in layers, and each layer is coupled to two PM tubes, one at each end. Four scintillating layers are arranged in a stack and 8 PM tubes connected to them. This assembly of stacked layers and PM tubes forms a unit or module, and two similar modules form the active area of the detector.

This equipment is to be used in field applications. It has to be portable and thus as light and robust as possible. It may endure rough and careless transportation handling, or adverse weather conditions such as high temperatures or rain. The detector equipment will lay for hours in the open when the characterization of a site takes place, and will overheat when overexposed to the sunlight. Humidity, rain and soil vegetation will act as beta radiation attenuators, and therefore measurements performed in these conditions are not representative of the contamination levels.

2.4 References

2.1   Gillespie A. B., 1953. "Signal, Noise and Resolution in Nuclear Counter Amplifiers." Pergamon Press, London.

2.2   Knoll G. F., 1989. "Radiation Detection and Measurement." John Wiley & Sons. Chapter 9, p. 268.

3. EXPLORATORY DATA ANALYSIS

Becoming familiar with the data is of a paramount significance in the starting phase in any geostatistical study. To start with, the origin of the data should be thoroughly investigated. It should be clear understood how the data were assembled into the final form which will be used in the study. Such initial information can be very helpful in avoiding pitfalls in the succeeding analysis. Often a good feel for the spatial arrangement of the data can be obtained from a data posting. Preliminary contour maps can indicate highs, lows and trends. Simple statistics will indicate the nature of the sample distribution; it will assist in the investigation of the distribution behavior. These are important points to consider, because the impressions formed in this preliminary phase will influence the statistical methodology of the study.

3.1 The sampling campaign

The site selected for the demonstration of the current detector was the large field north of Fernald's incinerator facility (figure 3.1) where existing surface contamination is primarily the result of southwesterly prevailing-wind-directed stack emissions from the incineration of uranium-contaminated combustibles.

The sampling campaign originated two types of data: those obtained in situ by setting the developing detector directly on the soil surface, and those obtained by extensive soil hand sample and subsequent laboratory analyses (some times referred to as hand collected data) performed by Fernald personnel. The former took a few days to be collected and was partially delayed due to the existing wet environmental conditions during the demonstration. These data were given to the author of this work by Battelle Pacific Northwest Laboratory for later analysis. The latter was obtained by Fernald personnel after almost two months of efforts.

3.1.1 In situ field sampling

The reference site, Fernald Incinerator Site, was sampled over a rectangular area, 93.87 m (308 feet) in the north direction and 112.16 m (368 feet) in the east, totaling approximately 10,000 m², with the incinerator located in the lower left corner of the rectangle, (Figures 3.1 and 3.2). Sample locations were chosen at a quasi-regular grid spacing of 9.14 m (30 feet) because of the interferences created by a local traversing road and the presence of an electricity tower.
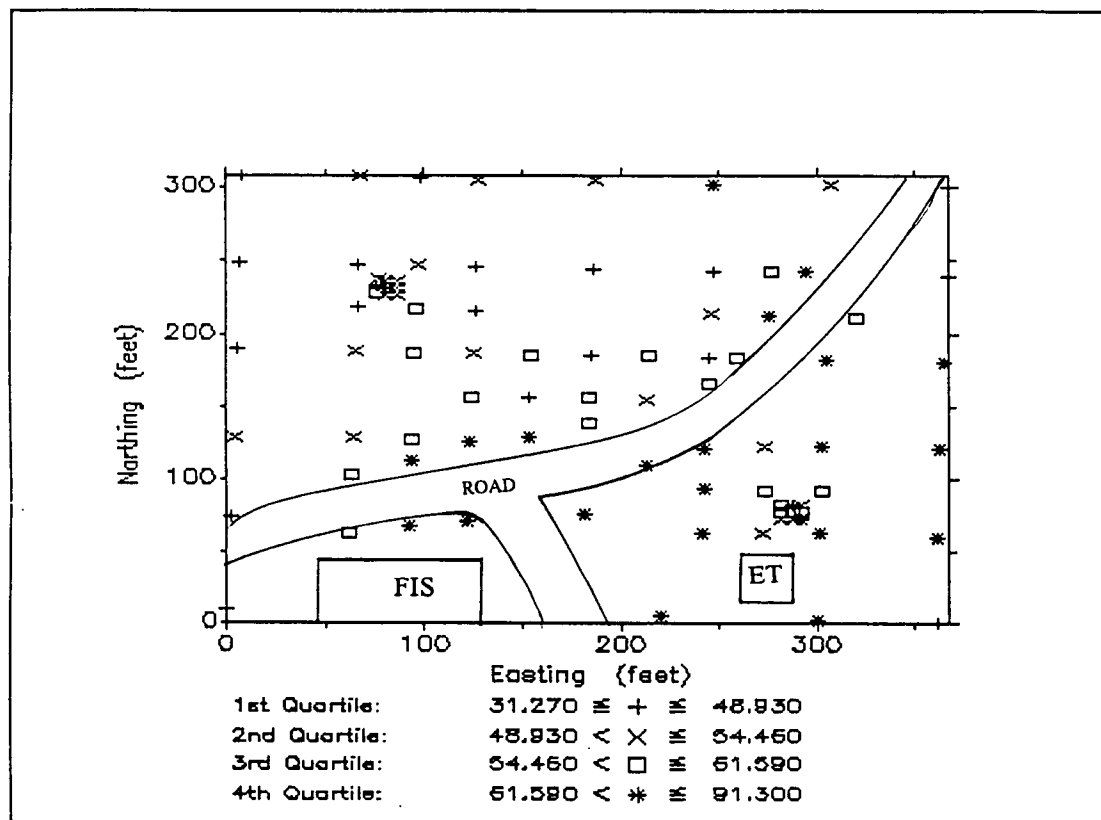
Figure 3.1 Posting of the collected 86-site data. Sample values are posted in pCi/g of ^{238}U and ^{90}Sr. FIS and ET stand for Fernald Incinerator Site and electricity tower respectively.

The number of samples collected during the campaign with the detector was 86. Not included in the sampled lot, were a set of practiced measurements in two different field locations to investigate the reproducibility of the detector. Note the existence, figure 3.1, of some clustered data about the left upper corner and right lower corner. Figure 3.2 is the posting of the laboratory obtained data (or hand data) once the declustering was performed.
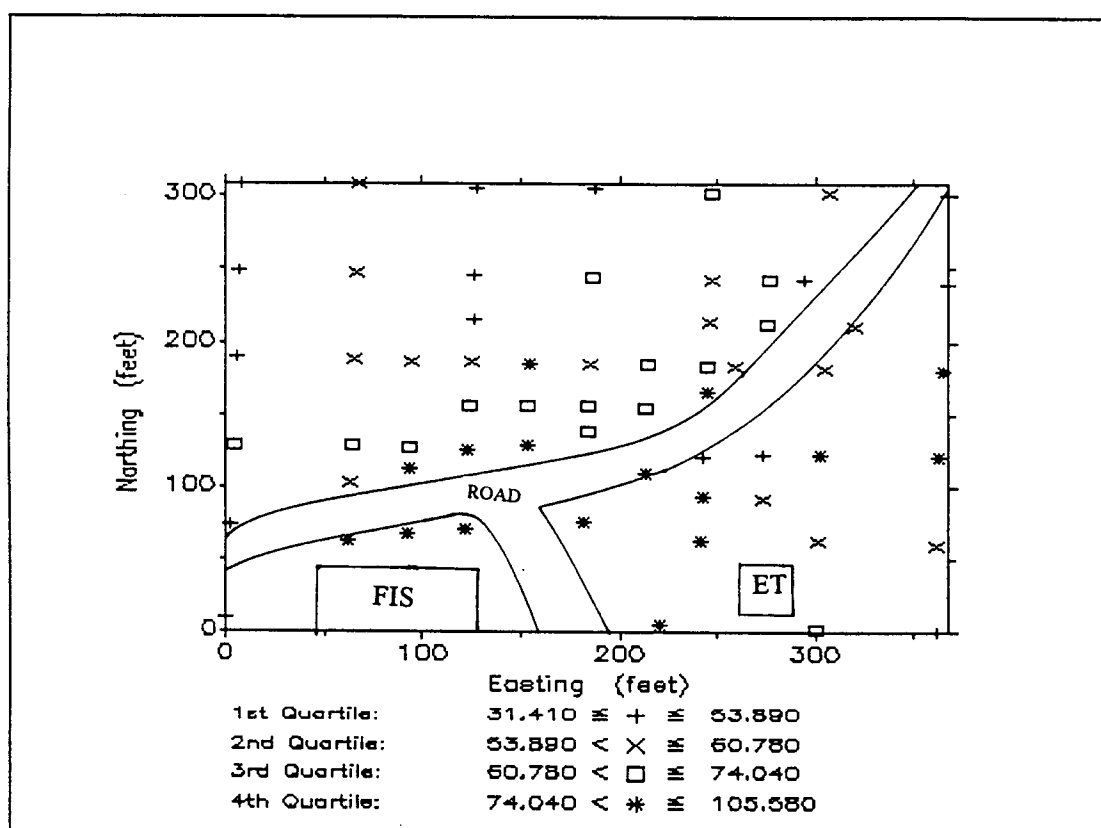
Figure 3.2 Posting of the hand collected data after declustering. Sample values are posted in pCi/g of ^{238}U and/or ^{90}Sr. FIS and ET are the incinerator facility and the electricity tower respectively.

The detector was placed directly on the soil surface and counts were initiated for 15 minutes at each sample location. The surface vegetation was cropped to within 5 cm prior to the campaign to let the detection equipment closer to the soil target.

Calibration standards were produced at the Fernald facility by spiking large aliquots of local soils and homogenizing them by mechanical-mixing process. Additionally, these aliquots served the purpose of demonstrating detector reproducibility.

3.1.2 Laboratory analysis sampling

Samples of 20-cm-deep cores were performed at the same sample locations by Fernald personnel in support of this project. Each core was homogenized before being run through the laboratory. As part of the effort, five of the 20-cm-deep-core samples were randomly selected and split into four equal increments of approximately 5-cm deep. The succeeding inspection of the results ensures that: first, the distribution of the contamination is mostly located on the surface soil, and second the specific activity of the contaminants decreases as depth in the core sample increases. Both in situ detector and laboratory analysis collected data are listed in appendix 1. In situ collected data, as showed in appendix 1, are the processed raw data.

3.2 Univariate statistics

In order to infer the univariate statistics or histogram of the contaminant concentrations within the reference site, it has to be ensured that the sample is not a biased representation of the parent population. For instance there were 86 original data (multiple-coincidence events are measured by the detector in count units) which were transformed into a new set of 86 data in pCi/g units. About 25 % of the collected data are considerably closer to one another that the average grid spacing of 30 feet, and this suggests the possibility of some spatial clustering within the data. This could imply that the lower concentrations are overrepresented by the 86 sample data and, unless this is corrected for, the estimate of the underlying histogram will be biased. Nonetheless, in this case the difference between the clustered and declustered data is not remarkable as can be seen in figures 3.3 and 3.5 respectively. Figure 3.3

shows a histogram of the whole set of data (86). The distribution is almost symmetric about the mean as coefficient of variation, 0.19, and skewedness, 0.538, show. Additionally the mean and median are close as their values are 56.172 and 54.490, respectively. Hence, the spread of radioactive contamination at the Fernald Site is well-behaved.
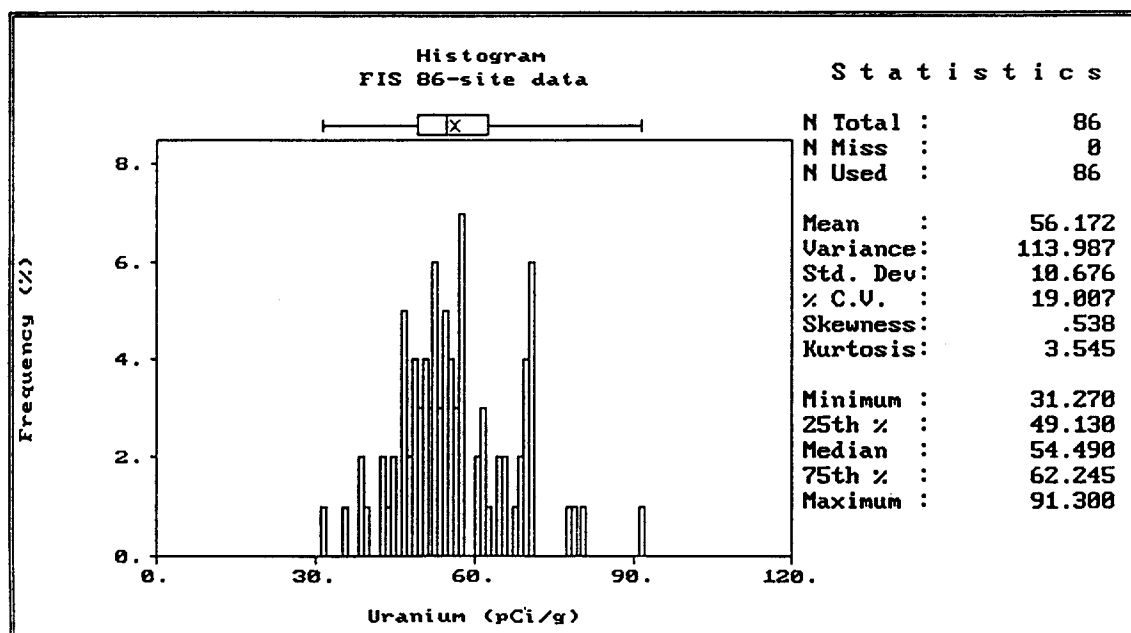
Figure 3.3 Histogram for the distribution of the 86-site data collected at Fernald Incinerator Site. The histogram class width is 1. Note the low values that the coefficient of variation and skewedness show suggesting a close-to-symmetric Gaussian distribution.

Figure 3.7 (page 24) is a normal probability plot of the 86 data. On the normal probability plot of the figure, the x-axis is scaled in such a way that the cumulative frequencies will plot as a straight line if the distribution is Gaussian. The points obviously do not conform to a straight line; however, about 70% of them lie in a straight line. Any straight line intended to fit to these points will reveal significant departures between a theoretical normal model and the actual data distribution,

especially when estimating extreme values. Nonetheless, whether a distribution is normal or something else has no particular geostatistical significance, except that it is usually more difficult to interpret variograms for highly skewed distributions [3.3].

Figure 3.4 shows a histogram from the 85-site laboratory-obtained data. Assuming that these data are more accurate than those collected by the detector prototype, and that the global mean obtained from the laboratory data is 62.091 pCi/g, the detector-obtained global mean then is 9.7% smaller than that of the laboratory. However, the trend of the distributions representing both sets of data are quite similar with their minima and maxima being close, and their distribution shapes very analogous.
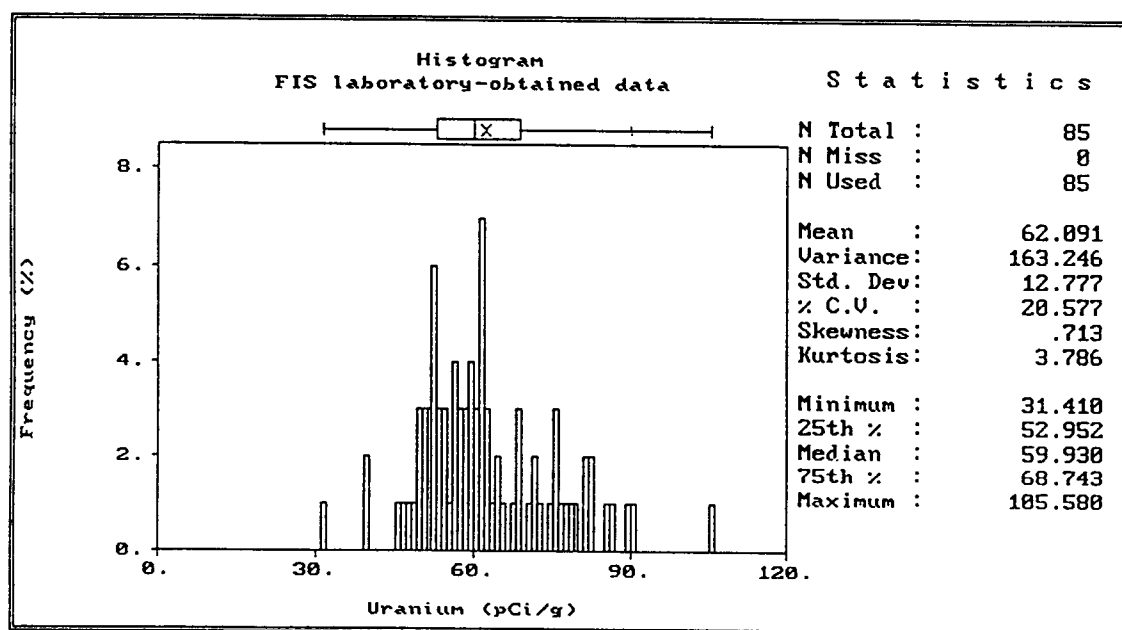
Figure 3.4 Histogram for the distribution of the 85-site hand data collected at Fernald Incinerator Site. The histogram class width is 1. The distribution is slightly skewed to the right.

3.3 Data declustering

To reduce the likelihood of bias data, a technique for declustering was applied. The technique is given by Journel [3.2] and it is known as the cell method. It shortly consists of superimposing a regular grid of cells over a posting of the data and assigning each of the datum a weight inversely proportional to the number of data within its cell. The cell size applied to the site was 30 feet by 30 feet. The weights are then applied to the estimation of the histogram which effectively declusters the data and enables an unbiased estimate.

The declustered histogram of the 86-site data is given in figure 3.5. Note the slightly positive skewedness, mean scarcely larger than the median, 57.030 and 55.600 pCi/g, respectively. The tail of the distribution slightly draws out to the right. The histogram of the declustered hand data is shown in figure 3.6.

Figures 3.8 and 3.10 are normal probability plots of the 85 and 62 site laboratory-obtained data. Figure 3.9 is the corresponding normal probability plot of the 63-declustered site data. The points obviously do not conform to a straight line; however, the likeness with a straight line is noticeable. Any straight line intended to fit to these points will reveal departures between a theoretical normal model and the actual data distribution, especially when estimating the four extreme values.

The fact that these two distributions are well-behaved is of a vital significance for the geostatistical estimations. No severe problems will be expected because the phenomenon under analysis is not represented by data with a long-tailed distribution. Under these conditions, the experimental variogram can be more easily obtained and will depict the main features of the spread of radioactive contamination in the environment.

Figures 3.3 through 3.10 were obtained with the help of the code STAT1 which is a subset of GEO-EAS 1.2.1 (see section 4.9). STAT1 is an interactive program which computes basic univariates statistics such as histograms or probability plots.
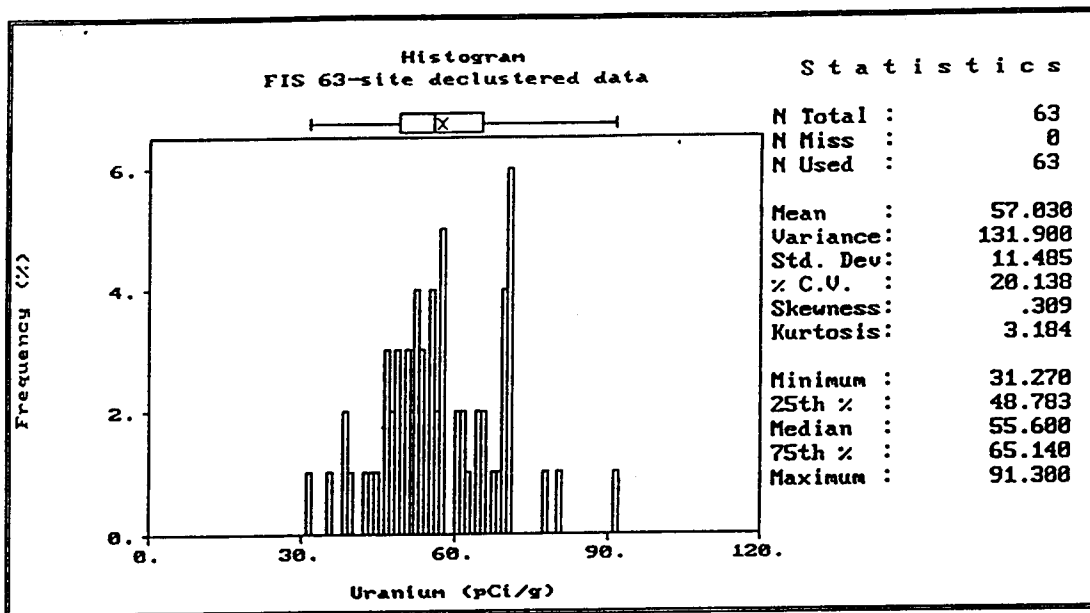
Figure 3.5 Histogram for the distribution of the 63-site declustered data. The histogram class width is 1. Note the low values that the coefficient of variation and skewness show suggesting a close-to-symmetric Gaussian distribution.
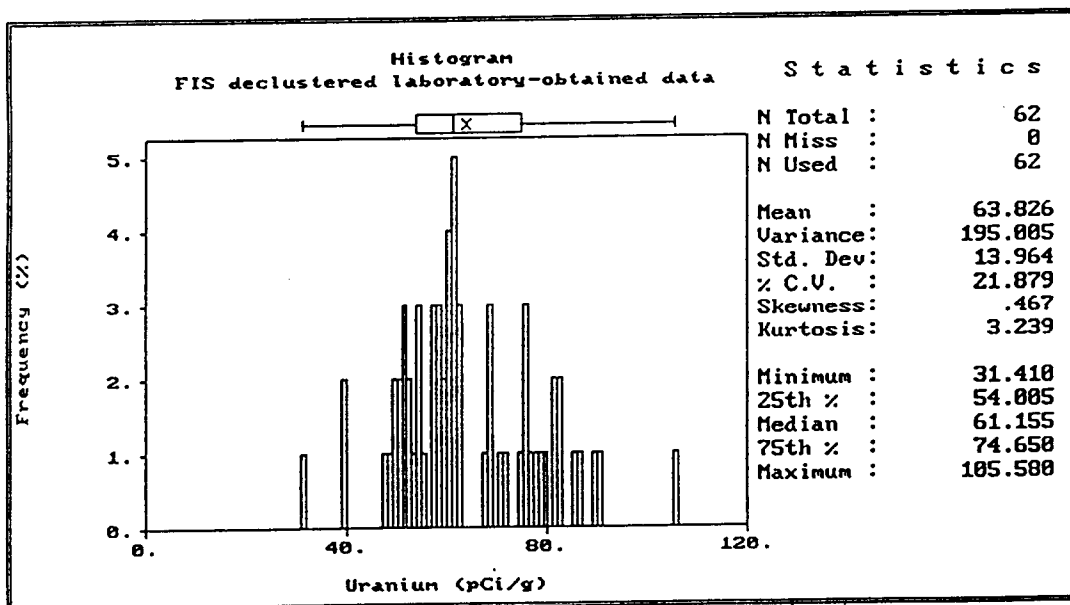
Figure 3.6 Histogram for the 62-site declustered hand data collected at Fernald Incinerator Site. The histogram class with is 1.
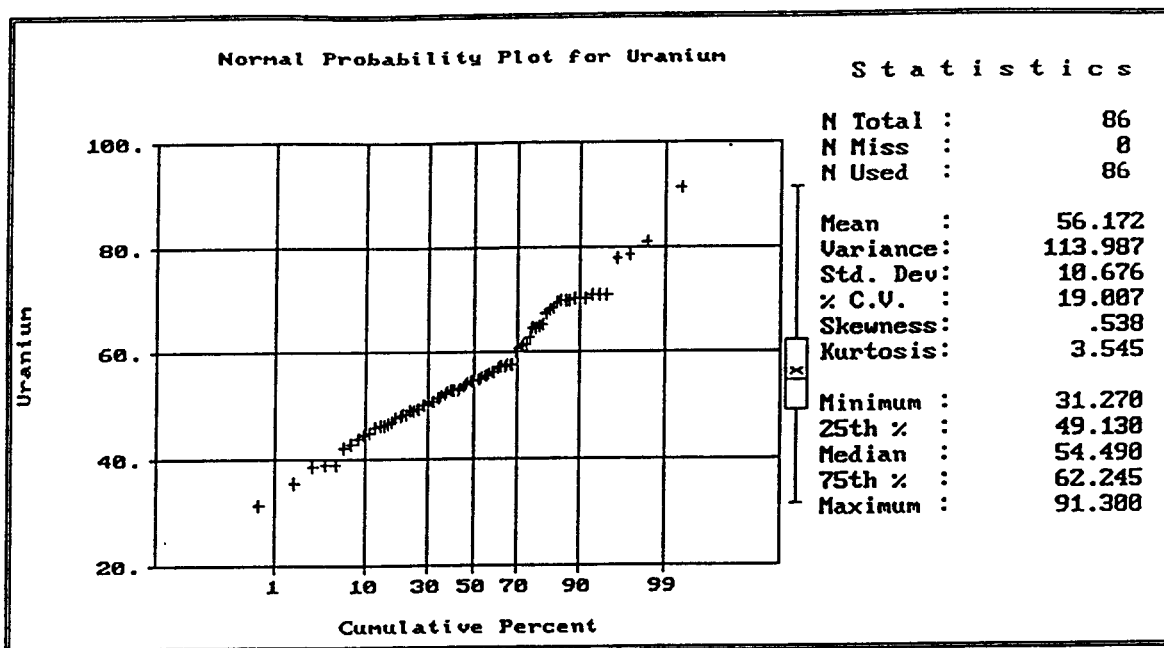
Figure 3.7 Normal probability distribution plot of the 86-site data collected at Fernald Incinerator Site. The figure shows the cumulative frequency plot scaled so that a normal distribution plots as a straight line. Note the four outliers, three in the lower limit and one in the upper limit.
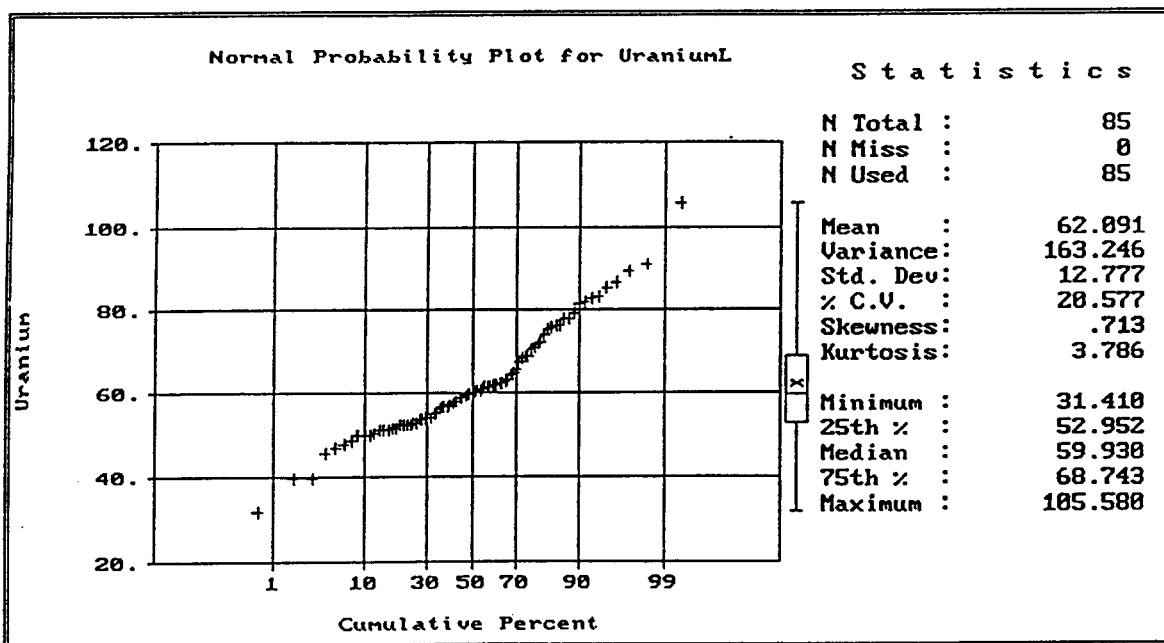
Figure 3.8 Normal probability distribution plot of the 85-site hand data collected at Fernald Incinerator Site.
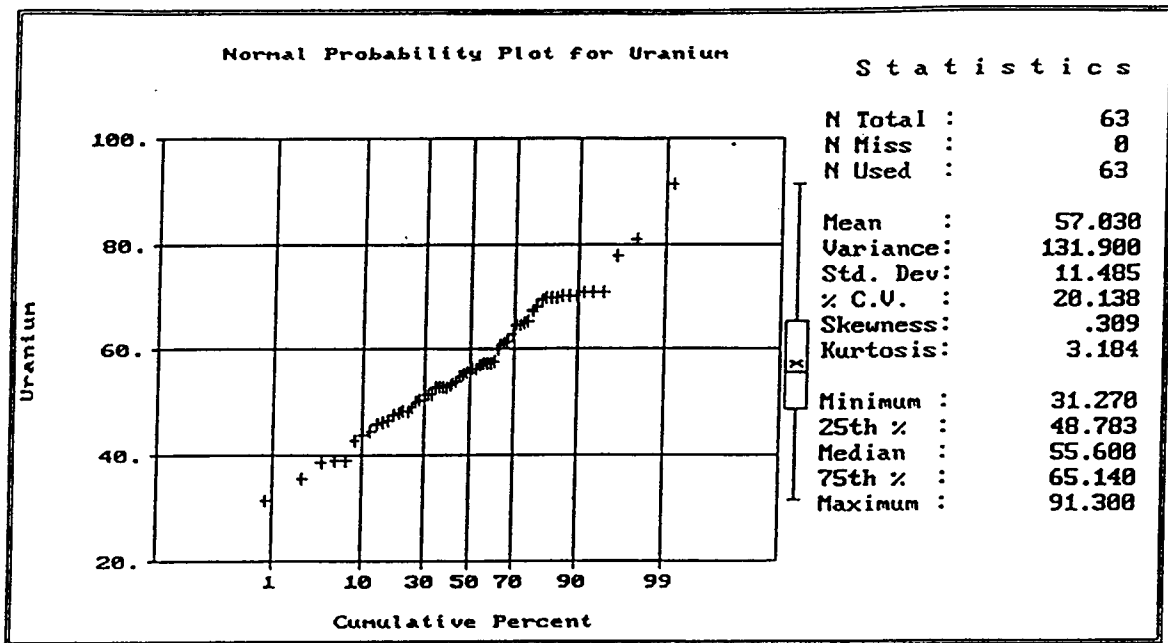
Figure 3.9 Normal probability distribution plot of the 63-site data collected at Fernald Incinerator Site.
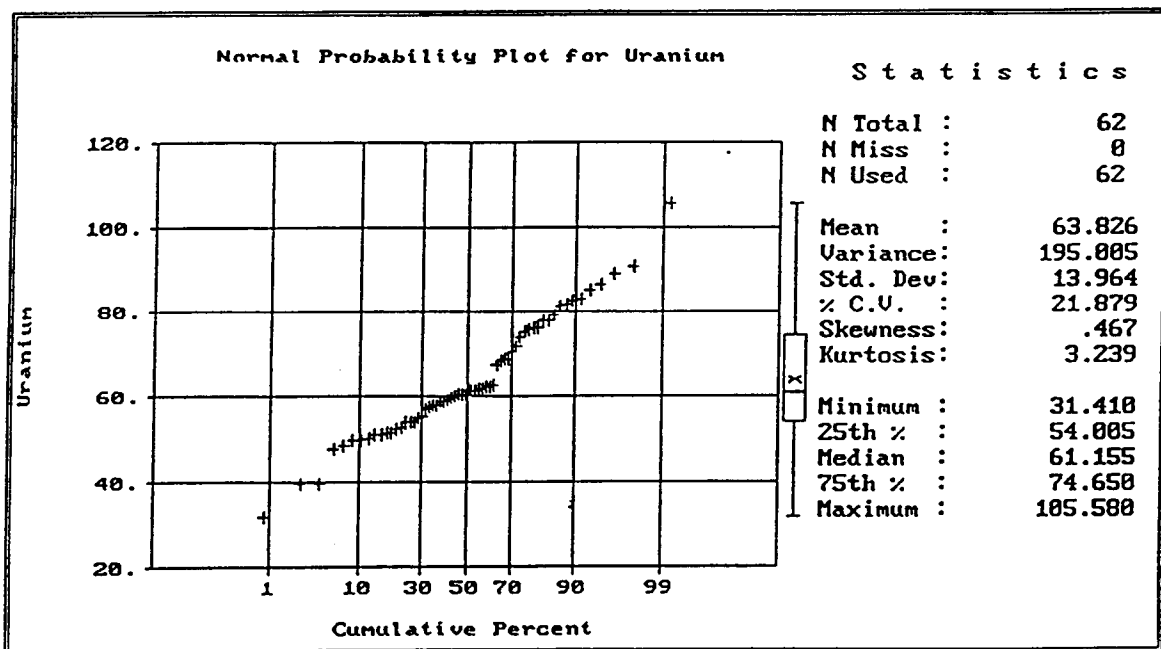
Figure 3.10 Normal probability distribution plot of the 62-site hand data collected at Fernald Incinerator Site.

3.4 References

3.1.   Journel A. G. and Huijbregts, C. J., 1978. "Mining Geostatistics." P. 29. Academic Press. New York, N. Y.

3.2.   Journel A.G., 1983. "No Parametric Estimation of Spatial Distributions." Mathematical Geology Vol. 15, No. 3, 445-468.

3.3.   Englud E, April 1991. "Geostatistical Environmental Assessment Software User's Guide." Section 4, 4-5.

4. GEOSTATISTICAL ANALYSIS

4.1 Introduction

It is not possible to determine and to know the true value of any point within the site that has not been sampled. Exhaustive sampling of vast areas to obtain more data is time consuming and impractical. To understand how the geographical distribution of a contaminant lies, a method to assess estimated values has to be implemented. Furthermore, the results of the geoestatistical analysis are affected by the characteristics of the measuring device.

In this presentation, traditional estimates of contamination levels are replaced with estimates based on kriging. The probabilistic solution to this problem thus consists of conceptualizing the unknown values as the outcomes of a random process and solving the problem for the conceptual model. A case study, Fernald Incinerator Site, is provided to illustrate the information which can be drawn from kriging. The identification of the contaminated area is provided by contour maps of equal specific activity distribution or isopleths. Cross validation is used to check the accuracy of the estimates.

The specific steps in a geostatistical study are as follows: 1) the data are initially screened and summarized through the use of simple statistical and plotting methods, 2) determination of the experimental variogram, 3) election of the variogram model to be used, 4) using kriging algorithms to map the contamination distribution on the site in isopleth contours and 5) cross validation. Item number one has already been discussed in depth in chapter 3, leaving the four remaining items for this chapter's discussion.

4.2 Geoestatistical background

There are a number of complications affecting statistical aspects of the contamination soil assessment and further cleanup. For instance, design of the sampling requires an understanding of the nature of the physical distribution of the contamination, and also is constrained by inherent difficulties in sampling for uranium. Data analysis must include the capability of obtaining estimates of average concentrations for the site, and error variances for those estimates.

The physical distribution of contamination in the site is a function of many variables. These include the way of depositing contamination, the direction and distances of events, wind velocity and its direction, and the grass on the soil surface. Obviously, whatever causes were acting to produce a certain contamination level at one point were also acting at nearby points to produce similar contamination levels. Therefore, independence of the uranium concentrations at points near each other cannot be assumed. The physical distribution is spatial in character because of the spatial nature of many of the causes such as wind and terrain. The statistical model used in designing and analyzing had to account for these characteristics as well as provide a practical representation of what is near or far.

For any point at which it is attempted to estimate the unknown value, the model to be used is a stationary random function that consists of several random variables, one for the value at each of the 86-site sample locations, and one for the unknown value at the point that is being estimated. Ordinary kriging assumes that each of these random variables has the same probability law (same expectation E), and that the covariance between pairs of random variables separated by a distance, h, is only a function of the distance. If the random variables are $V(x_i)$ with i being the sample number, the two assumptions stated above can be expressed as:

(1) $E\{V(x_i)\}$ = constant, (stationary condition)

(2) $\text{Cov}\{V(x_i), V(x_i-h)\} = K(h)$

These two equations are considered as a model for defining the uranium concentrations. However, as shown by Delfiner and Delhome [4.2], it is going to be reasonable to assume the following:

(3) $E\{V(x_i + h) - V(x_i)\} = 0$, and

(4) $Var\{ V(x_i + h) - V(x_i)\} = 2\,\gamma(h)$

$\gamma(h)$ is called the variogram function, and the associated estimation procedure is called kriging. The stationary condition $E\{V(x_i + h) - V(x_i)\} = 0$ is acceptable even if $E\{V(x_i)\}$ is not constant but it varies very little within a local neighborhood of x. With assumption (3), the presence of very light drifts do not need to be addressed. It is said that a drift exists when the expectation of a random variable varies along the site. It is assumed in this work that there is not noticeable drift effect. Should the final results suggest the presence of a drift, corresponding modifications would be included in the analysis.

4.3 Kriging

Kriging is a geostatistical technique, first developed for estimating mining ore grades, that is structured on regionalized random variables. The word kriging designates the procedures of selecting the estimator with a minimum estimation variance within a given class of possible estimators. Kriging produces estimators that are shaped mathematically by linear regression approaches of random variables. Its aim is twofold: estimation of the unsampled areas based on the sampled ones, and determination of the errors and accuracy of the model that has been applied.

The first part will be accomplished by implementing a model based on random functions and probability distributions. This is possible because a random variable can be associated with each point (sampled or unsampled) of the reference site. The model will need: a) the existence of at least second-order moments (variance or variogram and covariance) of the random variable being estimated, and its mean;

b) the assumption that two random variables are dependent only on their distances and not on their locations (equations (2) and (4)); c) the assumption of stationarity which implies that the mean and the variance of the random variables are constant.

The second part will be accomplished by determining the difference between the modeled true value and the estimator that has been used. The true value is impossible to know unless it is measured. Consequently, it must be modeled, and it will be referred to as the true value, but it should be recalled that the modeled true value is an idealization of the "real" one.

Kriging is mathematically described by a set of n linear equations with n unknowns, n being the number of samples. The system of equations is referred to as the kriging matrix system. The matrices of the system are the matrix of the covariances between all pairs of sample points, **A**, and the matrix of the covariance between each sample point and the point being estimated, **Z**. The solution of the kriging defines the chosen estimator and also the errors associated with kriging.

The presence of drifts is evaluated before applying any specific kriging estimates. However, the removal of the drift effect can be considered when there is an expectation that changes constantly but its change is small enough that can be taken as constant in blocks of land within the site (equations (3) and (4)).

There are several geostatistical methods for estimating, namely simple kriging, universal kriging, ordinary kriging or probabilistic kriging. Ordinary kriging was chosen for this study for several reasons. No mean hypothesis is required to apply ordinary kriging, and indeed it develops an estimation algorithm which does not require prior estimate or knowledge of the mean. Ordinary kriging supplies with a good smoothing degree and accounts for redundancy of nearby samples. The standard deviation of the errors obtained by this kriging method is low. This method is also simple to understand and to implement.

4.4 Ordinary Kriging

To determine the value of the radioactive contamination at any unsampled location within the target soil using the collected data, a system of n+1 equations has to be solved. The n+1 unknowns are the n data samples plus one more unknown (Lagrange parameter) which is introduced to help find a solution to the system of equations.

In section 1.2.1, it was shown that at every point where there is not a sample, the unknown true value will be estimated using a weighted linear combination of the available samples:

$$\hat{z}(x_o) = \sum_{i=1}^{n} \lambda_i z(x_i)$$

The $z(x_i)$ are the sampled locations and therefore well-known values. The set of weights is allowed to change as the estimation of unknown values changes at different locations. Additionally, the weights, λ_i, sum to 1 because of the unbias constraint of ordinary kriging (OK) which requires that the error at any particular location has an expected value of 0. The weights can be calculated from the product of the matrices A and Z as follows:

$$A.w = Z$$

where w is the vector consisting of the kriging weights, λ_i, and the Lagrange parameter μ, A is the symmetric covariance matrix (n+1 x n+1) and consists of the covariance values C_{ij} between the random variables V_i and V_j at the sample location. It records the distances between each sample and every other sample through the covariance function or its corresponding variogram function. The matrix A records the distance in terms of statistical distance rather than geometrical distance; that is, the weight associated to each sampled point prevails over its geometrical distance from the estimation point. The covariance matrix , Z, which is a 1-column matrix, consists of

the covariance values C_{io} between each random variable and the random variable V_o of the point being estimated.

Once the estimate is calculated, the OK error variance, σ^2_{OK} , is expressed as:

$$\sigma^2_{OK} = \sigma^2 - w.Z$$

with σ^2 being the corresponding value of the covariance function for a distance h equal to 0. This equation is been obtained after the application of other constraint by which the error variance is minimized.

In order to build the matrices **A** and **Z**, an understanding of the covariance or the variogram functions is needed. In geostatistics, covariance is usually treated as the simple inverse of the variogram, and computed as the overall sample variance σ^2 minus the variogram value. The choice of a variogram model is a prerequisite for ordinary kriging, consequently a model has to be fit to the sample variogram. There are two reasons why the sample variogram cannot be used directly in the ordinary kriging system: first, the matrix **Z** may call for variogram values for distances that are not available from the sample data; second, the use of the sample variogram does not guarantee the existence and uniqueness of the solution to the ordinary kriging system.

4.5 Variogram analysis

The variogram provides information on the form of a relationship between two observations as a function of the intervening distance, under the assumption that a measurement at any point represents nearby locations better than locations farther away. Variogram analysis attempts to quantify this relationship and also to show how the spatial continuity, that is assumed, changes with direction. Since the experimental variogram is not enough to solve the problem of soil characterization, as shown in section 4.4, a variogram model is then required.

The computation, interpretation and modeling of variograms is the essence of a geostatistical study. The variogram model is an interpretation of the spatial correlation

structure of the sample data set. The variogram controls the kriging weight assignments during interpolation, and consequently controls the quality of the results. The variogram then is not unique but a considerable number of them could be brought to consideration.

The shape of the variogram is also affected by the characteristics of the detector prototype. A measurement actually represents an average over the quantity of material measured (the support). Measurements on smaller support are averages over smaller quantities, which are more variable than averages over larger quantities. Hence, as supports get larger, increments become less variable, resulting in a smoother variogram.

The effects of the selected nugget, sill, range and directional dependence play a crucial role when choosing the variogram function, and determine the type of variogram. A variogram is said to have a nugget effect when there is a discontinuity at the origin of this variogram. In practice, the nugget effect can result from a combination of other factors besides the discontinuity in the physical phenomenon. Sampling errors might cause sample values separated by very small distances to be quite dissimilar. The range is the distance at which the variogram reaches its maximum value or asymptotically approaches it. The sill is defined as the plateau that the variogram reaches at the range.

After the model variogram has been shaped, the variance between all pairs of sample locations is well defined. Because of the good behavior of the distribution of the collected data, see figures 3.7 and 3.9, the experimental variogram can easily be obtained from the available data and they will portray the main features of the phenomenon under study. The kriging equations can then be solved, and OK provides improved, risk-qualified, local estimates.

4.6 Variogram model

To begin computing the variogram model, it is required to specify the distance class intervals or lags and directional tolerances. Finding the best combination is a trial and error exercise. The systematic approach that is to be used in this work is next summarized. After the appropriate lag between groups is fixed, an omnidirectional variogram is sought. All possible pairs will be included in the omnodirectional variogram. As shown by Barnes [4.3], the variogram is often isotropic. This maximizes the number of pairs in each lag which usually gives the smoother variogram. From this omnidirectional variogram, the best estimate of the y-intercept (nugget) and maximum value (sill) parameters for the variogram model can be drawn, as well as the best idea of what type of model should be fit. In general, the most common models that are used in radioactive contamination studies are the linear, spherical, exponential and Gaussian. A good fit to the experimental variogram is then such that will cast confidence in the model.

Figures 4.1 through 4.3 display the omnidirectional experimental variogram for three lag intervals of 10, 25 and 35 feet respectively. As these lags become closer, more detail information is obtained about samples that are closer. Because of the distance dependence between two given pairs, the influence of neighboring pairs will be larger than that of pairs located far apart. As the distance interval increases, the variogram becomes smoother and the amount of carried information smaller. The variogram model with a lag interval of 10 feet provides sufficient information as to fit the experimental variogram.
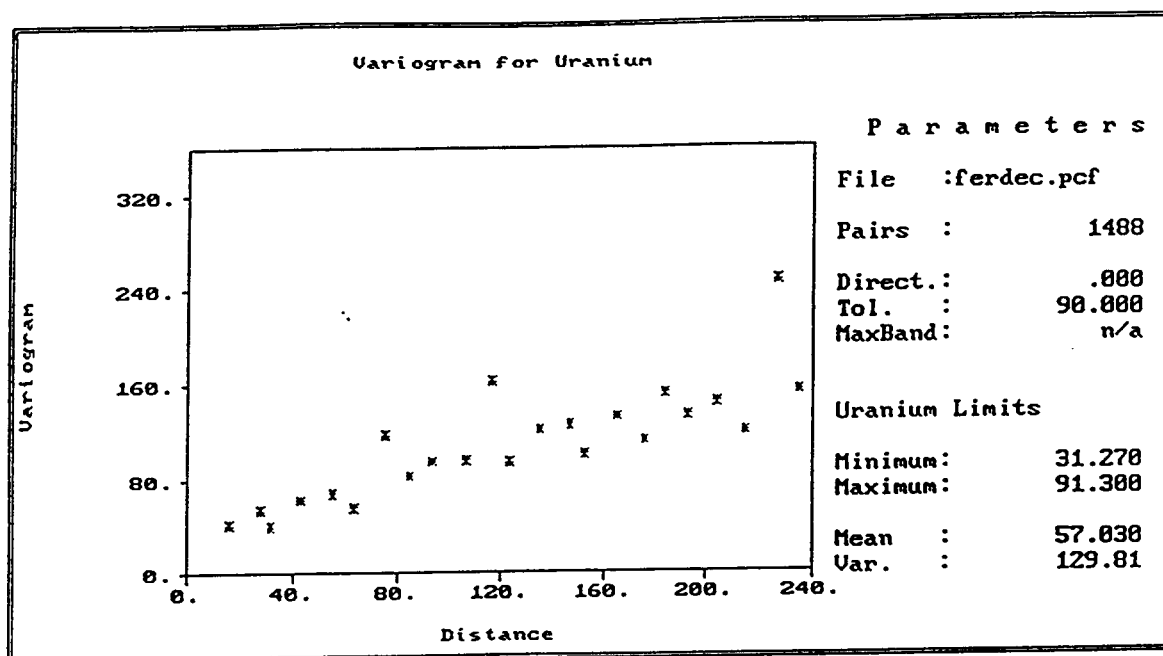
Figure 4.1 Experimental variogram for a lag interval of 10 feet.
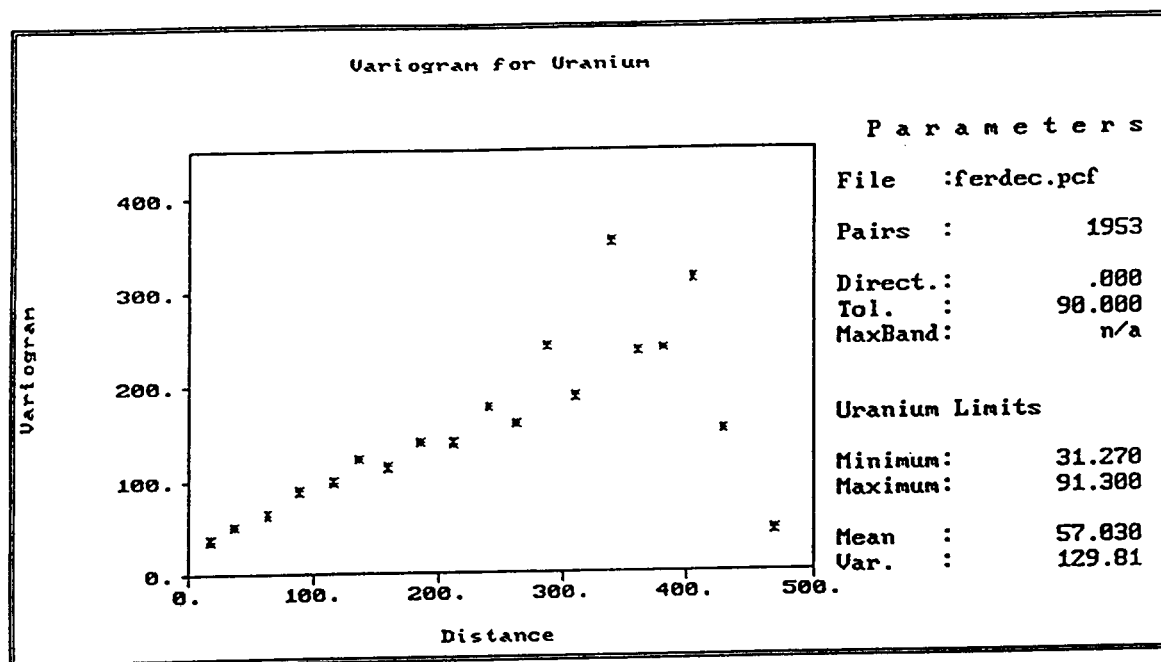
Figure 4.2 Experimental variogram for a lag interval of 25 feet.
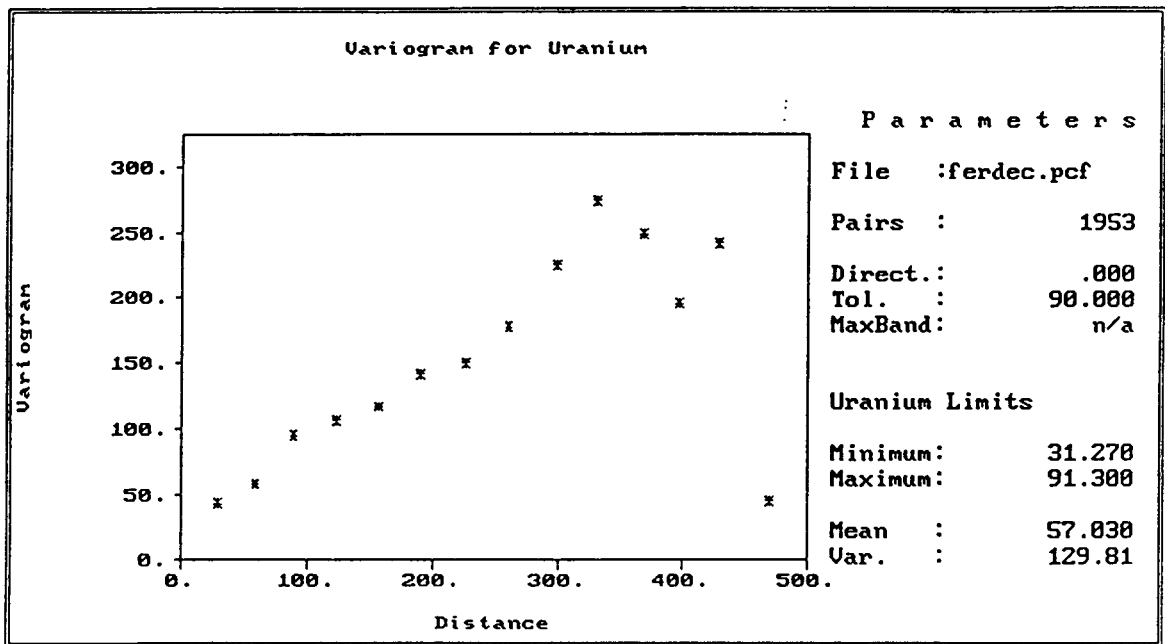
Figure 4.3 Experimental variogram for a lag interval of 35 feet.

Figures 4.4 through 4.8 show the variogram models that were fit to the omnidirectional experimental variogram. Figure 4.4 shows the best linear model with nugget effect of 35 that was achieved. No better fit was found for a null-nugget-effect linear model. The linear variogram suggests a linear dependence between the distance of pairs in the same lag and their variogram function values. It is not defined what the range of influence would be in this instance because the variogram is monotonically increasing with distance. However, a certain range must be fixed if this model is to be applied.
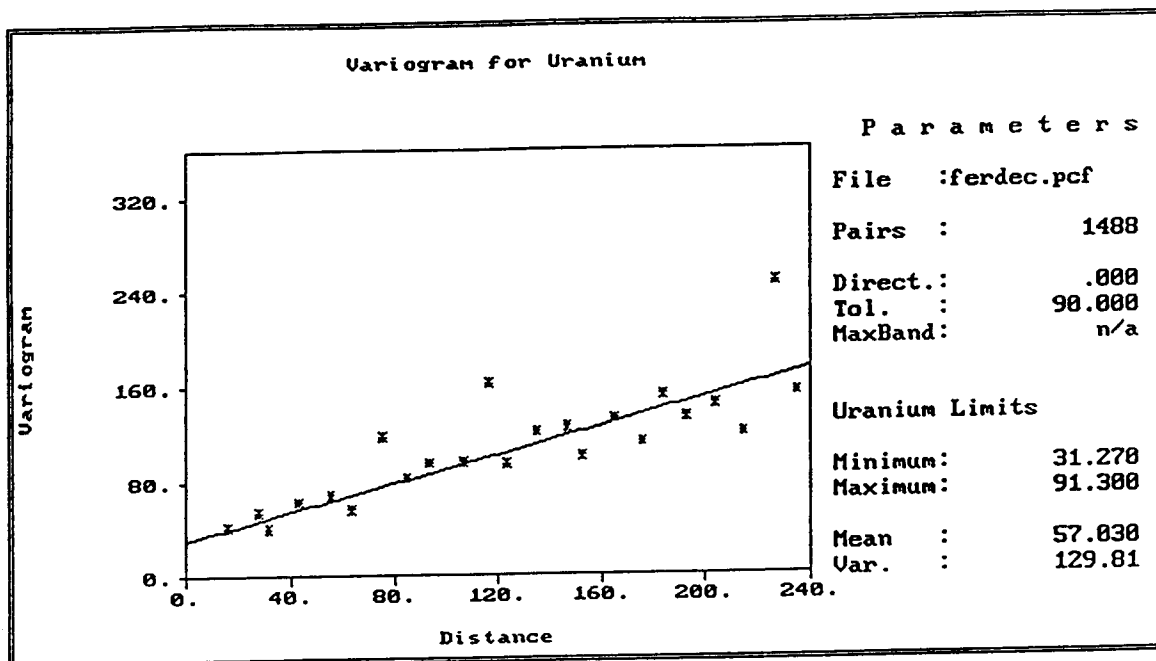
Figure 4.4 Linear variogram model. Nugget effect = 35.
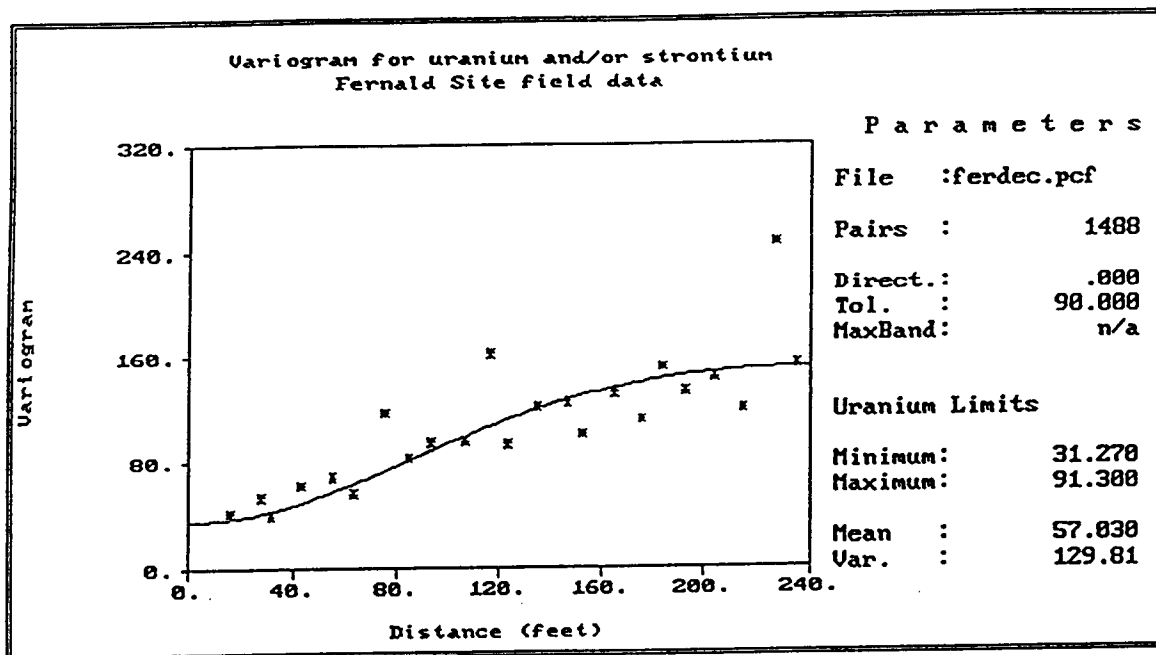
Figure 4.5 Gaussian variogram model. Range = 240, sill = 145.

Figure 4.5 shows a Gaussian fit to the experimental variogram. The best fit that was obtained displays a nugget effect of 35 and fits reasonably well to the experimental variogram. The 240-foot range of the variogram model is defined as well as the sill (145). Beyond 240 feet, it is considered that the variogram model is not valid.

Figure 4.6 shows an exponential fit with no nugget effect. The range and sill that were found are 240 and 145 respectively. The absence of the nugget effect suggests a smooth phenomenon. Figures 4.7 and 4.8 show the best spherical models with and without nugget effects that were found. Although both have the same variogram range of 240, they differ in their nugget effects and sill values. The fact that a null-nugget-effect variogram model was found as the best fit in either instance gives confidence in the model results.
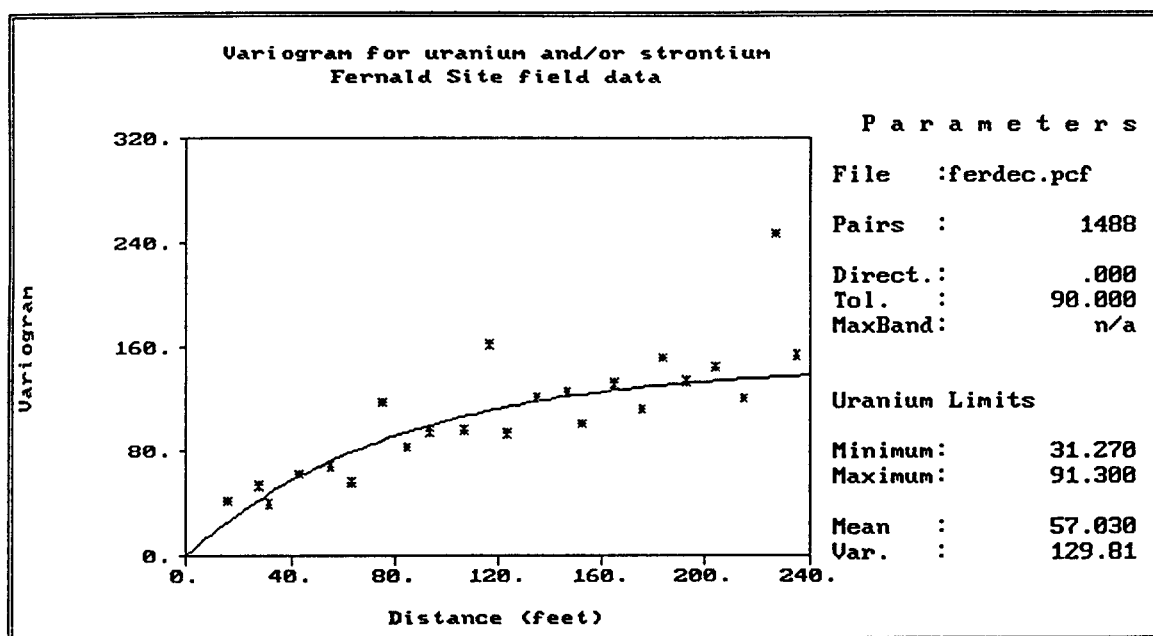
Figure 4.6 Exponential variogram model. Range = 240, sill = 145.
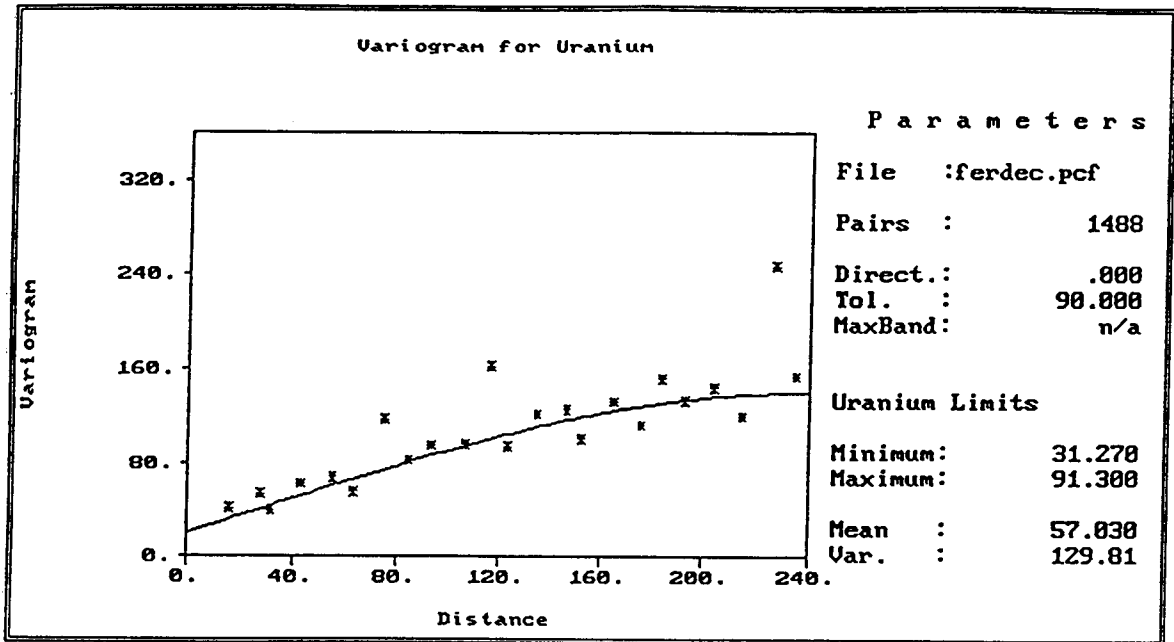
Figure 4.7 Spherical variogram model. Nugget effect = 20, range = 240, sill = 120.
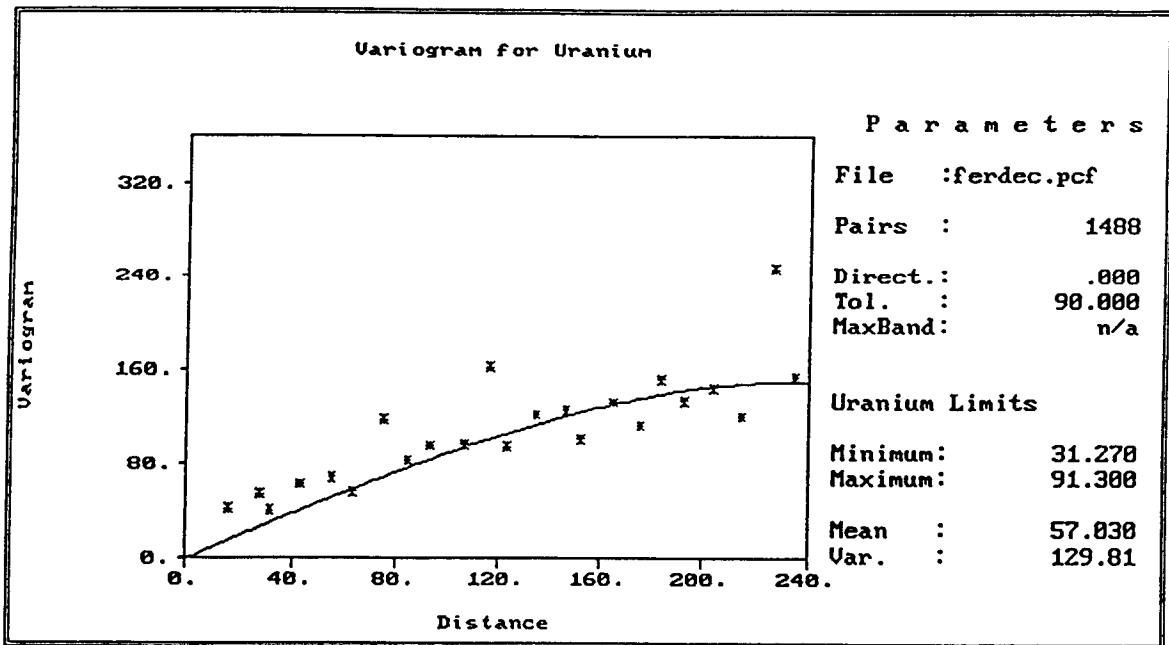
Figure 4.8 Spherical variogram model. Range = 240, sill = 150.

The directional analysis showed certain spatial continuity (anisotropy) in the 90° direction up to a range of 120 feet (figure 4.11), which is reasonable since predominant winds are in the southwesterly direction. Figure 4.9 is an illustration of the direction parameters. Figure 4.10 shows the model variogram on the 45° direction and a tolerance of ± 15° with 249 pairs that contribute to the variogram model. The omnidirectional variogram of figure 4.6 is smoother than that of figure 4.10 and represents a better approach to the experimental variogram. No spatial continuity in this direction can therefore be reported. Figure 4.12 is the 135° direction variogram. It does not show a clear pattern of continuity in this direction. A closer inspection of the hand data does not confirm the existence of anisotropies in this direction. No drifts were found in any particular direction.
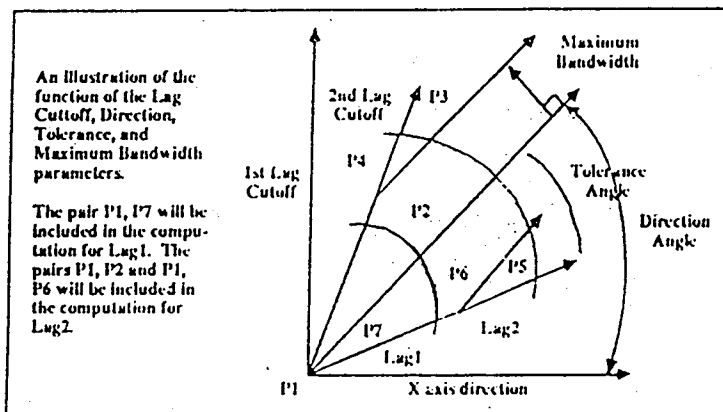
Figure 4.9 Illustration of the direction parameters [4.4].
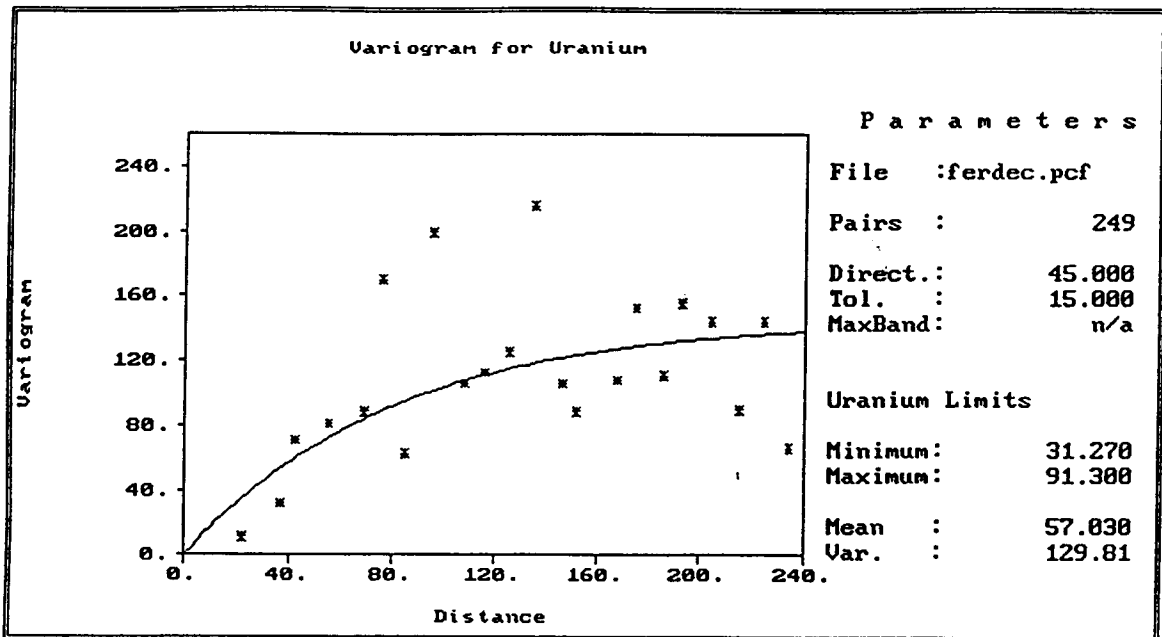
Figure 4.10 45° variogram model. No spatial continuity is observed.
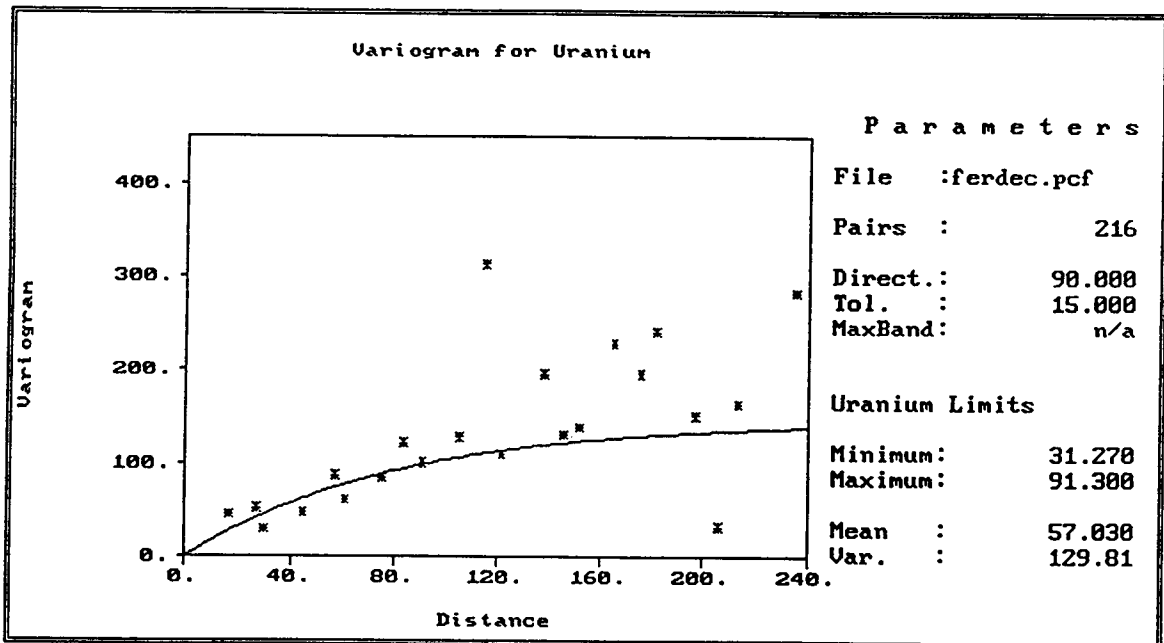
Figure 4.11 90° variogram model. Spatial continuity is observed up to 120 feet.
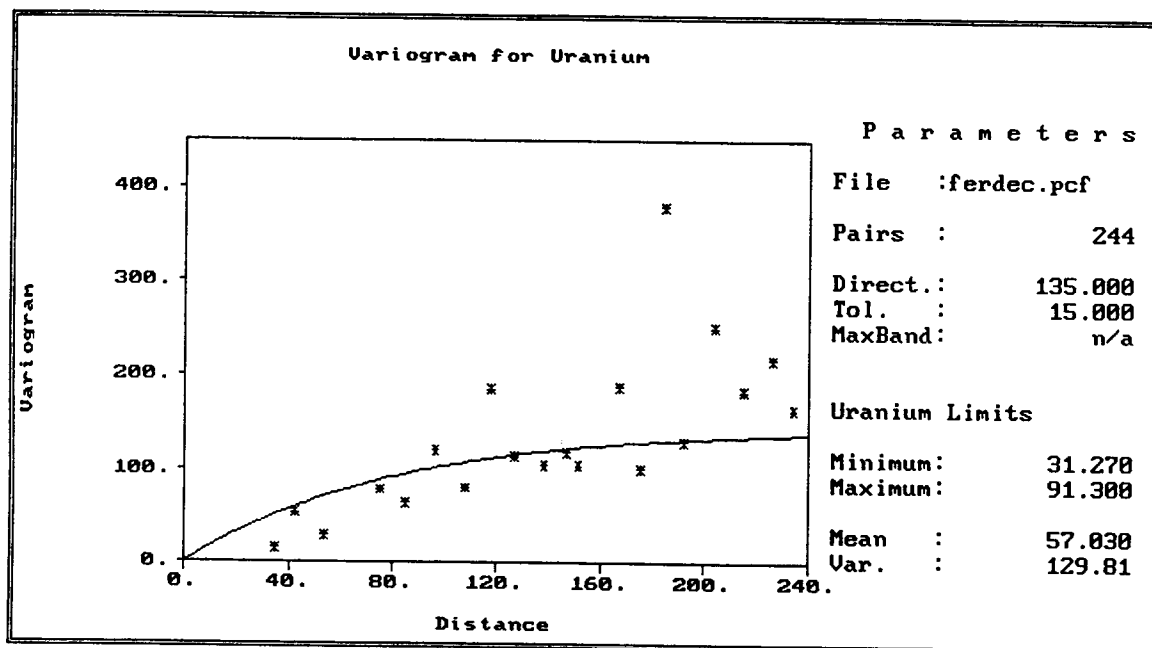
Figure 4.12 135° variogram model. No anisotropy is present.

4.7 Cross validation

Cross validation is a technique to compare estimated and true values using only the information available from the collected data. Because cross validation serves the purpose of improving the estimation procedure, it becomes a useful preliminary step before final estimates are calculated. The estimates are compared to the original observations in order to test whether the hypothetical variogram model and neighborhood search parameters will accurately reproduce the spatial variability of the sampled observations.

All of the variogram models with nugget effects were ignored because of the fair assumptions that the phenomenon under study is continuous, and non-sampling errors were involved in the sampling campaign. Only the two models that had null nugget effect were considered, see figures 4.6 and 4.8. A cross validation of the exponential and spherical models yielded that the exponential model was preferable.

Figures 4.13 through 4.18 show the results of the cross validation analysis. Figures 4.13 through 4.15 are related to the spherical variogram model, while figures 4.16 through 4.18 to the exponential model. Very small error differences were observed between them; however, results favored the exponential model. Figures 4.13 and 4.16 show the kriged estimates errors scatter plots for both the spherical and exponential models, respectively. The symbol "+" refers to an overestimation (estimate - observed > 0), and the "x" mark for negative differences or underestimation. About 80 % of the kriged estimates are in the [-10 %, 10 %] error interval in both cases, and 52 % (spherical model) and 54 % (exponential model) of the estimates are in the [-5 %, 5 %] interval.

Figures 4.14 and 4.17 give a qualitative idea of the error size for both selected models. The same symbol reference used in figures 4.13 and 4.16 applies here. Figures 4.15 and 4.18 show a histogram of the error distributions for both selected models. The fact that the majority of the errors are in the [-10 %, 10 %] interval gives confidence in the obtained results.
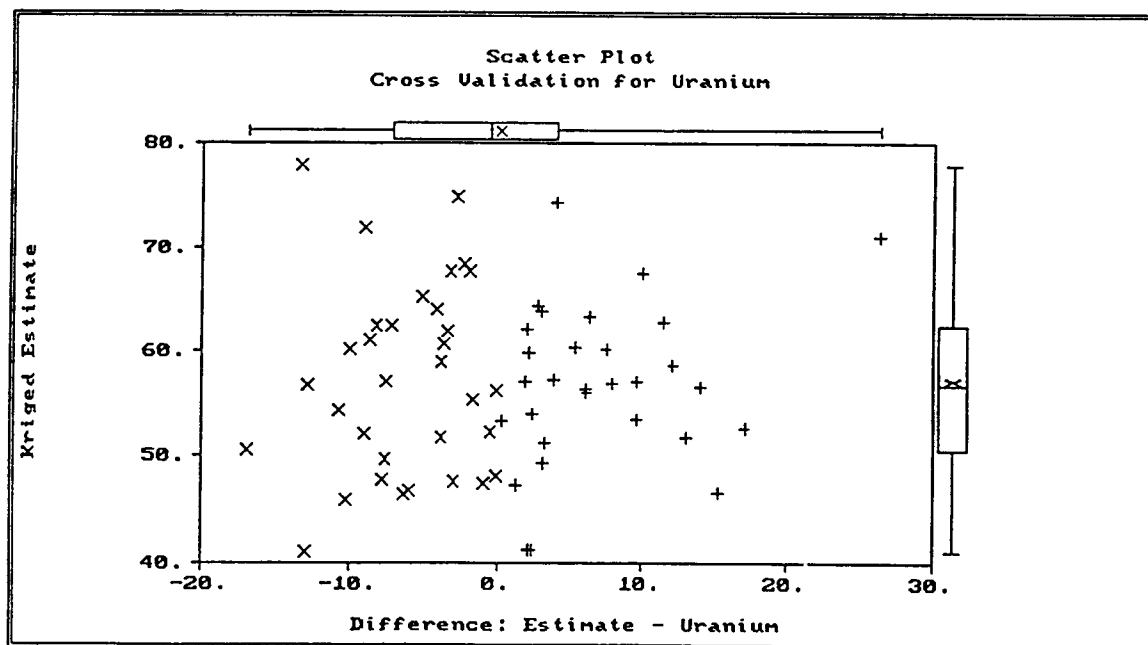
Figure 4.13 Cross validation scatter plot. Spherical variogram model.
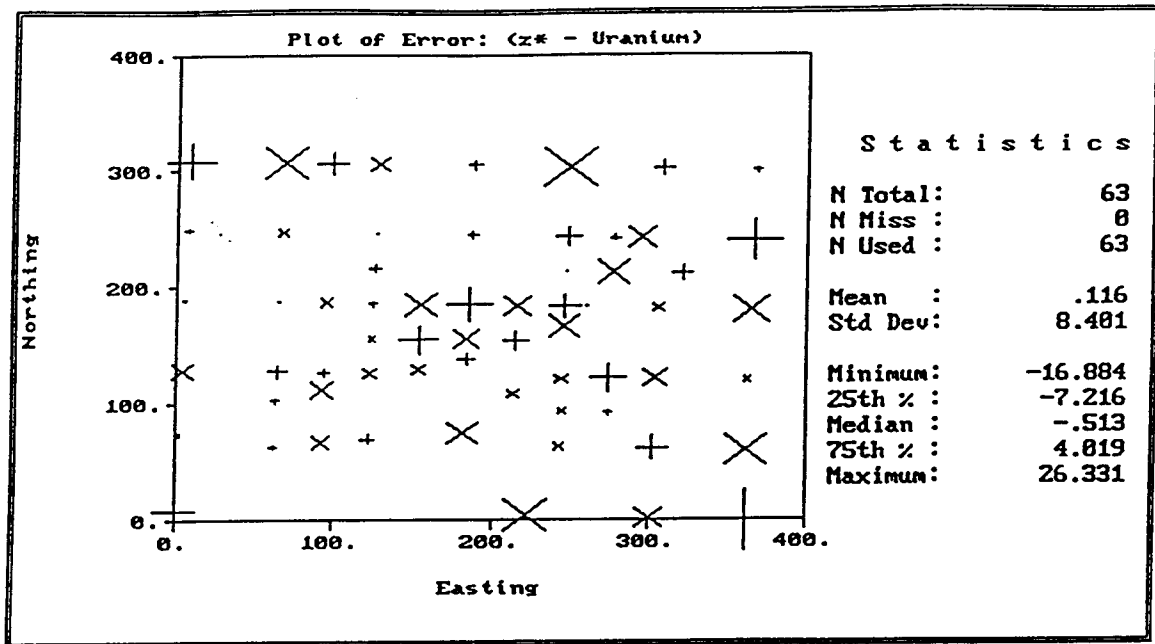
Figure 4.14 Plot of the error distribution. Spherical variogram model.
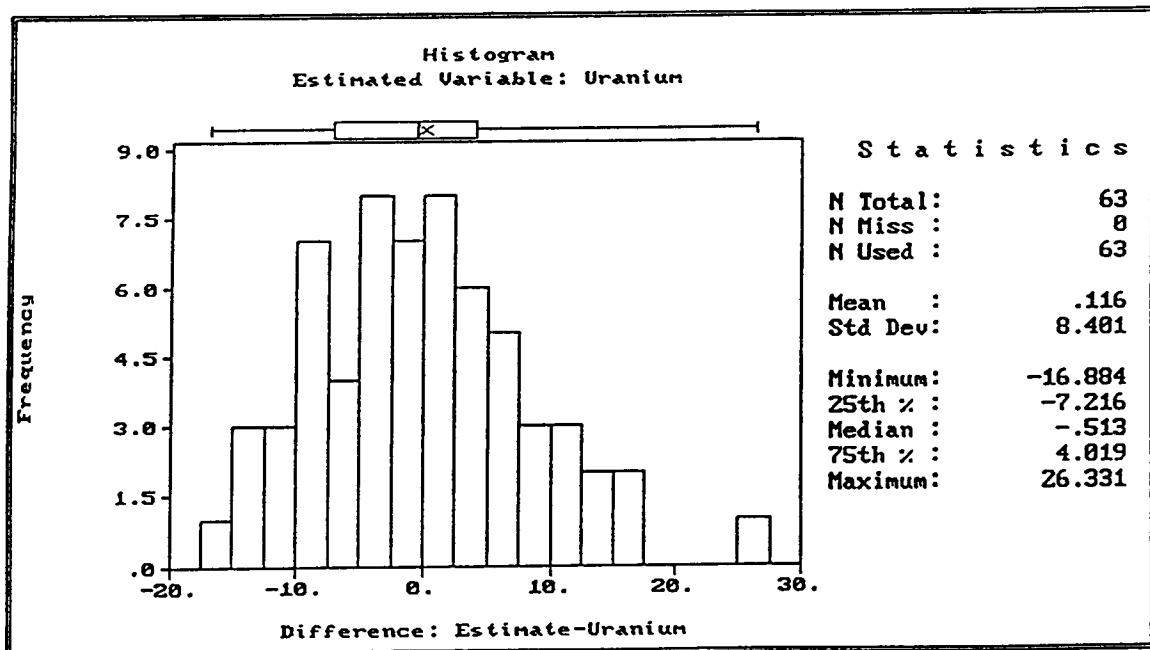
Figure 4. 15 Histogram of the error distribution function. Spherical variogram model.
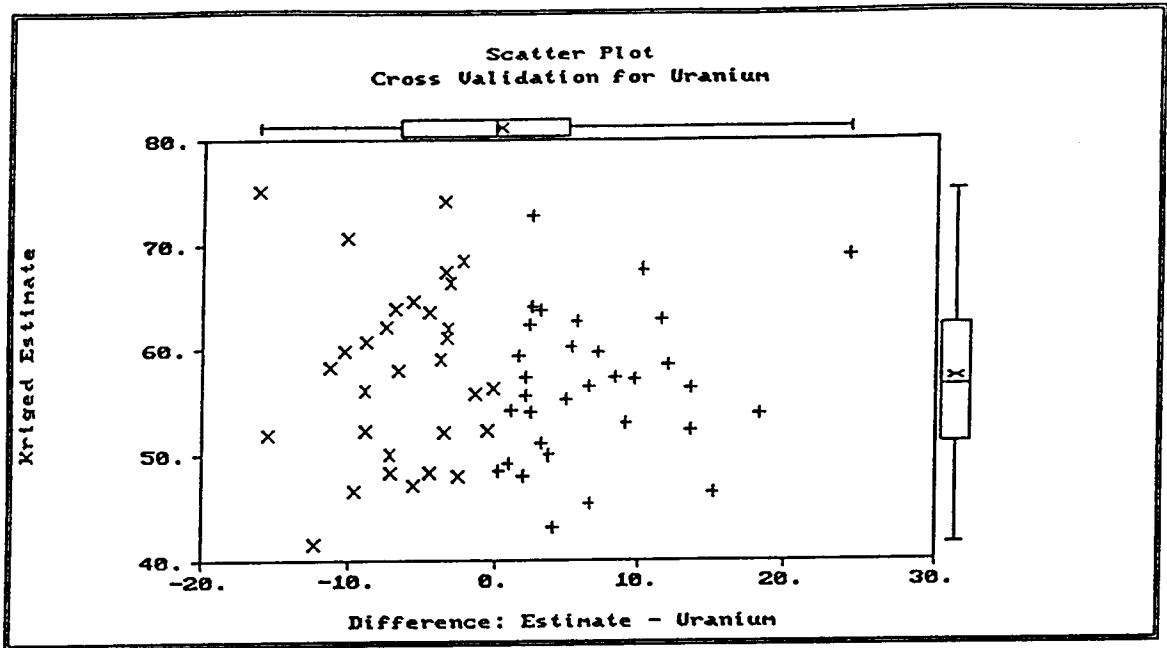
Figure 4.16 Cross validation scatter plot. Exponential variogram model.
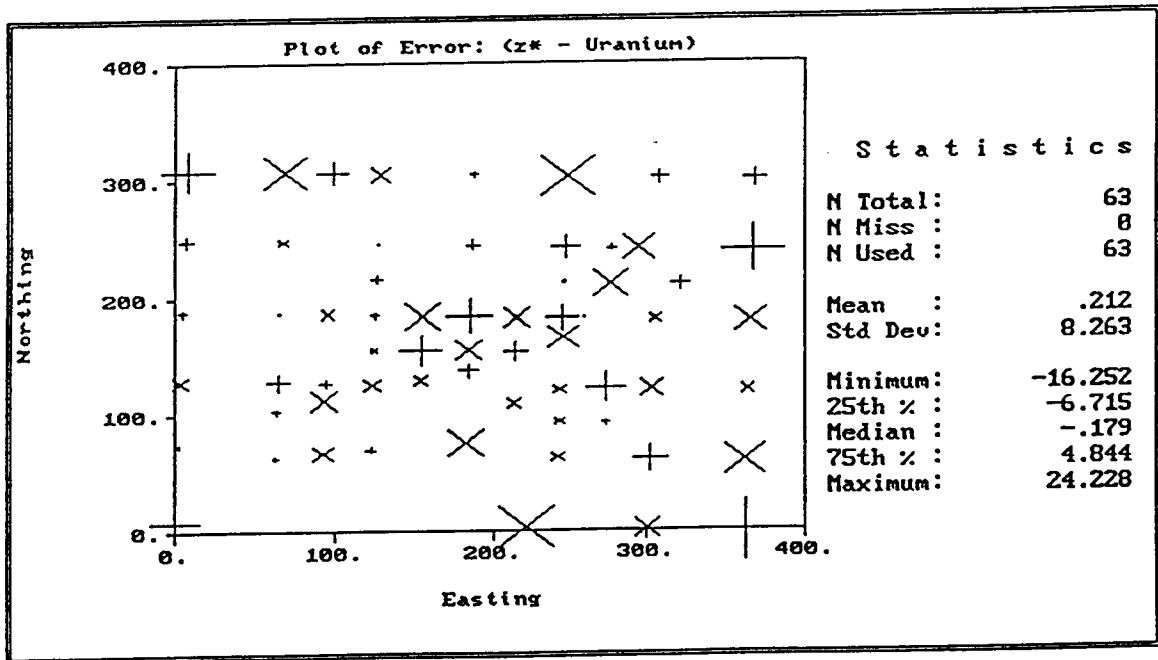
Figure 4.17 Plot of the error distribution. Exponential variogram model.
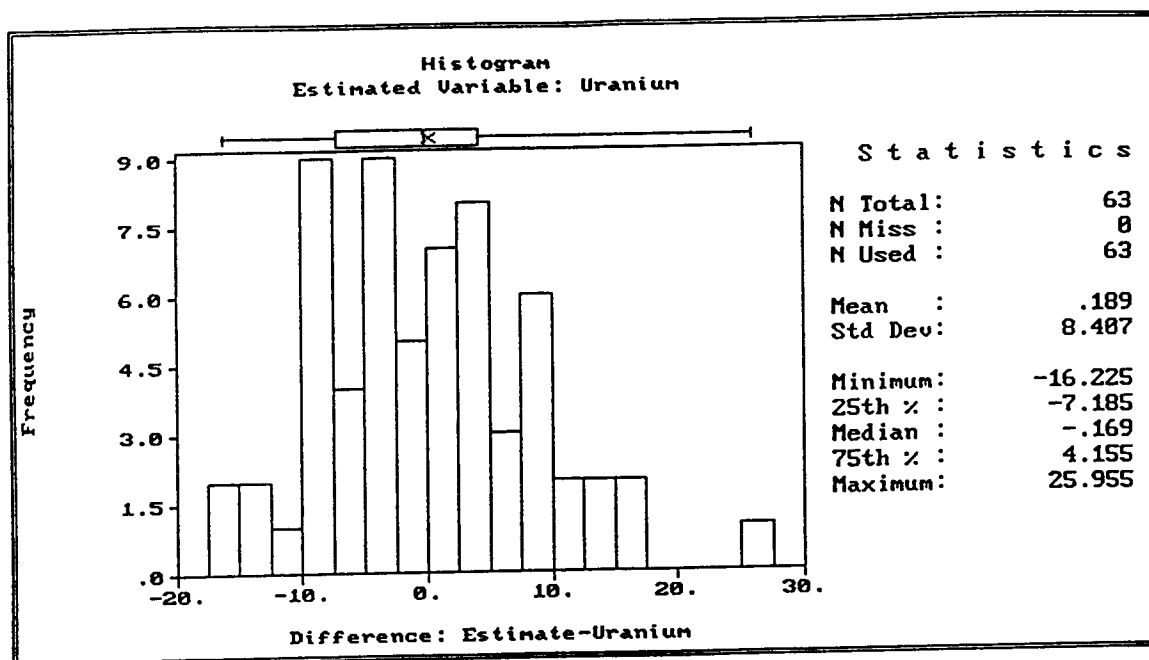
Figure 4.18 Histogram of the error distribution function. Exponential variogram model.

Based on the above results, the exponential variogram model has been chosen to fit the experimental variogram considering its slight error advantage over the spherical model. However, the spherical option could have been taken into consideration as well since it offers also an accurate approach to the experimental variogram.

4.8 Kriging and contouring

The solution of the ordinary kriging equations (see page 31) is performed with the program Krige from the software package GEO-EAS 1.2.1. For each point kriged, the program calculates the matrices **A** and **Z** which makes possible the determination of the kriging weights, λ_i, and error variance (see section 4.4).

A rectangular grid of kriged estimates is created with the two-dimensional kriging program, Krige, and stored in a GEO-EAS data file. Contour maps may be generated from these kriged estimates with the program Conrec. The contour map of

the spatial distribution of the ^{238}U and ^{90}Sr contamination at Fernald Incinerator Site is shown in section 6.2. In this section will be discussed the way Krige operates.

The Krige option screen and the parameters that had been chosen for block kriging are show in figure 4.19. The type of kriging and the search parameters are the most significant options. These two options have here the control of the kriging method.

4.8.1 Block kriging

Ordinary block kriging (OBK) is more realistic than point kriging. Therefore, (OBK) is of more interest than point kriging to estimate average values within local areas. Block kriging has the advantage of producing estimates of the block average with the solution of only one kriging system, and thereby computational savings when calculating average point-to-block covariances are remarkable.

```
--------------------------------- K R I G E   O P T I O N S ---------------------------------
| Title: Kriged estimates of the 63-site data                                               |
| -----------------------------------------------------------------------------------------
| Data                          | Grid Parameters                                           |
|                               |                                                           |
| Data File   : ferdec.dat      |                      X              Y                     |
| Output File : ferdec.grd      | Variable  :  Easting       Northing                       |
| -----------------------------| Origin    :           .000            .000               |
| Polygon                       | Spacing   :         40.800          34.333                |
|                               | Number    :            10              10                 |
| Polygon File:                 | -------------------------------------------------------- |
| Sample Select: No             | Search Parameters                                         |
| -----------------------------|                                                           |
| Type                          | Major Radius :       80.000 # Sectors     :  1            |
|                               | Minor Radius :       80.000 Max in Sector:  8            |
| Type of Kriging :  Ordinary   | Ellipse Angle:         .000 Min. to use   :  1            |
| Point or Block  :  Block 4x4  |                                                           |
|                               | Distance Type: Variogram    Empty Sectors:  0            |
--------------------------------------------------------------------------------------------
```

Figure 4.19 Kriging option screen as it is displayed by Krige.

In order to use the block kriging, some modifications have to be performed in the kriging matrix system of page 31. The matrix form of the point kriging is:

$$A.w = Z$$

By simple examination of this equation (also see table 6.2), it is seen that the location of the point or block that is being estimated has absolutely nothing to do with the construction of the covariance matrix **A** which is independent of the location at which the estimate is required. So it could correctly be concluded that **A** does not require modifications for block kriging. However the values required for the covariance vector **Z** are the point-to-block covariances and they vary with the estimate. Consequently, by adjusting the covariance vector **Z** to the new situation, the point kriging can be transformed into an ordinary block kriging.

The point-to-block covariances that are required for the block kriging can be developed as follows:

If B is a block area and $V_B = B^{-1} \sum V_j$ the random variable representing the average value of the surface contamination over the area B, then

$$
\begin{aligned}
C_{iB} &= \text{Cov}\{V_B V_i\} = E\{V_B V_i\} - E\{V_B\}E\{V_i\} \\
&= E\{B^{-1} \sum V_j V_i\} - E\{B^{-1} \sum V_j\}E\{V_i\} \\
&= B^{-1} \sum E\{V_j V_i\} - B^{-1} \sum E\{V_j\}E\{V_i\} \\
&= B^{-1} \sum [E\{V_j V_i\} - E\{V_j\}E\{V_i\}] \\
&= B^{-1} \sum \text{Cov}\{V_j V_i\}
\end{aligned}
$$

The summation in the above equations is extended to any j within the block area B.

The covariance between the random variable at the i-th sample location and the random variable V_B representing the average value of the spread of contamination over the area B is the same as the average of the point-to-point covariance between V_i and the random variables at all the points within B.

The block kriging error variance is given now by:

$$\sigma^2_{OK} = C_{VV} - \left(\sum \lambda_i C_{iB} + \mu \right)$$

where C_{VV} in this equation is the average covariance between pairs of locations within the block B. The expression that let C_{VV} be computed is showed below:

$$C_{VV} = \frac{1}{B^2} \sum_{ij} C_{ij}$$

The summation of this equation is extended to all i and j within B.

The number of discretizing points that are needed within B to yield an adequate approximation of the components of the covariance vector $\mathbf{Z}$ is something related to computer memory savings and calculational accuracy. Fewer discretizing points require less computer memory and thus the computations are faster. This computational efficiency must be weighed against the desire for accuracy, which calls for as many points as possible. For a two-dimensional block, sufficient accuracy can usually be attained with a 4 x 4 grid containing 16 points [4.1].

4.8.2 Search strategy

The choice of a search strategy that controls the samples that are included in the estimation procedure is of a paramount significance when considering any approach to local estimation. Considerations such as number, relevance and redundancy of nearby samples has to be defined before further steps are taken.

Because of the capability of the program Krige that can handle any number of nearby samples, an ellipse (or circumference) centered on the point being estimated is used as the search neighborhood within which all available samples contribute to the estimation.

The size of the circle used for kriging has next to be decided. It must be large enough to include some samples. The geometry of the data set decides the size of the search circle. The larger the search window is, the larger the number of nearby samples within the circle. Nonetheless, there are two factors that control the size of

the search window: first, using more samples increases the amount of computation time; and second, as samples come from farther and farther away, the appropriateness of a stationary random function model becomes more doubtful. It has been noticed that as the search circle becomes larger, the estimation algorithm can still be applied, but with an ever-increasing departure between the theoretical statistical properties predicted by the model and their real counterparts. By restricting the samples to small neighborhoods, the stationary random function conceptualization becomes more plausible and the difference between the actual statistical properties and those of the model are less severe.

The possibility that some nearby samples are redundant must be resolved next. For ordinary kriging this is of less concern since the covariance matrix **A** and the data declustering technique that was applied in chapter 3 accounts for possible redundancies. However, the program Krige includes options for the sector search as it can be seen in figure 4.19, and thus the number of points in a search sector can be limited to reduce the influence of redundancy. Limiting the search circle to 1 sector and a maximum number of 8 points per sector, if this sector has fewer samples than the maximum allowable, 8, then all the samples it contains are kept; but, if the sector contains more samples than 8, then only the closest 8 are kept. Figure 4.20 shows the samples that are kept (bold-face marks) from the original set of nearby samples during the process of kriging in this particular neighborhood. It also shows how the Krige program goes during the kriging estimate calculations by displaying intermediate results. There is a search and a kriging estimation in all of the 100 points of the grid as it was specified in figure 4.19 (see grid parameters : 10 divisions in the x-direction and 10 in the y-direction). Finally, figure 4.21 shows the kriging results that were obtained block by block within a 10 x 10 node grid and the exponential variogram model (figure 4.6). The small "x" marks of figure 4.21 are not representing missing points but the sampled locations.
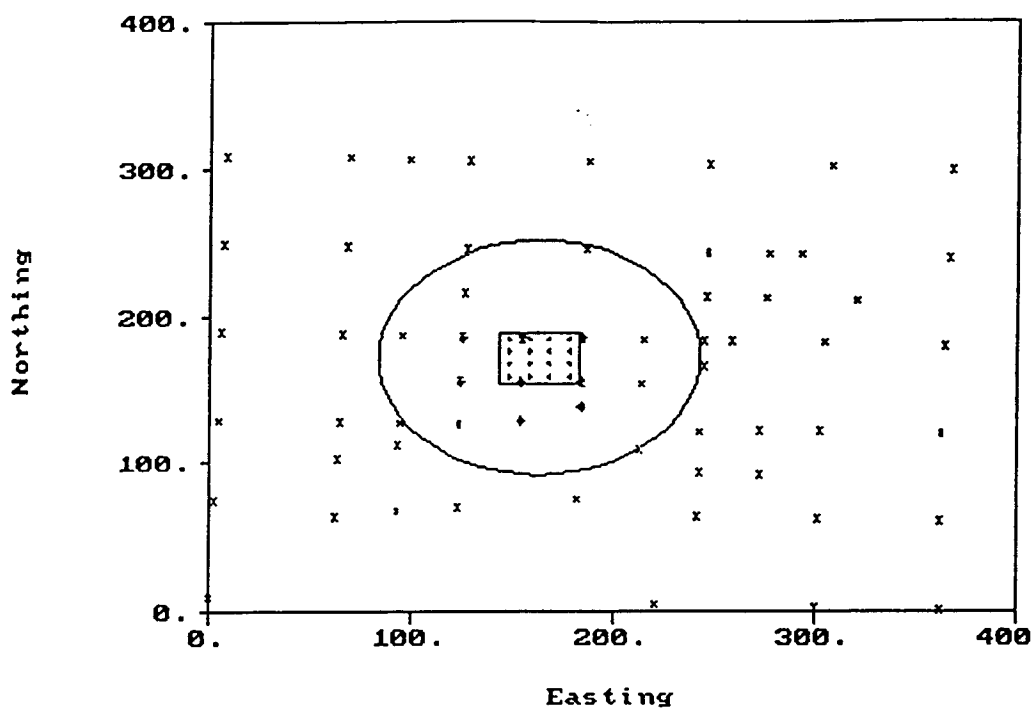
Figure 4.20 Intermediate kriging results during the kriging process. The coordinates of the point of the 10 x 10 grid under search is (163.2 E, 171.7 N). Note the axes have different scales, so the 80-foot radius circle is displayed as an ellipse.
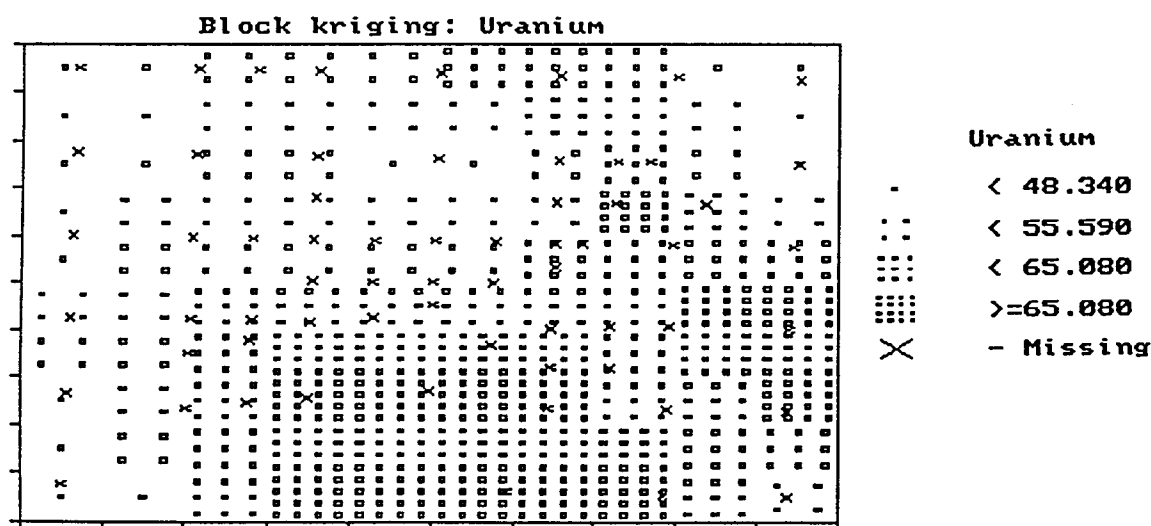
Figure 4.21 Block kriging estimates performed at Fernald site. The size of the kriging block is 40.8 feet by 34.3 feet.

4.9 Computer codes

GEO-EAS 1.2.1 is available from EPA. It is a collection of interactive tools for performing two-dimensional geostatistical analyses of spatially distributed data. The code uses the covariance values, rather than variogram values for solving the kriging matrix equations since it results in a greater computational efficiency [3.3]. GSLIB is a library of computer codes developed at Stanford University by Deutsch and Journel in 1990. These codes were installed on a PC 486/50 at the Radiation Center computing facilities at OSU.

Additionally, figures 6.14 and 6.15 were generated using the commercially available software package Sigma Plot for Windows version 1.02 which was installed on a PC at the Battelle PNL facilities in Richland for the purpose of this research.

4.10 References

4.1   Isaak E. H. and Srivastava R. M., 1989. "An Introduction to Applied Geostatistics." Chapter 13, 330. Oxford University Press, Oxford, NY.

4.2   Delfiner P. and Delhomme J. P., 1975. "Optimum Interpolation by Kriging." Display and Analysis of Spatial Data Nato Advanced Study Institute. John C. Davis and Michael J. McCullagh, ed., John Wiley and sons, New York.

4.3   Barnes M. G., 1978. "Statistical Design and Analysis in the Cleanup of Environmental Radionuclide Contamination", Desert Research Institute, University of Nevada System, NVO 1253-12. p. 15.

4.4   Englud, E, April 1991. "Geostatistical Environmental Assessment Software User's Guide." Section 10, 10-5.

5. DETECTOR LABORATORY INVESTIGATION

5.1 Introduction

Laboratory experiments were conducted, independently, at the Oregon State University Radiation Center (OSURC) facilities with the current detector prototype. The experiments included not only the analysis of the detector response to ^{238}U and ^{90}Sr but also its response to intermediate-energy beta emitters such as ^{137}Cs and ^{154}Eu.

The detector prototype, for the purpose of this laboratory investigation, is composed of the following parts: the radiation detection system, the microcomputer palmtop and the 18-V battery. The detector system includes not only its active area but also the electronics it contains. The microcomputer palmtop constitutes the communication means between detector and user. Data transmitted from the detector are showed on the microcomputer's display. A datum is the number of counts that have been obtained during each count interval. A count interval duration has been set at 300 seconds. The 300-second time interval was considered to be long enough as to give accurate measurements. The basis for the setting of this time-count standard are both the detector's sensitivity to background and its statistics. The current prototype distinguishes from the one used at Fernald in its higher speed processing electronics, which allows decreasing the count interval duration down to 300 seconds (from 900 seconds with the previous detector prototype).

The 18-V battery supplies the power needed to both the detector's circuitry and the microcomputer. A full charged battery can keep supplying to the system for as long as 5 hours provided that the strength of the radioactive source standards is about 100 pCi/cm^2.

The microcomputer palmtop is equipped with two 1.5-V batteries. When the two batteries reach a discharge voltage of about 1.2 V (2.4 V total), the microcomputer will issue the message "main battery is low" on its display. The two batteries shall be recharged or replaced by a new set. It is important to follow carefully the directions showed on the palmtop backside. A backward replacement of the batteries could

result in the deletion of the information stored in the computer's flashdisk, "dobeta" will be lost and the detector operation interrupted. This removable flashdisk contains the software, "dobeta", that controls the internal operation of the detector.

When the detector is disconnected from a discharged battery and reconnected again to a new one, it has to be reset by disconnecting it from the battery for about 15 seconds. Back to operation mode again, the detector will stop itself counting about 10 seconds later. After this occurrence, the detector will behave until the 18-V battery discharges down to 11.5 V.

Finally, the aims of this laboratory investigation are the determination of the detector conversion factors to activity units such as pCi/g, and its response to different beta-energy emitters. Furthermore, a procedural guide is developed to help operate the detector prototype.

All the aliquots that were used at the OSURC facilities for the investigation purposes were obtained from their parents sources which were prepared and sent from Battelle PNL, Richland, WA. Directions for the aliquot preparation were given as well.

5.2 Sample preparation

For the laboratory investigation, basaltic soil samples spiked with $UO_2(NO_3)_2$ and filter paper samples stippled with solutions of ^{238}U, ^{90}Sr, ^{137}Cs and ^{154}Eu were prepared.

5.2.1 Sand samples

Three samples of surrogate soil were sent from Richland (PNL spiked sand). The soils contained sand which was spiked with different activities of $UO_2(NO_3)_2$: 5, 15 and 35 pCi/g. Each sand sample was mechanically blended for 15 minutes to obtain a homogeneous mix. After the mix was completed, the sands were placed on a plastic tray measuring 42.5 x 62.5 cm^2. Each sample was made of 1,500 cm^3 of sand

uniformly spread on the tray and reaching a depth of about 0.5 cm. A very thin plastic layer was set on the bottom of the tray to prevent contamination and to facilitate the sand loading and unloading.

5.2.2 Filter paper samples

Very thin sheets of filter paper were stippled with acid solutions containing the following radionuclides of interest: ^{238}U, ^{90}Sr, ^{137}Cs and ^{154}Eu. The size of the filter paper is about the same as the detector's active area, 40 x 60 cm^2. It was prepared three aliquots out of each different parent solution. Each filter paper was attached to a very thin transparent plastic layer and placed on a plastic tray to prevent tray contamination.

In order to determine the volume of solution that would be required for each filter paper, preliminary experiments were run. A solution containing FeCl$_3$ (1 mg/ml) in 0.1 N HCl was prepared and pipetted homogeneously 1 in. apart on the filter paper. The same was done with a solution containing KMnO$_4$ (1mg/ml) in distilled water. The latter solution cast better visual understanding of the process. The full coverage of the filter paper with the KMnO$_4$ solution was obtained with 16 ml of solution, with 1ml being equal to 35 drops, and thereby this amount was used as a reference to stipple the 42.5 x 62.5 cm^2 filter papers. Previously to this experiment, it was tried pipetting the solution on the filter paper 0.5 in. apart. This amount of solution was excessive. Once the volume of solution was determined, filter papers were stippled with radioactive solutions and left to dry for about 30 minutes before counting.

a) U-238 sample

Three solutions with the specific activities of 600, 6000, and 6 x 10^4 pCi/ml respectively, were prepared by diluting a portion of the parent solution in 0.1 N HNO$_3$ until the required dilution level was obtained. After these solutions were applied to the filter papers, the specific activity per unit area was found to be: 3.86, 40.5 and 373 pCi/cm^2, respectively. These values are correct provided that the parent solution

that it was given to us by PNL contained a total activity of 15 μCi. However, further investigations concluded that the total activity was 1.5 μCi. This final value is consistent with the second figure of 1.516 μCi that PNL gave us upon request. Therefore, the real activities used to stipple the filter paper are 10 times lower.

b) Sr-90 samples

Three similar solutions were prepared out of the parent solution (2.45 μCi of ^{90}Sr in 25 ml of 0.5 M HCl) containing 600, 1560 and 6000 pCi/ml, respectively. After the spread on the filter paper, the papers surface activities were 3.78, 9.89 and 37.5 pCi/cm^2, respectively. In all cases, the three 20-ml solutions were obtained by mixing an aliquot of the parent solution with the corresponding volume of a solution 0.5 M HCl.

c) E-154 samples

The parent solution was 21 ml of 0.1 N HCl containing 8.81 μCi of ^{154}Eu. The three daughter solutions had specific activities of 2.4 x 10^4, 5 x 10^4 and 1x 10^5 pCi/ml respectively, and thus the filter papers were stippled with 150, 376 and 625 pCi/cm^2 respectively. The PNL reported parent solution volume was 23 ml; however the volume measured at OSURC was 21 ml. The doubt about the accuracy in the activity of the parent solution arose because the preparation records of wether the PNL supplied activity was based on the total volume or on the per-unit volume were not available. It was assumed a parent solution activity of 8.81 μCi/21 ml = 0.42 μCi /ml.

d) Cs-137 samples

The three daughter solutions were obtained from the parent containing 2.156 μCi of ^{137}Cs in 16.5 ml of 0.5 N HCl. This parent solution was not of 19 ml as it was reported on the PNL data information that accompanied the radioactive sources. Consequently, the supplied volumetric activity or total activity of the parent solution might be questionable. The daughter solutions contained the following specific

activities 2.5 x 10^4 (203.13 pCi/cm^2), 1.64 x 10^4 (102.5 pCi/cm^2) and 1x 10^4 pCi/ml (62.5 pCi/cm^2). Only the two first were counted. By the time the third sample was ready, the detector was not available.

5.3   Counting technique

The following steps listed below show the procedural guide on how to operate the detector in order to achieved the minimum practical error in the measurements and the maximum detector linear response. It also sets the way to control the different parts of the detection system and their interrelation. For each sample, a set of measurements of ten to twenty 300-second counts was repeated in order to have better detector statistics. However, due to some technical and time limitations, some sets contain less than ten 300-second counts.

1. Set the source right beneath the detector's active area, so that detector and source will be almost in direct contact.

2. Set the computer palmtop to count by typing at the C:> prompt "dobeta". At about 10 seconds from the beginning, the system will stop. Press escape and retype "dobeta" at the C:> prompt. From now on the detector will perform 300-second counts; however the detector's counting must be initiated each 300 seconds. After each count, a display of the total and per-second counts will be shown.

3. Before the beginning of any count in the presence of radioactive sources, background should be measured. Background is about 7 cps. Since this prototype proved to be sensitive to gamma radiation fields, it would be advisable to check for them during background measurements. These fields will limit the detector beta sensitivity.

4. To determine the activity of a given source, it would be reasonable to perform a set of seven 300-second counts, so that the first set of three or four is discarded. This is due to the observed fluctuations at the beginning of each set of counts. The remaining counts will be averaged to determine the detector final count.

5. Three counts at least would be advisable to take after the rejection of the previous set in order to limit average errors to 3.3 %. Should just one count be registered, maximum average errors would be about 10.3 %.

6. RESULTS

6.1 Detector laboratory investigation results

These results are summarized in figures 6.1 through 6.10 and table 6.1. They show a detector response fairly linear for the samples of ^{238}U-spiked sands, ^{90}Sr, ^{137}Cs and ^{154}Eu stippled filter papers. A very satisfactory linear fit was found for the ^{238}U-spiked sands and ^{154}Eu samples with determination coefficients of $r^2 = 0.9671$ and $r^2 = 0.9571$, respectively (fig. 6.1 and 6.4). Each of the three squared marks in the graphs is the result of averaging the detector readouts for each set of counts.
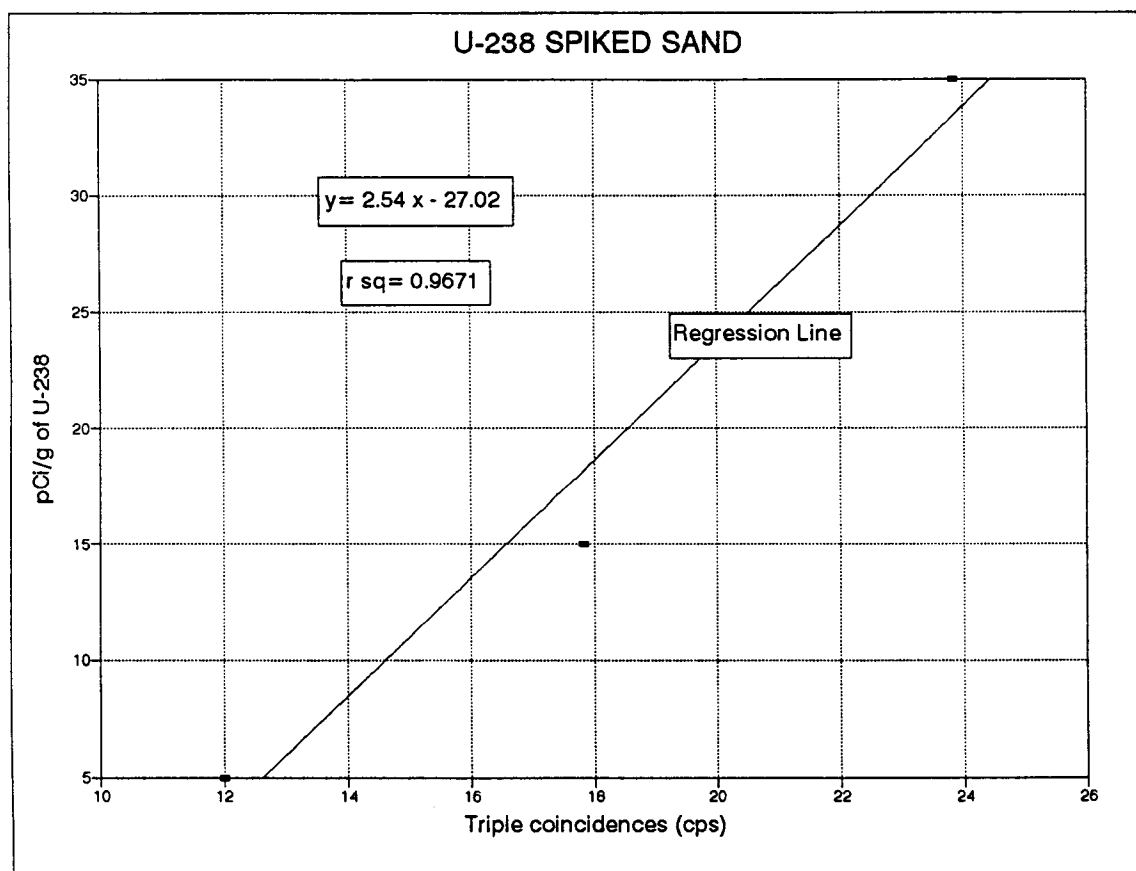
Figure 6.1 Detector response to uranium spiked sand. The three aliquots specific activities are 5, 15 and 35 pCi/g.

Figures 6.2 and 6.3 display the linear responses for ^{238}U and ^{90}Sr stippled filter paper respectively with $r^2 = 0.9999$. On the other hand, the regression line of figure 6.4 is a good fit for the low-energy beta emitter ^{154}Eu stippled on filter paper with $r = 0.9783$ ($r^2 = 0.9571$).
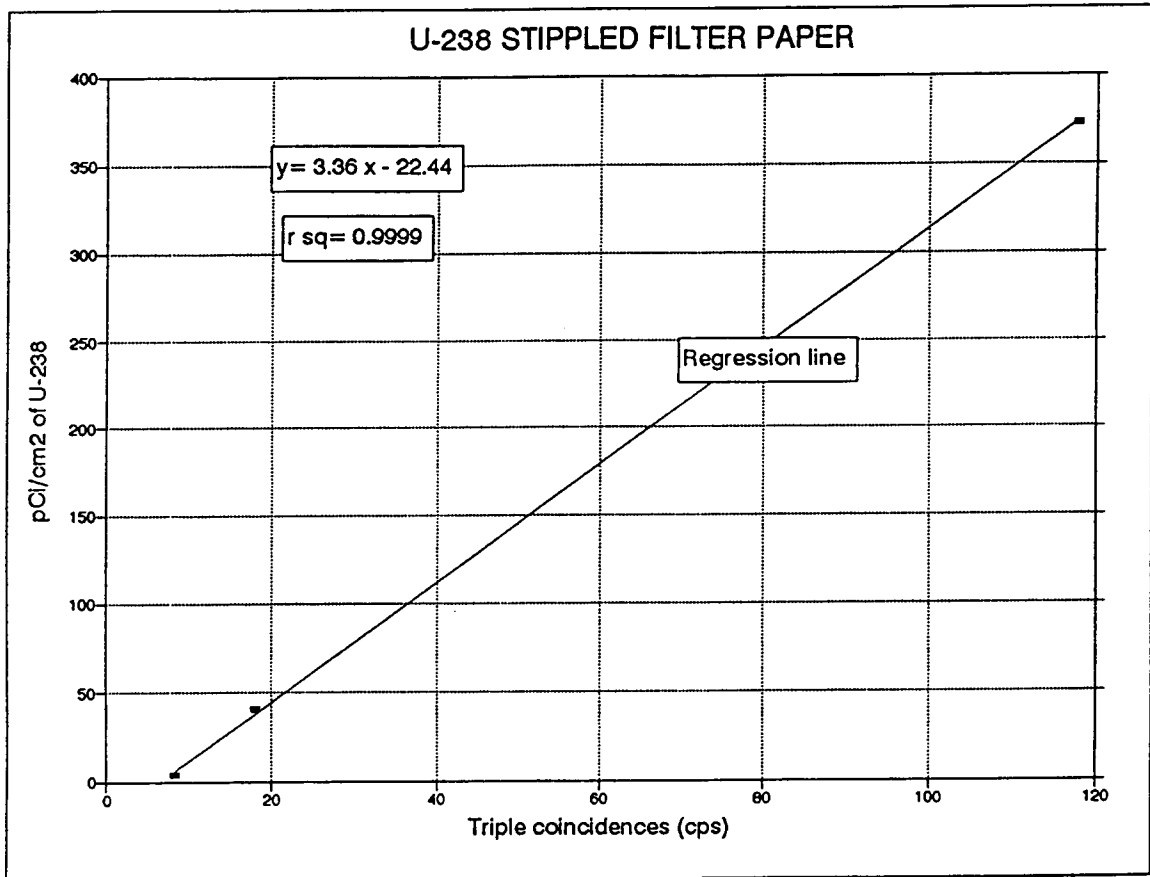
Figure 6.2 Detector response to ^{238}U stippled filter paper. The three aliquot activities are 3.86, 40.5 and 373 pCi/cm^2.
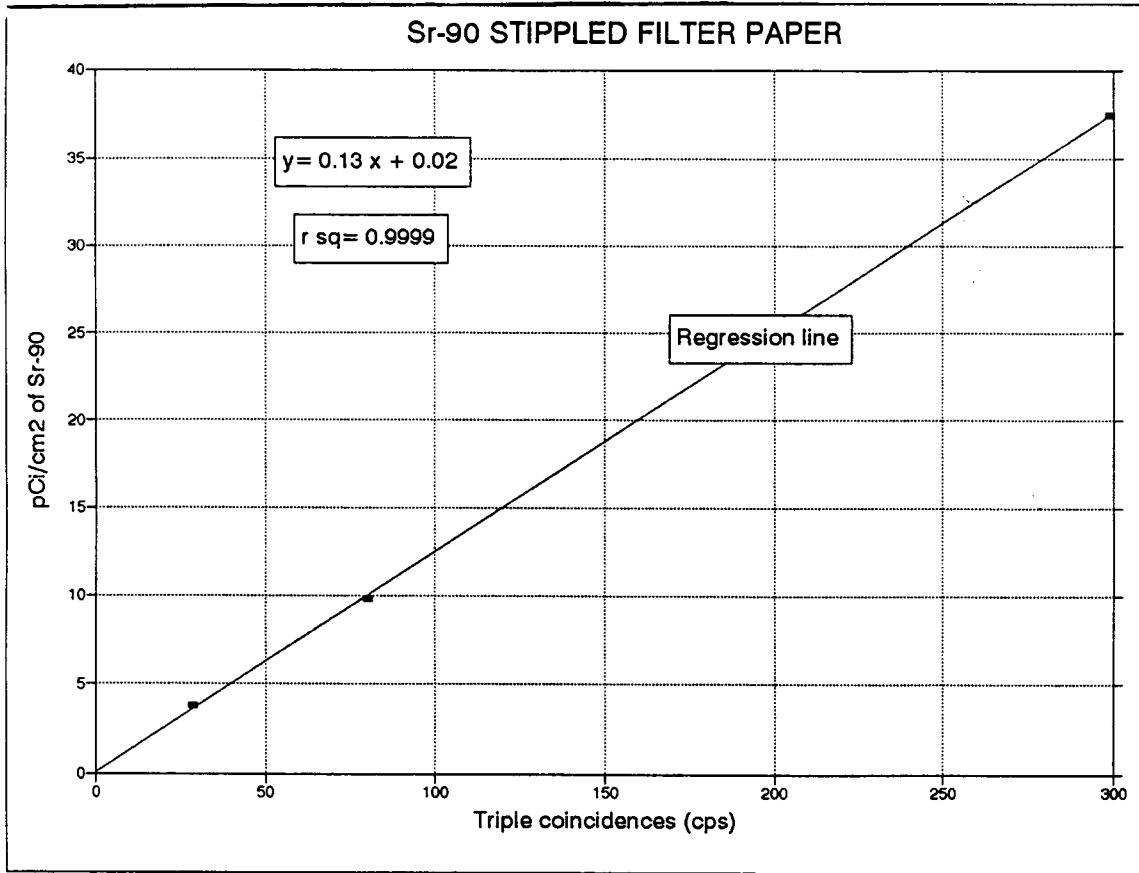
Figure 6.3 Detector response to ^{90}Sr stippled filter paper. The three aliquot activities are 3.78, 9.89 and 37.5 pCi/cm^2.
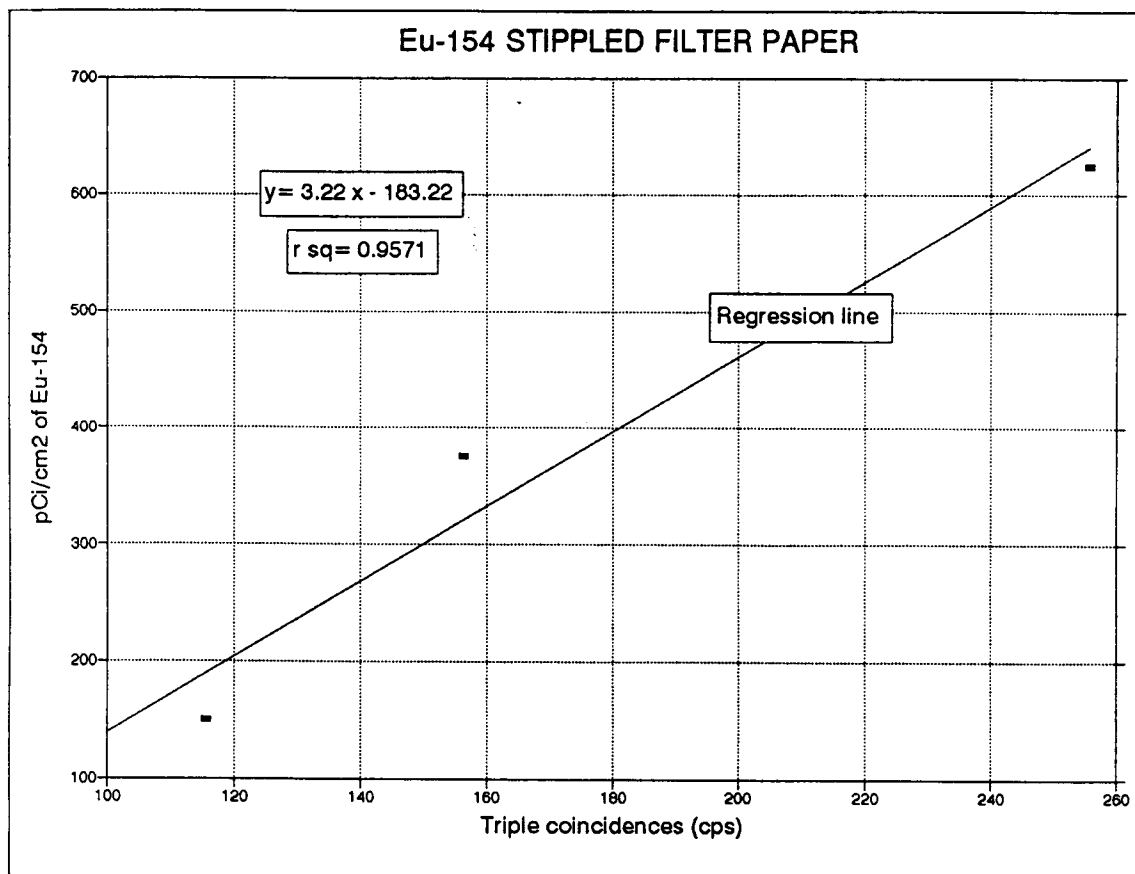
Figure 6.4 Detector response for ^{154}Eu stippled on filter paper. The three aliquot activities are 150, 376.5 and 625 pCi/cm^2.

Systematic oscillations were observed at the beginning of each set of measurements. The reason is not clear yet. Appendix 3 shows the results of the countings for each sample (also see appendix 2). Therefore, the first three 300-second counts of each set of measurements were rejected. Substantial improvement in the new set of errors were observed. Table 6.1 shows the systematic average errors found after and before the rejection of the three first set of counts for each sample. In general, ^{238}U and ^{90}Sr samples presented lower errors.

Since maximum registered values are the most significant in terms of radioactive contamination and its risk when the characterization of a site comes to scrutiny, the errors are calculated based on the maximum values recorded during the counting. Although the differences between errors after and before rejection are remarkable, the differences of the means after and before rejection are quite small.

Table 6.1 Error comparison obtained after and before discarding the first three 300-second counts.

Radionuclide (pCi/cm^2)	Mean$_{after}$ (cps)	Average Error$_{after}$ (%)	Mean$_{before}$ (cps)	Average Error$_{before}$(%)	Radio nuclid. #
Sr (3.78)	28.80	1.1	28.8	1.1	1
Sr (9.89)	80.38	0.9	80.38	0.9	2
Sr (37.5)	299.25	1.3	298.96	1.4	3
U-238 (3.83)	8.31	0.9	8.38	2.6	4
U-238 (40.5)	18.15	2.5	18.42	10.3	5
U-238 (373)	117.72	1.4	117.72	1.4	6
E-154 (150)	115.55	1.4	115.61	1.7	7
E-154 (376.5)	154.96	1.4	156.48	4.6	8
E-154 (625)	255.08	1.2	255.91	1.5	9
Cs-137 (102.5)	28.89	3.3	28.42	7.2	10
Cs-137 (203.1)	62.83	1.1	62.95	2.0	11
U-spiked sand (5 pCi/g)	12.03	2.1	11.99	2.1	12
U-spiked sand (15 pCi/g)	17.86	1.8	17.83	2.1	13
U-spiked sand (35 pCi/g)	23.49	1.4	23.83	4.0	14

Figure 6.5 shows the improvement of the errors after the rejection of the undesirable first three counts. Figure 6.6, on the other hand, displays the quasi-invariability of the mean of the detector readouts after and before the rejection process. This proves that the majority of the partial counts of each set are around the mean, with some outliers generally being found among the rejected set. Interestingly enough, the most pronounced difference occurs within the interval numbers 7 to 9 and 10 to 12 which happens to be where the low-energy beta emitter ^{154}Eu and ^{137}Cs samples lie.
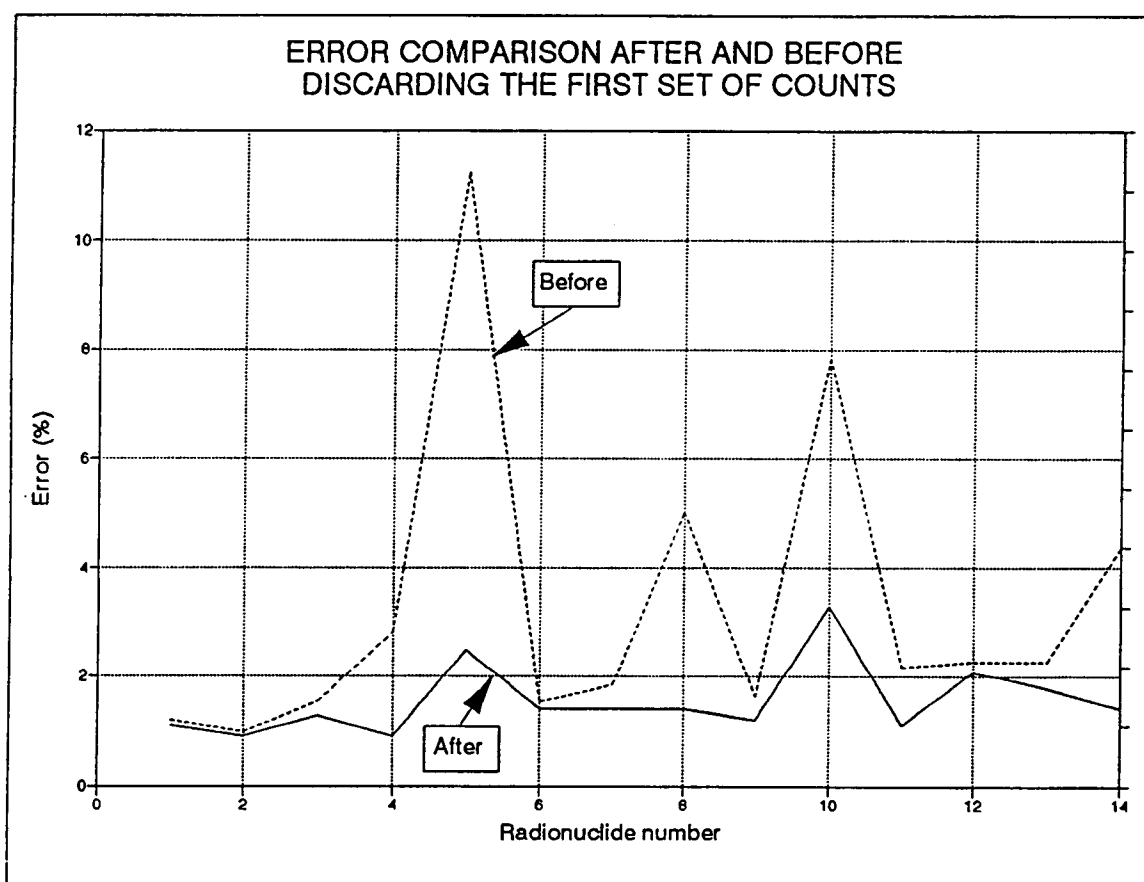
Figure 6.5 Error comparison before and after rejection of the first set of counts.

MEAN-COUNT COMPARISON AFTER AND BEFORE DISCARDING THE FIRST SET OF COUNTS
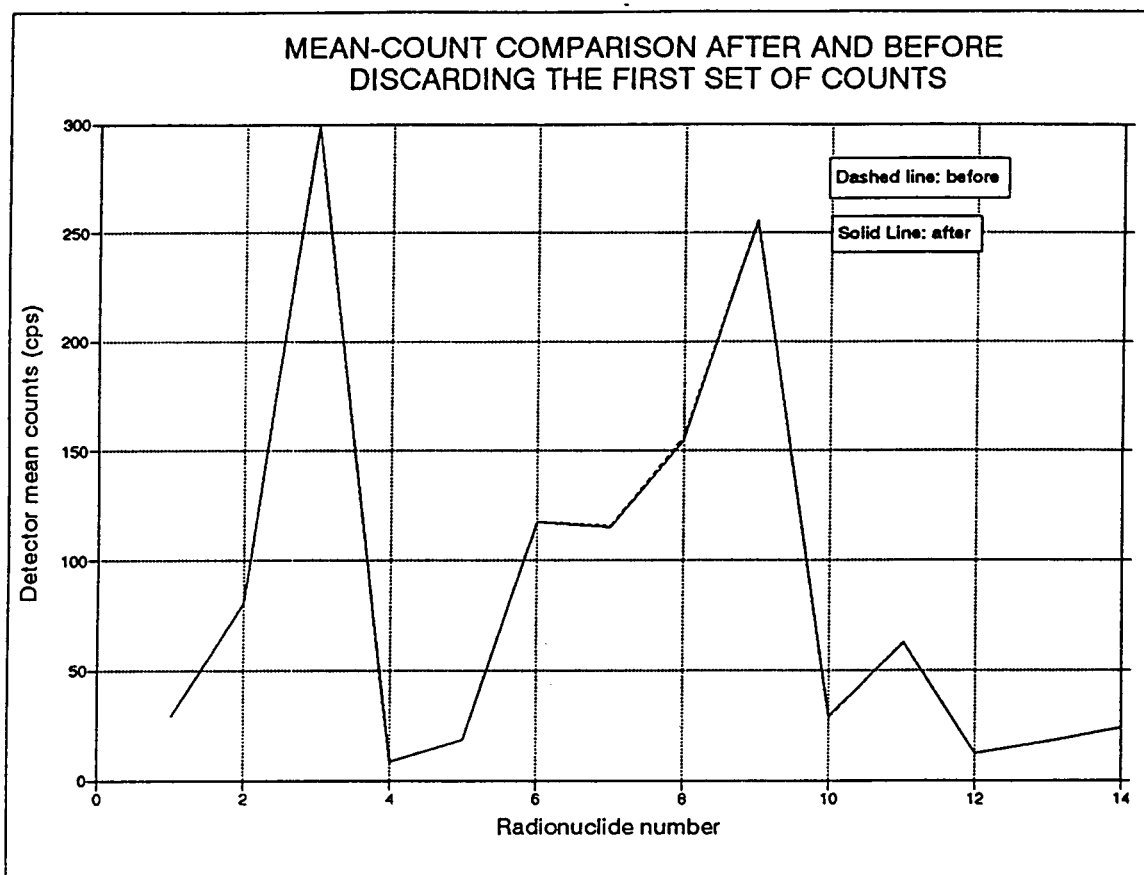
Figure 6.6 Mean-count comparison before and after rejection of the first set of counts.

The 18-V battery of the detector plays an important role among the components of the whole prototype system. Its discharge behavior thus has been investigated as well. Figures 6.7 through 6.9 show the detector's 18-V battery's discharge pattern. They first display a zone of a smooth discharge which extends up to 14 V (figures 6.7 and 6.8). After that, a raising in the discharge rate prolongs until the battery reaches 11.5 V, the discharge value.
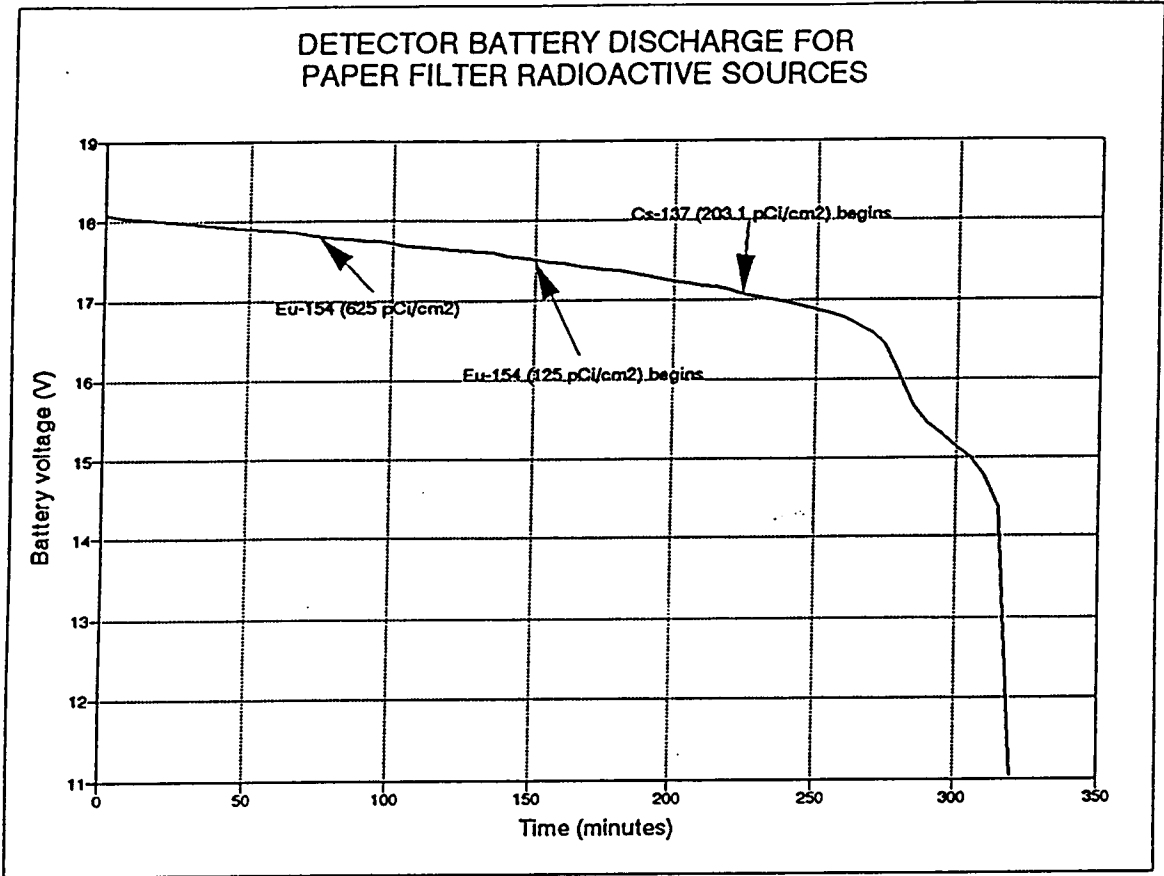
Figure 6.7 Detector battery discharge behavior for filter paper sources.
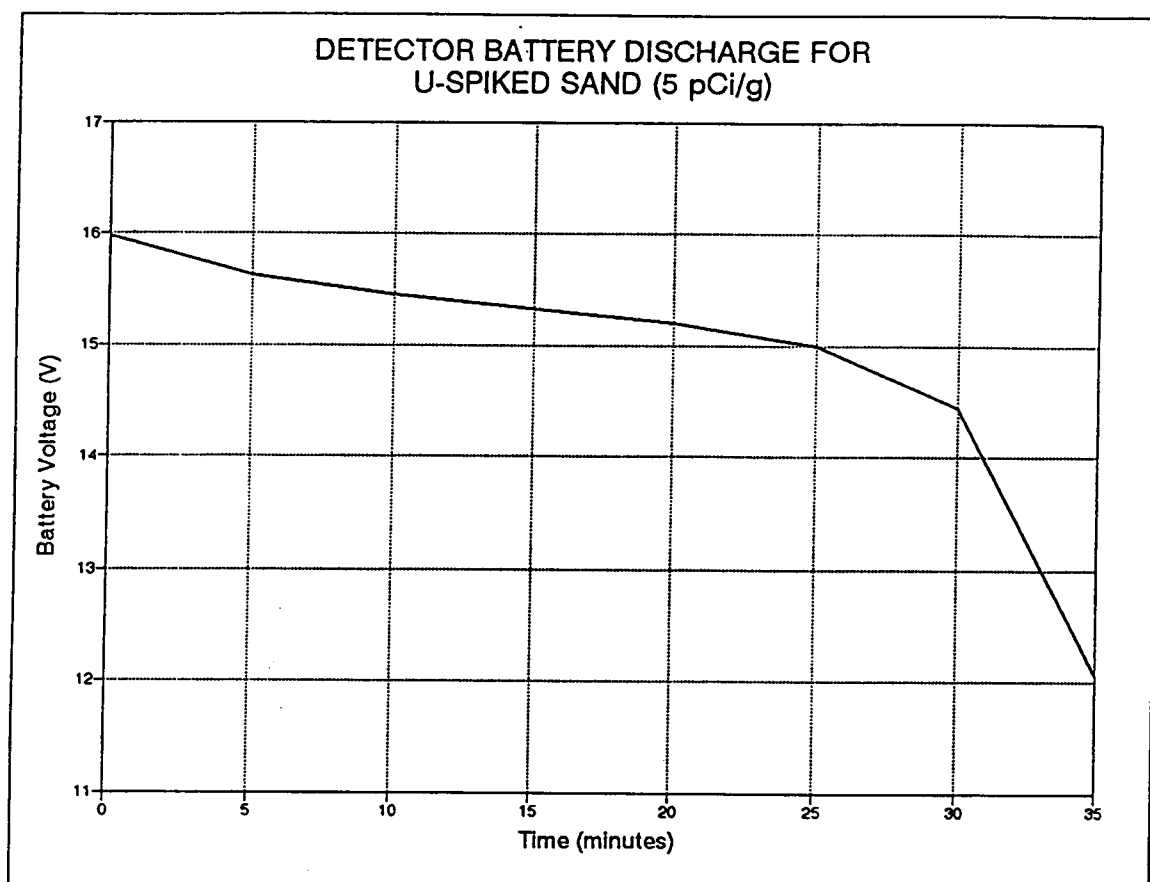
Figure 6.8 Detector battery discharge behavior for the 5 pCi/g uranium-spiked sand.

Figure 6.9 on the next page shows a very steep slope in the 17.5V-14.75V range which is unusual and it might be due to the fact that two different twin batteries were used during the running of the experiments.
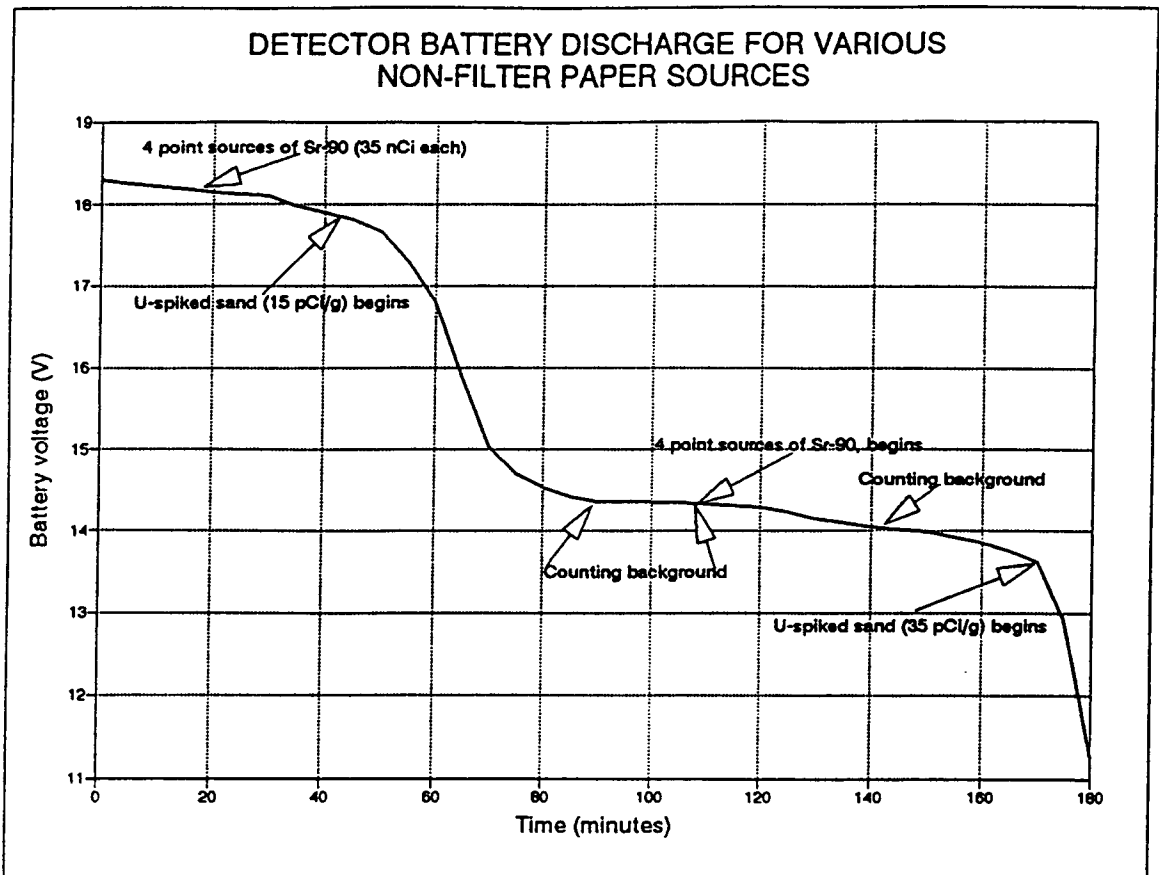
Figure 6.9 Detector battery discharge behavior for various non-filter paper sources.

Figure 6.10 shows what the background readouts look like. A substantial increase of about 20% was detected during the experiment. It is most likely due to the presence of gamma radiation fields stemming from the OSTRIGA (Oregon State Training Research Isotope Production by General Atomic) nuclear reactor operation at full power. OSTRIGA reactor operation gives off the short-lived ^{16}N whose gamma emissions are as high as 7.12 and 6.13 MeV.
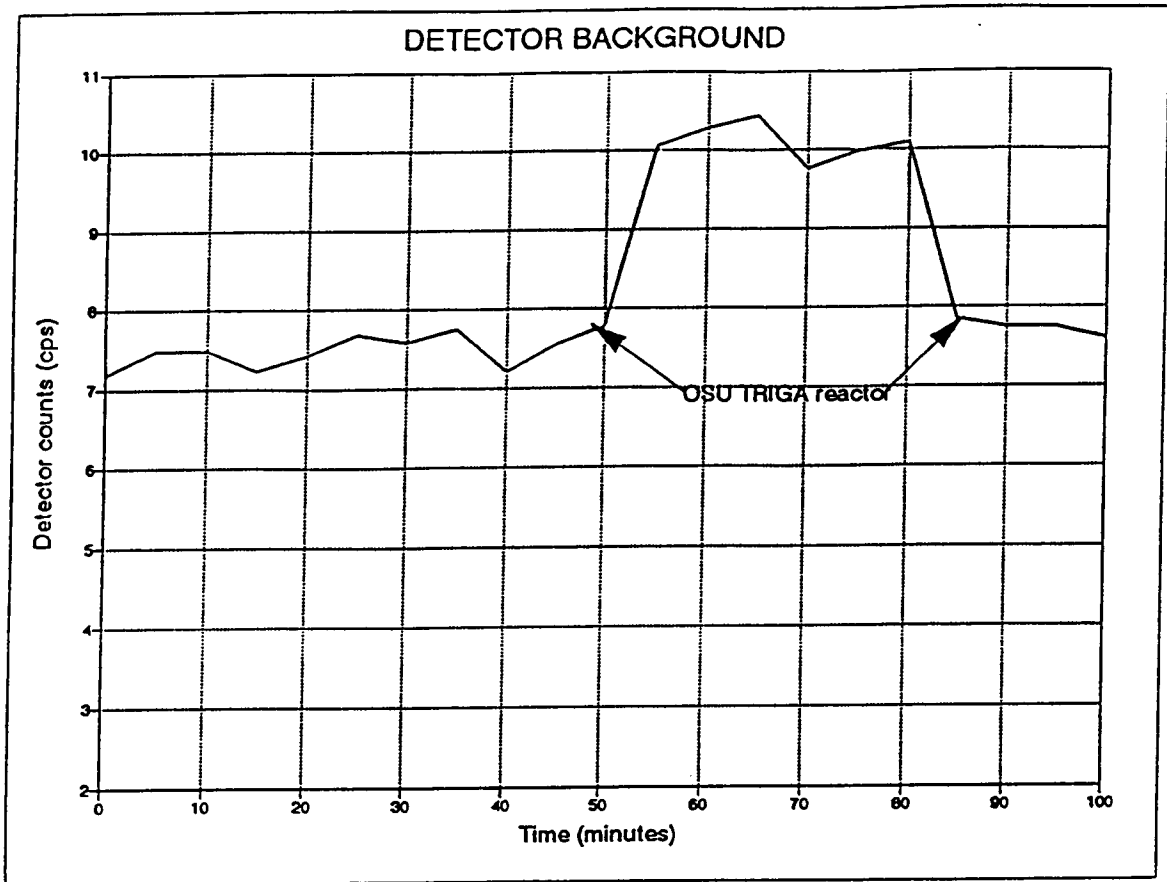
Figure 6.10 Detector laboratory background. Note the background rise during OSTRIGA reactor full power operation.

Appendix 2 shows the normal probability distribution of each single set of counts performed for each of the 14 samples. Its use constituted one intermediate step in the errors determination and also gave a very good insight on the detectors statistics. All of the appendix plots show that the distribution of the detector counts lay in a quasi-linear fashion, and this feature thus suggests a Gaussian behavior of the detector statistics.

6.2 Fernald Incinerator Site results

The locations at which estimates were kriged form a two dimensional grid covering the whole Fernald Incinerator Site. The origin of the grid is defined at the south-west corner of the target field, where the incinerator is located, and a coordinate system was superimposed on this field with the origin being (0 E, 0 N) (see figure 3.1). The grid spacing was set at 40.8 feet in the east direction (x axis) and 34.3 feet in the north direction (y axis). The grid extends a maximum of 10 divisions east and 10 divisions north, totaling 100 grid nodes. The maximum number of data retained in each kriging neighborhood was 8, with a minimum of 1. The search radius was 80 feet. The block size selected for the kriging was 40.8 feet by 34.3 feet, with 16 discretization points (figure 4.20). The variogram model used to practice the kriging was of exponential type with no nugget effect, a range of 240 feet and a sill of 145 (figure 4.6). With these parameters, the variogram model function was found to be $\gamma(h) = 145 \, (1-e^{-0.02 \, h})$ and the covariance function $K(h) = 145 \, e^{-0.02h}$ with h being the variable distance. Under these restrictions, the maximum dimension of the kriging matrix **A** was n+1 by n+1, or, 9 by 9. The maximum number of sectors needed to estimate a location was 1, and as far as there is at least 1point then it will be an estimation. These results are quite reasonable, since it was found that, in general, the ordinary kriging with block estimates are not very sensitive to the number of data in the kriging neighborhood provided this number is greater than or equal to 8.

6.2.1 An example illustrating the estimates provided by OK

The example selected to illustrate the calculations and main features of the estimation method by ordinary kriging (OK) consists of 8 data surrounding a specific block location within the site. The coordinates of the center of the block are 163.2 E and 171.7 N. Figure 4.20 shows the location of the block, illustrated by a rectangle, and the 14 data found within the radius of 80 feet. Only a maximum of 8 data (the

bold-faced marks) were used for estimation. Table 6.2 shows the elements of the covariance matrices $A(I,J)$ and $Z(I)$ which must be known to compute the vector w and thus the estimate and error variance, σ^2_{OK}. Note that as the distance between pairs increases, the covariances decrease.

Table 6.2 Debug results showing the elements of the two covariance matrices for the point kriged (163.2 E, 171.7 N) and its 8 closest neighbors.

```
Debug results for variable :Uranium
             Point kriged is :(   163.200,    171.665)

2(I)     A(I,J):
113.982     145.000  99.636  99.657  86.071  72.704  99.636  85.294  71.997   1.0

110.403      99.636 145.000  84.563  99.657  94.227  85.294  99.636 104.766   1.0

103.649      99.657  84.563 145.000  99.636  80.568  68.486  62.331  65.146   1.0

102.292      86.071  99.657  99.636 145.000 117.241  63.031  68.486  88.279   1.0

 87.463      72.704  94.227  80.568 117.241 145.000  56.036  66.268  98.025   1.0

 86.578      99.636  85.294  68.486  63.031  56.036 145.000  99.636  65.191   1.0

 85.104      85.294  99.636  62.331  68.486  66.268  99.636 145.000  87.551   1.0

 83.059      71.997 104.766  65.146  88.279  98.025  65.191  87.551 145.000   1.0

  1.000       1.000   1.000   1.000   1.000   1.000   1.000   1.000   1.000    .0
```

Table 6.3 shows the estimation result for the point that has been kriged. $X(i)$, $Y(i)$ and $V(i)$ represent the east coordinate, north coordinate and its sampled activity value in pCi/g. The distance, in feet, from the kriged point (the center of the block) to the 8 closest neighbors is in the next column. $W(i)$ are the weights associated to each sample. Note that as the sample becomes farther and farther away, its influence is smaller and so its weight. The estimate is 51.0 pCi/g and the error variance, σ^2_{OK}, is 5.85 or the standard deviation is 2.42 pCi/g. The constant C_{VV}, which is determined by the variogram model, is 115.283. Finally, the obtained value of the Lagrange parameter, μ, is 1.068.

Table 6.4 shows a comparison of the variation of the error variance with the number of discretizing points within the block used for kriging. It shows that as the number of discretizing points increases, the error variance significantly decreases.

However, the estimate stayed invariant at 51.0 pCi/g as the number of discretizing points varied.

Table 6.3 Debug results showing the results of the estimate. Estimate, error variance, weights and Lagrange parameter have been computed.

```
         Point kriged is :(    163.200,    171.665)
     X(i)           Y(i)           V(i)       Distance         λ(i)
-------------------------------------------------------------------
     155.           185.           56.2          15.7           .339
     154.           155.           46.4          19.0           .282
     185.           185.           42.6          25.6           .181
     184.           155.           57.3          26.7           .171
     184.           138.           55.1          39.6       -.880E-02
     125.           186.           51.6          40.8        .244E-01
     124.           156.           57.2          42.2        .209E-01
     154.           129.           62.9          43.6       -.976E-02

  Neighbors:              8     Σ Weights:        1.000
  Estimate:       51.0                 CVV:     115.283
Stand.dev. (σ):   2.42          Σ WiB2i:     108.365
      σ²ₒₖ:       5.85                   μ :       1.068
```

Table 6.4 Error variance (σ^2_{OK}) comparison for different kriging block types.

Block type	C_{VV}	Error variance
4 x 4	115.28	5.85
3 x 3	116.26	6.48
2 x 2	119.57	8.23
point	145	28.2

Once the results for each of the 100 nodes of the grid has been computed and the kriging process is over, the map of the geographical distribution of the

contamination in the site could be determined. For this purpose, the program Conrec from the GEO-EAS 1.2.1 package was used. Conrec produces contour maps of variables within a grid using spline interpolation.

6.2.2 Contouring the contamination isopleths

A two-dimensional surface activity contour map was generated with Conrec (figure 6.11). This map showing the lines of equal contamination activities on the surface (isopleths), is quite consistent with the site historical information which indicates that contaminated emissions from the incinerator stack were transported to the north and east across the field site, and uranium activity levels are observed to decrease as a function of distance from the incinerator. As predicted, the surface activity in the soil is greater nearby the incinerator just directly downwind of its stack and decreases in a northeasterly direction.
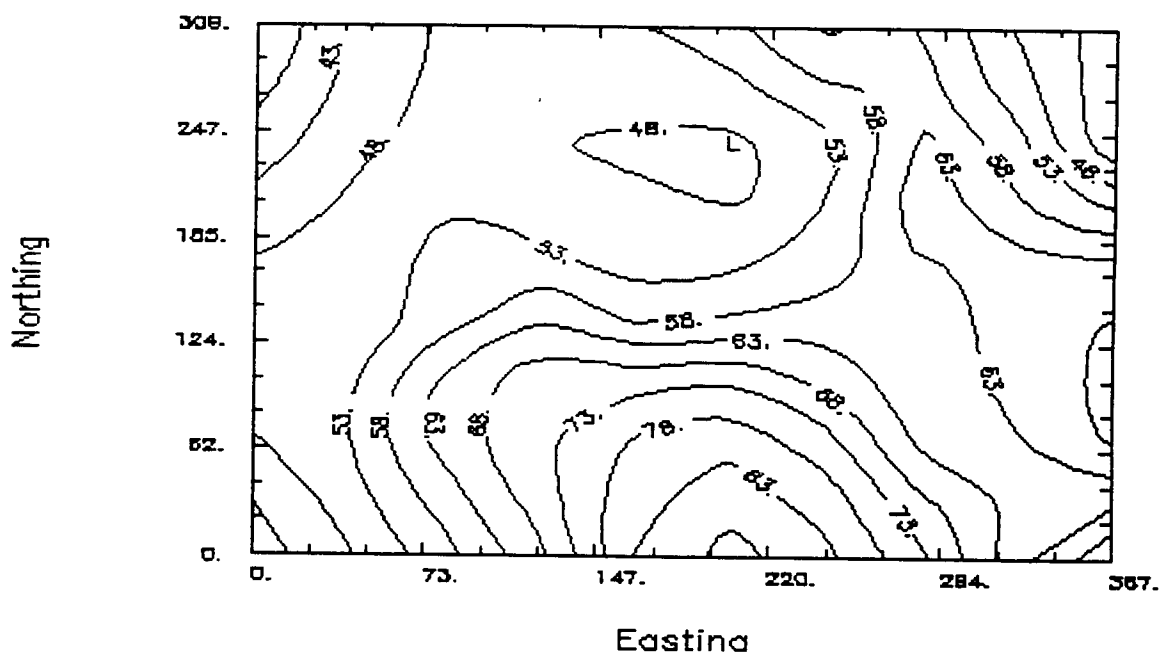
Figure 6.11 Uranium surface activity contour map based on a geostatistical analysis of the beta sensor measurements.

Further support for the beta results are provided by current surface soil analyses and in situ gamma-ray spectrometry measurements (i.e., a high-purity germanium detector suspended 15 cm above the ground), which lead to qualitatively similar contour maps (figure 6.12 and 6.13).
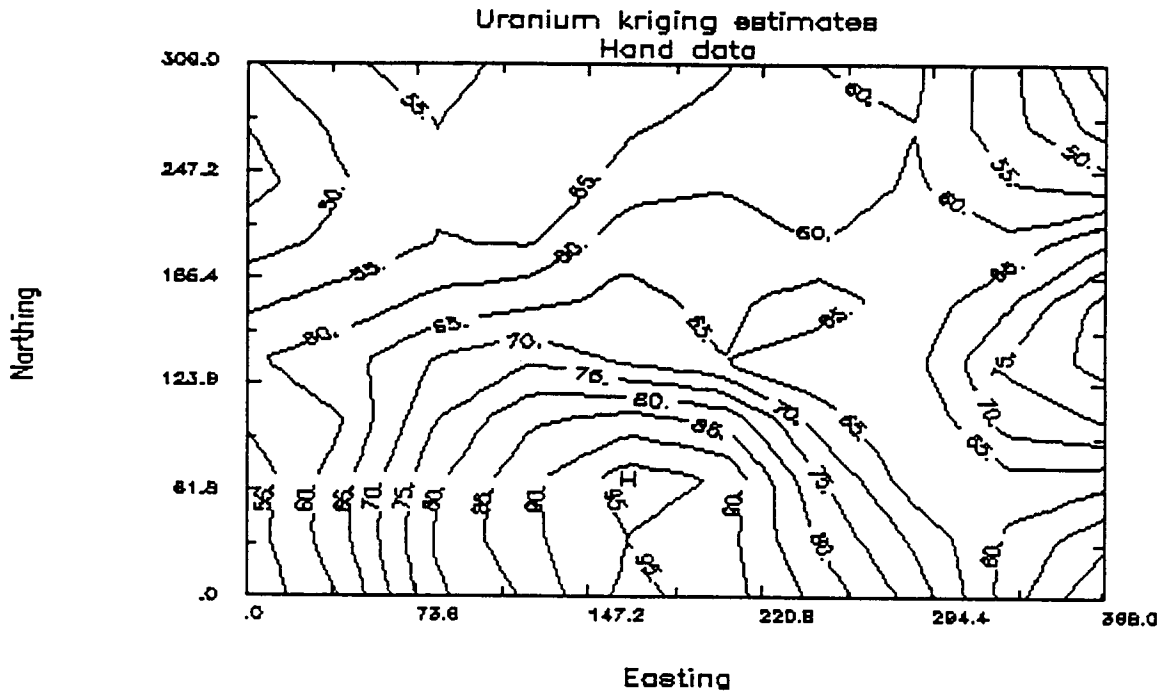
Figure 6.12 Uranium surface activity contour map based on a geostatistical analysis of the hand-sample measurements.
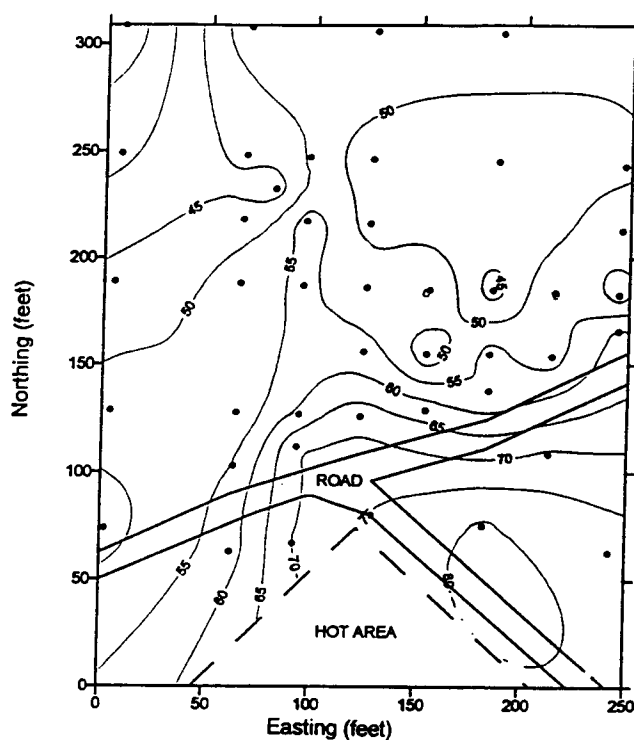
Figure 6.13 Uranium surface activity contour map based on a geostatistical analysis of the in situ gamma-ray spectrometer measurements.

Quantitatively, the results from these three techniques are not equivalent because of the extreme differences in the reach of view for each methodology (i.e., in situ gamma-ray spectrometry > beta detector > soil samples) and the spatial heterogeneity of the source. Hence, actual activity values at each location are highest for the laboratory-obtained soil samples, lowest for the in situ gamma-ray measurements, and intermediate for the beta detector. Despite these quantitative discrepancies, the combined data from these three technologies are quite well correlated (figures 6.14 and 6.15), thereby lending support to the use of the high-energy beta scintillation detector for field measurements of surface activity under various environmental conditions.
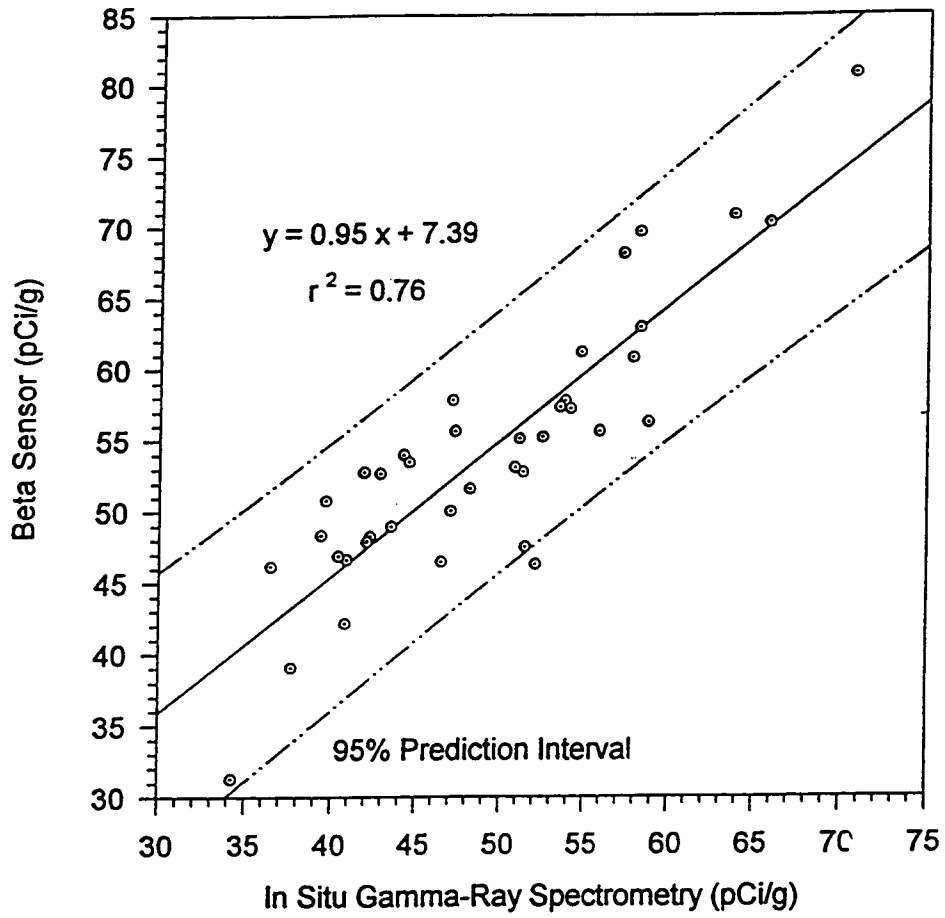
Figure 6.14 Correlated plot comparing the in situ gamma-ray measurements and the beta detector response.
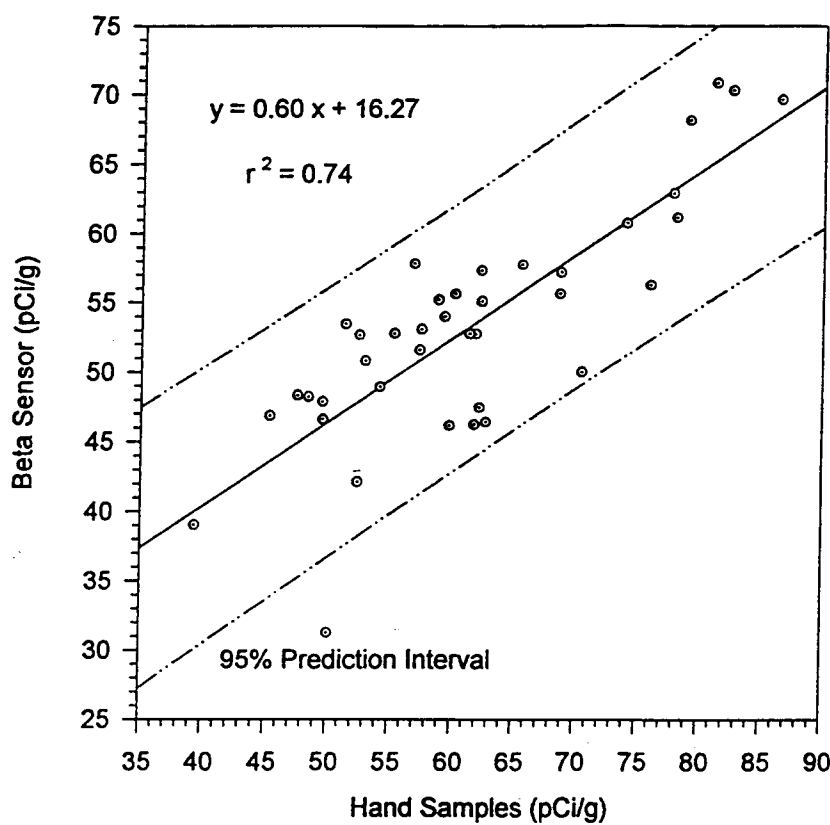
Figure 6.15 Correlated plot comparing the hand sample (laboratory-obtained) measurements and the beta detector response.

The obtained results are associated to some errors or differences between the "true" values and the estimated ones. They were compared, and it was found (see section 4.7) that about 80 % of the kriged estimates are in the interval [-10 %, 10 %] and about 54 % of the estimates fell in the interval [-5 %, 5 %]. In general, the errors are larger as the distance from the incinerator stack increases, which is in reason with the fact that, in geostatistical analyses, as distance increases the influence of pairs located far apart is smaller, therefore chances of accumulating significant errors are greater when including far away pairs. In the center of the field was found a homogeneous error distribution in the range of ± 10 %. The larger errors were found near the edges of the resultant map because there are less sample points, and also a breakdown of the network of the grid samples.

The directional dependence that might be found in the 90° direction does not change noticeably the spatial distribution results of the contamination. The omnidirectional contour map portrays fairly well this spatial distribution and is quite representative of the phenomenon. Therefore, there is no need of the 90° directional-dependence contour map since generally speaking it does not cast additional information.

Figures 6.16 and 6.17 show the estimations obtained by detector and laboratory (or hand) data collection respectively. The similarities are evident. The few differences are likely a consequence of the two distinct methodologies that have been used.
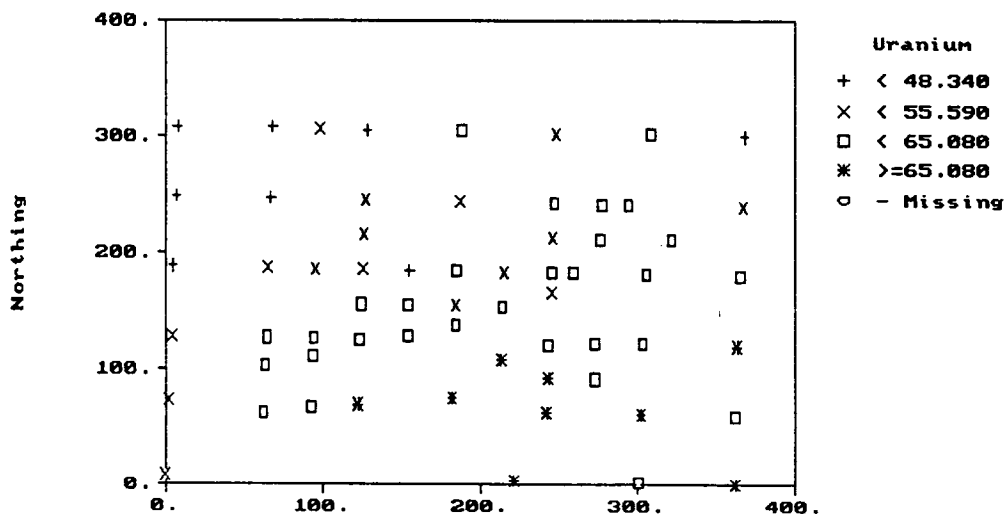
Figure 6.16 Kriged estimations obtained after the data collected with the beta detector.
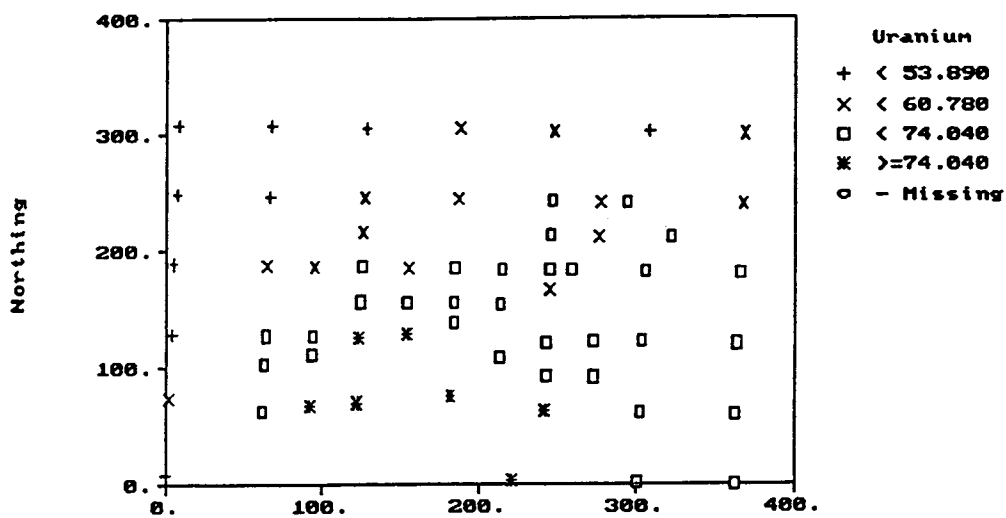
Figure 6.17 Kriged estimations obtained after the data collected with hand sampling and further laboratory analysis.

7. DISCUSSION

Improvements of both the detection system and the modeling methodology are still possible. The kriging results are not definitive. They should not be considered as the best that can be produced from the kriging techniques. Kriging itself is in an evolutionary stage. In this chapter, the replacement of the PM tubes with semiconductor diodes and the placement of a fourth-coincidence layer are discussed. The main purpose of these modifications is to gain energy resolution and to improve beta detection sensitivity while keeping the current detector design.

7.1 Energy resolution

There are several major inefficiencies in the scintillator-photomultiplier arrangement that lead to a relatively poor energy resolution, and discrimination between ^{238}U and ^{90}Sr is impossible. In a photomultiplier, the number of photoelectrons emitted per photon at the photocathode is low; the collection of photons from where they are emitted in the scintillator to the photosensitivity surface of the photomultiplier is incomplete, and the scintillator itself is inefficient.

The origins of energy resolution loss in scintillation technology stem from the combined effects of statistical noise, electronic noise and scintillator noise. These sources cause fluctuations in the response of the detector which ultimately result in imperfect energy resolution. The statistical noise, which is caused by the statistics associated with the charge production in the detector, is reducible to a minimum amount of fluctuation that will always be present in the detector signal no matter how perfect the remainder of the system is made. From a detection viewpoint the statistical noise is the dominant source of fluctuation in the signal.

The limiting value of the detector resolution, R_{limit}, due to statistical fluctuations in the number of electrons collected from the photocathode of the PM tube is expressed as:

$$R_{limit} = 2.35 \sqrt{\frac{F}{N}}$$

where N is the number of electrons generated on the average. The above expression holds if a Poisson distribution for the statistics [7.1] is assumed, and the detector response is approximately linear. The Fano factor, F, is a fudge factor that must be inserted in the equation in an attempt to quantify the departure of observed statistical fluctuations from Poisson statistics [7.2]. R_{limit} depends only on the number of electrons created N, and the resolution improves (R will decrease) as N is increased. From this equation we can deduce what value N should reach to achieve energy resolutions better than 0.54 % so that discrimination between ^{238}U and ^{90}Sr would be theoretically allowed. However, some reasonable doubts arise regarding that discrimination level because of the beta energy spectra associated with theses two radionuclides is virtually the same. Additionally, their beta energy spectra are continuous functions.

In a photodiode, N depends on the photodiode material, its operation mode (i.e., avalanche diode) and the intensity of the dark currents. Diodes have higher quantum efficiency and generate weaker dark currents than PM tubes do. The fraction of dark current that undergoes multiplication in the PM tube could be significant especially at higher than room temperatures. Thereby, N would be similar in both cases and F will influence the final results. Usually, F is much less than unity (~0.12) for the scintillator-photodiode combination than that for the scintillator-PM tube arrangement [7.3].

With no direct way to measure the statistical noise contribution, it was estimated by the following. The production of scintillation photons is about 50,000 assuming a conversion efficiency of 0.123. If all these photons reach the photodetector about 45,000 photoelectrons will be generated if a 90 % quantum efficiency is assumed [1.5] and [7.1]. For a Gaussian distribution, the statistical contribution to the energy resolution for the 800-keV beta of ^{238}U and ^{90}Sr will be

about 0.14 % FWHM (full width at half maximum). The above calculations are based on data obtained from gamma radiation spectrometry, and they could be inaccurate just because of the gamma-beta energy spectrum difference.

The electronic noise is a contribution of the detector PM tubes, low-noise amplifiers and low-level noise discriminators. The noise performance of the first stage of the signal amplification (the preamplifiers) however, is an important single parameter determining the energy resolution of a scintillator optically coupled to a photodiode [7.4].

The PM tubes of the detector prototype necessitate a biased high-voltage supply of 1,500 V to operate at high enough gains, and that this voltage be very well regulated for stable operation. Photodiodes do not demand high voltages because of their higher quantum efficiency.

Because of the lower values of the dark currents in the photodiodes, the signal-to-noise ratio is improved in a photodiode-equipped detector since noise associated with the leakage current (dark current) rises as the square root of this current [7.5].

The summation in quadrature of the three partial energy resolution fluctuations will give the total component. Because of the noise reduction of the component associated with the statistics and electronics, the total component of the diode's noise will be reduced and energy resolution improved.

7.2   HgI₂ photodiodes

The HgI_2 photodiodes that are proposed in this work exhibit a photosensitivity in the visible region of the spectrum, with peak sensitivity at around 570 nm and a long-wavelength cutoff at about 600 nm. The employed plastic scintillator has its light emission in the wavelength region of 300 to 600 nm, with the maximum at about 450 nm. The spectral response characteristics of HgI_2 are favorable for the detection of the scintillation light produced by the beta emission of ^{238}U and ^{90}Sr.

The advantages of using these photodiodes in place of PM tubes are:

i)   to increase energy resolution, sensitivity and detection efficiency

ii)   to decrease noise in the photoconverter part

iii)   to reduce detector volume and weight.

These diodes have been selected because of their low leakage current. They does not require cryogenic cooling nor does they require a bias voltage supply.

The removal of PM tubes and their replacement by HgI_2 photodiodes would result in the improvement of the electronic and statistical noises resulting in a better energy resolution. It would also end in a simpler design.

7.3 Quadruple-coincidence operation mode

Having the detector operating in a quadruple-coincidence operation mode was thought to result in an improvement of the beta detection sensitivity. However, it is next to be discussed that it is not necessarily true.

The sensitivity is defined as the number of counts above the discriminator level for each beta particle that reaches the detector. The crucial part in the study of the detector sensitivity lies in the electronics associated to it and the energy of the beta particles entering the last scintillation layer. The energy of the particles reaching the fourth layer would be very low and thus so would be the energy of the fluorescence photons generated in the scintillation material. Low-energy beta particles entering the surface of the fourth layer may undergo sufficient deflection so that they re-emerge from the surface through which they entered, resulting in backscattering.

During the laboratory investigations at OSURC, it was observed that the prototype under investigation presented some sensitivity to the gamma emissions of ^{16}N produced by the OSTRIGA reactor, (figure 6.10). A background of about 7 cps, which would be equivalent to 0.4 pCi/g of ^{238}U or 0.48 pCi/g of ^{90}Sr, was measured. The background signal has two components, the signal generated by the overall noise and the one owing to the cosmic radiation that causes triple-coincidence events. The larger contribution to the final background signal is due to the overall detector noise

and therefore a fourth layer will not reduce the noise component of the background but increase this component.

Additionally, it has been assumed that the beta particle incidence angles are 90°, which is not ever true because of the isotropical emissions of the source. The incidence angles for the 4-layer arrangement fall in the interval [50°, 130°], whereas for the 3-layer arrangement the interval is [40°,140°]. A larger number of particles in the 4-layer arrangement will not cause quadruple-multiple coincidences because of its geometrical configuration.

Considering all of the above, the small gain in the screening of the gamma radiation that could be obtained in a quadruple coincidence operation mode, could be offset by the decrease in beta radiation detection due to backscattering and to the loss of beta particles because of smaller incidence angles. From a theoretical point of view, any solution to the sensitivity problem has to be accompanied by a reduction of the equipment noise.

7.4 References

7.1   Markakis J. M., February 1988. "Mercuric Iodide Photodetector-Cesium Iodide Scintillator for Gamm-Ray Spectrometers." IEEE Trans. Nucl. Sci. Vol. NS-35, No. 1, 356-359.

7.2   Knoll G. F., 1989. "Radiation Detection and Measurement." p. 116-117. Jonh Wiley & Sons.

7.3   Goulding F. S. and Landis D. A., February 1988. "Ballistic Deficit Correction in Semiconductor Detector Spectrometers." IEEE Transactions on Nuclear Science, Vol. 35, No. 1, 119.

7.4   Goulding F. S., 1969. "Semiconductor Nuclear-Particle Detectors and Circuits." National Academy of Science. Publication 1593, p. 381.

7.5   Jones A. R., 1973. "A Comparison of Two Types of Amplifying Radiation Detector for Use in Portable Gamma Radiation Monitores." IEEE Transactions on Nuclear Science, NS 20(1), 528.

8. CONCLUSIONS

8.1 Detector laboratory investigation

The current prototype of the high-beta energy detector has behaved accurately and showed good linear response during the laboratory experiments. The main characteristics that have been observed are as follows:

1. The detector must be rebooted each time a fully charged battery is connected to it or after being without power supply.

2. The detector response is almost linear, especially for the high-energy beta radionuclides ^{238}U and ^{90}Sr. Good linear fits were obtained for every radionuclide. The fit corresponding to ^{154}Eu had the lowest coefficient of determination $(r^2 = 0.9571)$.

3. The set of counts performed for each sample followed a quasi-normal distribution with relatively distant minimum and maximum values. Fluctuations were noticed in the three first (sometimes even four) counts in all of the samples that were measured.

4. Errors obtained after the rejection of the three (or four) first detector readouts were significantly smaller than those including the whole set of readouts. An average of three detector readouts should be obtained to keep errors below 3.3%. Maximum errors of 10.3 % could be generated if only a detector readout is registered.

5. The average cps read out by the detector does not significantly change after and before the rejection of extreme values.

6. The 18-V battery discharges smoothly down to a value after which the battery discharges very fast.

7. The detector response is somewhat sensitive to gamma radiation fields. Increments in the background as much high as 20% were observed when OSTRIGA reactor was at full operation power (1 MW). High-energy photons of the reactor-produced ^{16}N were responsible for this surge.

8.2 Fernald Incinerator Site

One of the most relevant problems that had to be faced during the development of this project was the lack of confidence in the collected data. This was inevitable in a project like this where a new detector prototype was to be developed, and a little understanding of the detector was available. There was no means to guess what reality would be, and the most constructive approach was to be prepared to change when necessary.

The developing system that has the unique advantage of determining concentration levels of high-energy beta contaminants in a real time basis could characterize a site in a short period of time. As an example, Fernald Incinerator Site was characterized in one week. It could have been characterized in less time if not for the heavy rains that delayed the data collection.

The detector was very sensitive to weather conditions during data collection. Rain caused the soil to be wet, and the moisture in the ground then attenuated easily beta radiation. On the other hand, environmental high temperatures might have altered the detector performance, causing the detection of nonexistent surface contamination.

The detector only gives readings for any high-energy beta emitter in a sample while the discrimination between the species ^{238}U and ^{90}Sr is not possible. To achieve this goal, photodiodes are preferable.

Ordinary kriging allowed the determination of the geographical distribution of the radioactive contamination with a $\pm$ 10 % accompanying error. Such errors lead to the conclusion that the model used might not fit reality itself but approaches it fairly well. For instance, underestimations of the spread of contamination can lead to excessive exposure and increased risk to health, while overestimations may result in excessive costs and unnecessary restrictions on the use of valuable property. Nonetheless, this is certainly within reason provided the size of the site, the relatively small number of data collected and the fact that the contamination is not randomly distributed. But even with this powerful theoretical tool to analyze data, there can still be formidable physical problems simply in obtaining reliable data.

The variogram models used in the estimation had simple forms; however, they adjusted to the experimental variograms reasonably well. Future work in this area may involve more complex models that could better fit reality.

The kriging results are not definitive. They should not be considered as the best that can be produced from the kriging techniques. Kriging itself is in an evolutionary stage. Also, the work reported here made use of data that were collected under a narrow variety of conditions. In reality, much more information (data from ground moisture contents, soil grain size or detector behavior) ought to have been used to generate contour maps or make decisions on the contamination spread on the site.

For all the complexities, difficulties and surprises reality can produce, with thought and careful planning, judicious flexibility and work, ^{238}U and ^{90}Sr can be accurately detected.

8.3 Detector modifications

The current research on the modifications that could be introduced in the detector prototype to improve its behavior yielded the following results:

i)   it is feasible to replace the detector photomultipliers with photodiodes in order to obtain better energy resolution and better detector sensitivity.

ii)   it is highly unlikely that the operation of detector in a four-coincidence mode will result in a better detector sensitivity unless the current design is modified and PM tubes are replaced by photodiodes .

iii)   a reduction in weight and volume of the detector could be achieved by replacing PM tubes by photodiodes.

The detector beta sensitivity achievements are satisfactory because it would allowed site characterizations of soils containing surface contamination levels of about 0.4 pCi/g of ^{238}U. It was found that the average concentration of ^{238}U in U.S. soils is 1pCi/g [8.1]. In addition, radiation protection standards require a surface concentration of < 5 pCi/g of ^{226}Ra (^{226}Ra is a daughter of ^{238}U) within the top 15 cm of soil [8.2].

The remarkable disadvantage of the modified design is that commercial photodiodes are small (due to their high production costs) and so are their associated active areas. Such small active areas limit the size of the scintillator that can be optically coupled to the detector.

The trapping process within the diode (caused by unavoidable impurities) is a critical factor influencing the performance of these diode-equipped detectors. The presence of trapping results in a loss of collected charge and thereby in a degradation of the detector's energy resolution.

8.4 References

8.1   Myrick T. E., Berven B. A. and Heywood F. F., 1983. "Determination of Concentrations of Selected Radionuclides in Surface soil in the US." Health Phys. 45, 631-642.

8.2   Cochran R. G. and Tsoulfanidis N., 1990. "The Nuclear Fuel Cycle: Analysis and Management." P.41. American Nuclear Society. La Grande Park, Illinois.

BIBLIOGRAPHY

1.1   Schilk A.J., Perkins R. W., Abel K. H., and Brodzinski R. L., April 1993. "Surface and Subsurface Characterization of Uranium Contamination at the Fernald Environmental Management Site." PNL-8617/UC-606, Pacific Northwest Laboratory, Richland, Washington.

1.2   Siemon K., Esterlund R. A.,Van Aarle J., Knaack M., Westmeier W. and Patzelt P., 1992. "A New Measurement of the Gamma-Ray Intensities of ^{234m}Pa Accompanying the Decay of ^{238}U." Appl. Radiat. Isot. Vol. 43, No.7, 873-880.

1.3   Miller K. M. and Helfer I. K., 1985. "In Situ Measurements of ^{137}Cs Inventory in Natural Terrain." Environmental Measurements Laboratory, U. S. Department of Energy, 376 Hudson St., New York, NY 10014.

1.4   Knoll G. F., 1989. "Radiation Detection and Measurement." Chapter 11. John Wiley & Sons.

1.5   Sakai E., Febuary 1987. "Recent Measurements on Scintillator-Photodetector Systems." IEEE Transactions on Nuclear Science, Vol. NS-34, No. 1, 418.

1.6   Schilk A. J., Knopf M. A., Thompson R. C., Hubbard C. W., Abel K. H., Edwards D. R., Abraham J. R., 1993. "Real-Time, In Situ Detection of ^{90}Sr and ^{238}U in Soils Via Scintillating-Fiber-Sensor Technology." Unpublished. Pacific Northwest Laboratory, P. O. Box 999, Richland, Washington 99352.

1.7   Barnes M. G., 1978. "Statistical Design and Analysis in the Cleanup of Environmental Radionuclide Contamination", Desert Research Institute, University of Nevada System, NVO 1253-12.

1.8   David M., 1977. "Geostatistical Ore Reserve Estimation." Elsevier Publishing Company. New York.

1.9   Delhomme, J. P., 1978. "Kriging in the Hydrosciences", Advances in Water Resources 1, 251-266.

1.10   Piazza A., Menozzi P., and Cavalli-Sforza, L, 1981. "The Making and Testing of Geographic Gene-Frequency Maps", Biometrics 37, 635-659.

1.11   Eynon B. and Switzer, P., 1982. "The Variability of Rainfall Acidity", SIMS Technological Report No. 58. Department of Statistics, Stanford University, Stanford, CA.

1.12   Grivet C.D., 1980. "Modeling and Analysis of Air Quality Data", SIMS Technical Report No. 43, Department of Statistics, Stanford University, Stanford, CA.

1.13   Barnes M. G., 1980. "The Use of Kriging for Estimating the Spatial Distribution of Radionuclides and other Spatial Phenomena", TRAN-STAT: Statistics for Environmental Studies, No. 13. Pacific Northwest Laboratory, Richland, WA. PNL-SA-9051.

1.14   Gilbert R. O., 1985. "Kriging for Estimating Spatial Pattern of Contaminants: Potential and Problems", Environmental Monitoring and Assessment No. 5, 113-135.

1.15   Royle A., Clark I., Brooker P. W., Parker H., Journel A., Rendu J. M., Sandefur R., Grant D. C., and Mousset-Jones P., 1980. "Geostatistics" Chapter 1. McGraw-Hill, Inc. New York, N. Y.

2.1   Gillespie A. B., 1953. "Signal, Noise and Resolution in Nuclear Counter Amplifiers." Pergamon Press, London.

2.2   Knoll G. F., 1989. "Radiation Detection and Measurement." John Wiley & Sons. Chapter 9, p. 268.

3.1.   Journel A. G. and Huijbregts, C. J., 1978. "Mining Geostatistics." p. 29. Academic Press. New York, N. Y.

3.2.   Journel A.G., 1983. "No Parametric Estimation of Spatial Distributions." Mathematical Geology Vol. 15, No. 3, 445-468.

3.3.   Englud E, April 1991. "Geostatistical Environmental Assessment Software User's Guide." Section 4, 4-5.

4.1   Isaak E. H. and Srivastava R. M., 1989. "An Introduction to Applied Geostatistics." Chapter 13, 330. Oxford University Press, Oxford, NY.

4.2   Delfiner P. and Delhomme J. P., 1975. "Optimum Interpolation by Kriging." Display and Analysis of Spatial Data Nato Advanced Study Institute. John C. Davis and Michael J. McCullagh, ed., John Wiley and Sons, New York.

4.3   Barnes M. G., 1978. "Statistical Design and Analysis in the Cleanup of Environmental Radionuclide Contamination", Desert Research Institute, University of Nevada System, NVO 1253-12. p. 15.

4.4   Englud, E, April 1991. "Geostatistical Environmental Assessment Software User's Guide." Section 10, 10-5.

7.1   Markakis J. M., February 1988. "Mercuric Iodide Photodetector-Cesium Iodide Scintillator for Gamm-Ray Spectrometers." IEEE Trans. Nucl. Sci. Vol. NS-35, No. 1, 356-359.

7.2   Knoll G. F., 1989. "Radiation Detection and Measurement." p. 116-117. Jonh Wiley & Sons.

7.3   Goulding F. S. and Landis D. A., February 1988. "Ballistic Deficit Correction in Semiconductor Detector Spectrometers." IEEE Transactions on Nuclear Science, Vol. 35, No. 1, 119.

7.4   Goulding F. S., 1969. "Semiconductor Nuclear-Particle Detectors and Circuits." National Academy of Science. Publication 1593, p. 381.

7.5   Jones A. R., 1973. "A Comparison of Two Types of Amplifying Radiation Detector for Use in Portable Gamma Radiation Monitores." IEEE Transactions on Nuclear Science, NS 20(1), 528.

8.1   Myrick T. E., Berven B. A. and Heywood F. F., 1983. "Determination of Concentrations of Selected Radionuclides in Surface soil in the US." Health Phys. 45, 631-642.

8.2   Cochran R. G. and Tsoulfanidis N., 1990. "The Nuclear Fuel Cycle: Analysis and Management." P.41. American Nuclear Society. La Grande Park, Illinois.

APPENDICES

APPENDIX 1

Fernald Incinerator Site collected data.

The 86-site data collected with the detector prototype are listed below. The first and second columns are the easting (feet) and northing (feet), respectively. The third column is the measured activity in pCi/g. The last column represents the flag.

68	308	53.98	'CC6'
98	307	43.85	'CC6.5'
8	309	31.27	'CC5'
7	249	39.05	'AA5'
67	248	46.15	'AA6'
66	218	46.88	'Z6'
77	238	54.34	'F1'
81	237	52.46	'F2'
86	237	49.33	'F3'
86	232	54.4	'E3'
81	232	42.13	'E2'
76	233	44.84	'E1'
76	228	57.73	'D1'
81	227	50.79	'D2'
86	227	49.44	'D3'
97	247	50.79	'AA6.5'
96	217	57.79	'Z6.5'
95	187	55.60	'Y6.5'
65	188	52.78	'Y6'
5	189	46.02	'Y5'
4	129	52.73	'W5'
2	74	48.34	'U5'
63	103	55.18	'V6'
93	112	69.64	'V6.5'
94	127	60.76	'W6.5'
64	128	50.01	'W6'
123	126	68.12	'W7'
154	129	62.90	'W7.5'
184	138	55.07	'W8'
128	306	52.67	'CC7'
188	305	53.46	'CC8'
187	245	46.25	'AA8'
127	246	48.24	'AA7'
126	216	47.87	'Z7'
125	186	51.58	'Y7'
124	156	57.16	'X7'
62	63	57.72	'U6'
0	9	38.69	'S5'
92	67	70.29	'U6.5'
122	70	70.22	'U7'
182	75	80.79	'U8'
242	63	77.60	'U9'
221	4	91.30	'S9'
213	109	70.85	'W8.5'
243	121	64.46	'W9'
243	93	70.72	'V9'
273	92	60.06	'V9.5'
273	122	51.36	'W9.5'
154	155	46.43	'X7.5'
184	155	57.30	'X8'
185	185	42.62	'Y8'
155	185	56.22	'Y7.5'
215	184	55.59	'Y8.5'
245	183	47.46	'Y9'
259	183	56.39	'Y9.5'

86-site collected data (continued)

245	166	61.17	'X9'
214	154	52.75	'X8.5'
248	303	67.42	'CC9'
308	302	50.31	'CC10'
294	242	69.70	'AA10'
277	242	61.59	'AA9.5'
247	243	48.93	'AA9'
246	213	53.07	'Z9'
276	212	70.24	'Z9.5'
321	211	57.09	'Z10'
305	182	65.32	'Y10'
303	122	64.66	'W10'
363	120	69.52	'W11'
365	180	65.08	'Y11'
367	240	35.54	'AA11'
362	0	44.67	'S11'
362	60	69.64	'U11'
302	62	68.26	'U10'
303	92	54.52	'V10'
292	82	54.46	'C3'
287	82	48.88	'C2'
282	82	61.59	'C1'
282	77	54.97	'B1'
287	77	57.48	'B2'
292	77	56.07	'B3'
272	62	52.25	'U9.5'
282	72	49.96	'A1'
287	72	51.78	'A2'
292	72	78.52	'A3'
300	2	70.80	'S10'
368	300	38.88	'CC11'

The 85-site data collected by the Fernald site personnel are listed below. This set of data were obtained by hand collection, followed by laboratory spectroscopy. The first and second columns are the easting (feet) and northing (feet), respectively. The third column is the measured activity in pCi/g. The last column represents the flag.

68	308	59.33	'CC6'
8	309	50.12	'CC5'
7	249	39.41	'AA5'
67	248	59.80	'AA6'
66	218	45.36	'Z6'
77	238	50.93	'F1'
81	237	49.90	'F2'
86	237	52.56	'F3'
86	232	56.38	'E3'
81	232	52.44	'E2'
76	233	56.83	'E1'
76	228	64.89	'D1'
81	227	53.81	'D2'
86	227	55.36	'D3'
97	247	52.99	'AA6.5'
96	217	56.85	'Z6.5'
95	187	60.17	'Y6.5'
65	188	55,32	'Y6'
5	189	49.60	'Y5'
4	129	61.86	'W5'
2	74	47.53	'U5'
63	103	58.81	'V6'
93	112	85.46	'V6.5'
94	127	74.04	'W6.5'
64	128	70.52	'W6'
123	126	79.11	'W7'
154	129	77.83	'W7.5'
184	138	62.32	'W8'
128	306	52.48	'CC7'
188	305	51.36	'CC8'
187	245	61.79	'AA8'
127	246	48.42	'AA7'
126	216	49.57	'Z7'
125	186	57.33	'Y7'
124	156	68.76	'X7'
62	63	75.60	'U6'
0	9	50.98	'S5'
92	67	82.55	'U6.5'
122	70	89.03	'U7'
182	75	105.58	'U8'
242	63	76.02	'U9'
221	4	90.68	'S9'
213	109	81.23	'W8.5'
243	121	52.94	'W9'
243	93	81.67	'V9'
273	92	54.12	'V9.5'
273	122	51.20	'W9.5'
154	155	62.73	'X7.5'
184	155	61.53	'X8'
185	185	59.93	'Y8'
155	185	76.00	'Y7.5'
215	184	68.69	'Y8.5'
245	183	62.19	'Y9'
259	183	60.78	'Y9.5'
245	166	78.12	'X9'

85-site collected data (continued)

214	154	61.53	'X8.5'
248	303	61.59	'CC9'
308	302	60.74	'CC10'
294	242	53.89	'AA10'
277	242	68.27	'AA9.5'
247	243	54.20	'AA9'
246	213	57.49	'Z9'
276	212	67.36	'Z9.5'
321	211	58.82	'Z10'
305	182	57.80	'Y10'
303	122	75.26	'W10'
363	120	82.98	'W11'
365	180	86.77	'Y11'
367	240	51.54	'AA11'
362	0	39.21	'S11'
362	60	58.04	'U11'
302	62	59.77	'U10'
303	92	53.72	'V10'
292	82	61.10	'C3'
287	82	61.84	'C2'
282	82	72.21	'C1'
282	77	46.80	'B1'
287	77	71.08	'B2'
292	77	64.39	'B3'
272	62	52.16	'U9.5'
282	72	63.36	'A1'
287	72	56.58	'A2'
292	72	65.60	'A3'
300	2	71.75	'S10'
368	300	31.41	'CC11'

APPENDIX 2

Normal distribution plots of the detector statistical performance at OSURC laboratory environment.

Next 16 pages of this appendix show the normal probability plots for the data collected during the laboratory investigations at OSURC. Pages 103 throughout 105 show the probability plots for the measurements regarding ^{238}U-sand activities of 5 pCi/g (page 103) , 15 pCi/g (page 104) and 35 pCi/g (page 105), respectively. Pages 106 throughout 109 refer to ^{238}U-filter paper activities of 3.86 (page 106), 40.5 (page 107), 40.5 (page 108 shows the same as page 107 but two more points corresponding to the two observed outliers that were discarded in the plot of p. 107) and 373 pCi/g (page 109), respectively. Pages 110 throughout 112 show the probability plots for ^{90}Sr filter paper activities of 3.78 (page 110), 9.89 (page 111) and 37.5 (page 112) pCi/g, respectively. Pages 113 through 116 display the plots for ^{154}Eu filter paper activities of 150 (page 113), 376.5 (page 114), 376.5 (page 115 shows the same as page 114 but one less point corresponding to the discarded outlier) and 625 (page 116) pCi/g, respectively. Finally, pages 117 and 118 correspond to the ^{137}Cs filter paper activities of 102.5 (page 117) and 203.13 pCi/g (page 118).

Normal Probability Plot for Activity
Data file: s5.dat

Statistics

N Total	:	7
N Miss	:	0
N Used	:	7
Mean	:	11.989
Variance	:	.030
Std. Dev	:	.173
% C.V.	:	1.439
Skewness	:	-.074
Kurtosis	:	1.921
Minimum	:	11.750
25th %	:	11.788
Median	:	12.000
75th %	:	12.080
Maximum	:	12.240
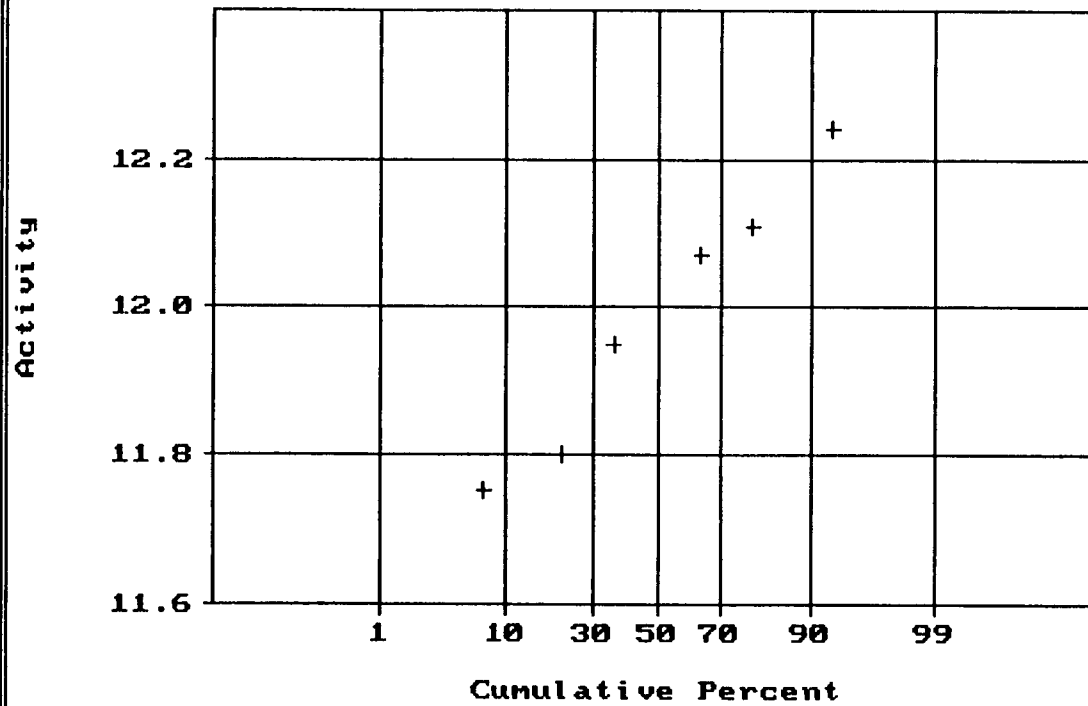
Normal Probability Plot for Activity
Data file: s15.dat

Statistics
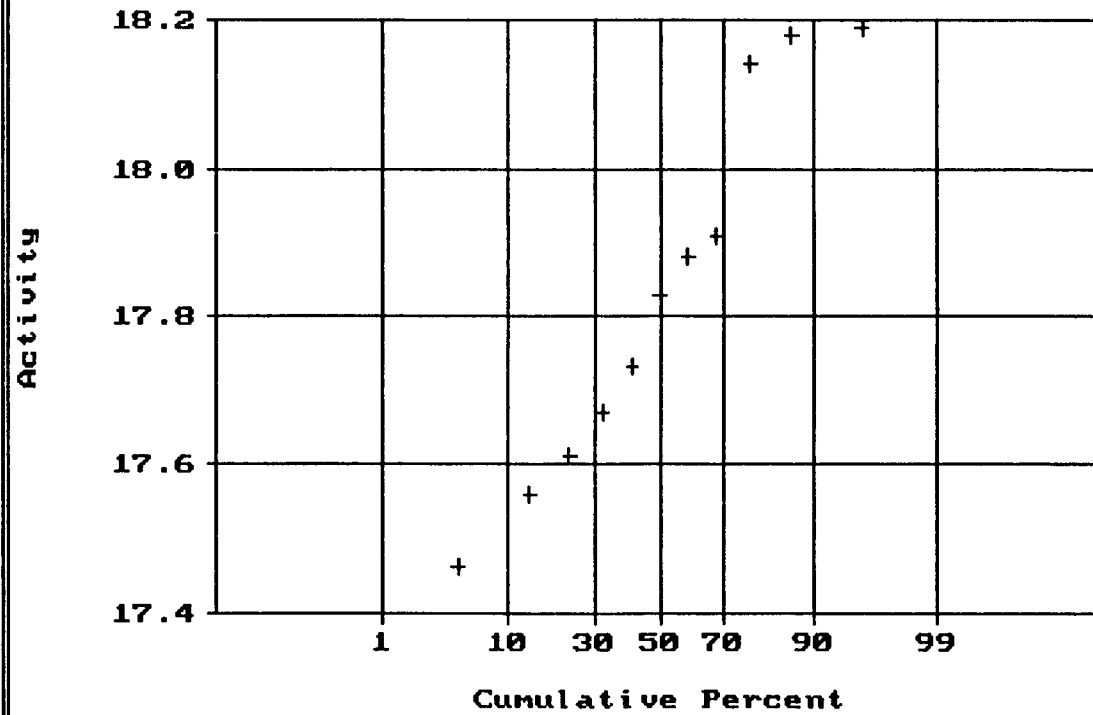
N Total	:	11
N Miss	:	0
N Used	:	11
Mean	:	17.833
Variance	:	.065
Std. Dev	:	.255
% C.V.	:	1.431
Skewness	:	.180
Kurtosis	:	1.763
Minimum	:	17.460
25th %	:	17.597
Median	:	17.830
75th %	:	17.967
Maximum	:	18.190

Normal Probability Plot for Activity
Data file: s35.dat

S t a t i s t i c s

N Total :	13
N Miss :	0
N Used :	13
Mean :	23.834
Variance:	.340
Std. Dev:	.583
% C.V. :	2.447
Skewness:	.591
Kurtosis:	2.212
Minimum :	23.090
25th % :	23.290
Median :	23.720
75th % :	24.245
Maximum :	24.980
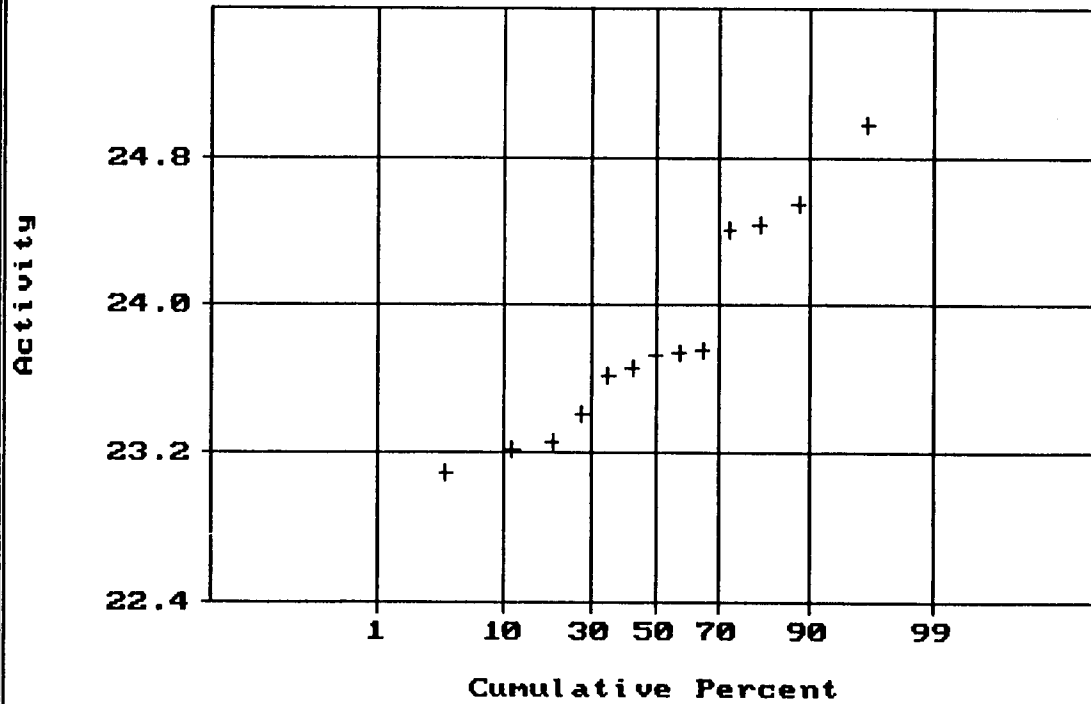
Normal Probability Plot for Activity
Data file: u4.dat

Statistics
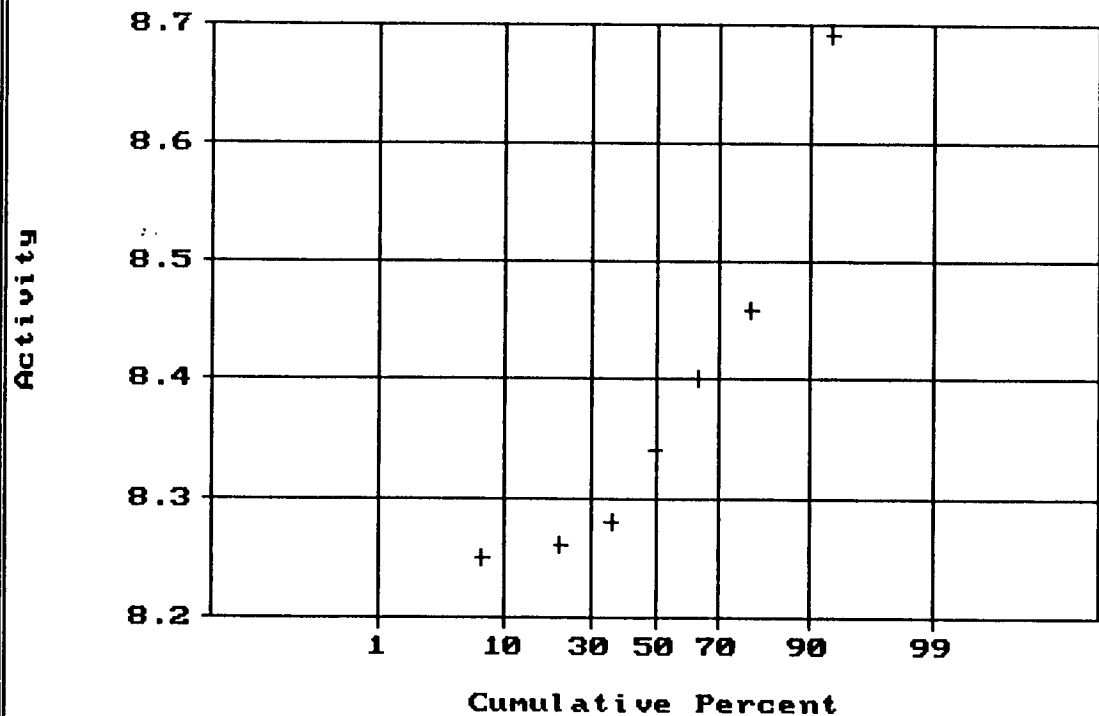
N Total :	7
N Miss :	0
N Used :	7
Mean :	8.383
Variance:	.024
Std. Dev:	.156
% C.V. :	1.859
Skewness:	1.145
Kurtosis:	3.160
Minimum :	8.250
25th % :	8.257
Median :	8.340
75th % :	8.415
Maximum :	8.690

Normal Probability Plot for Activity
Data file: u40.1dat

Statistics
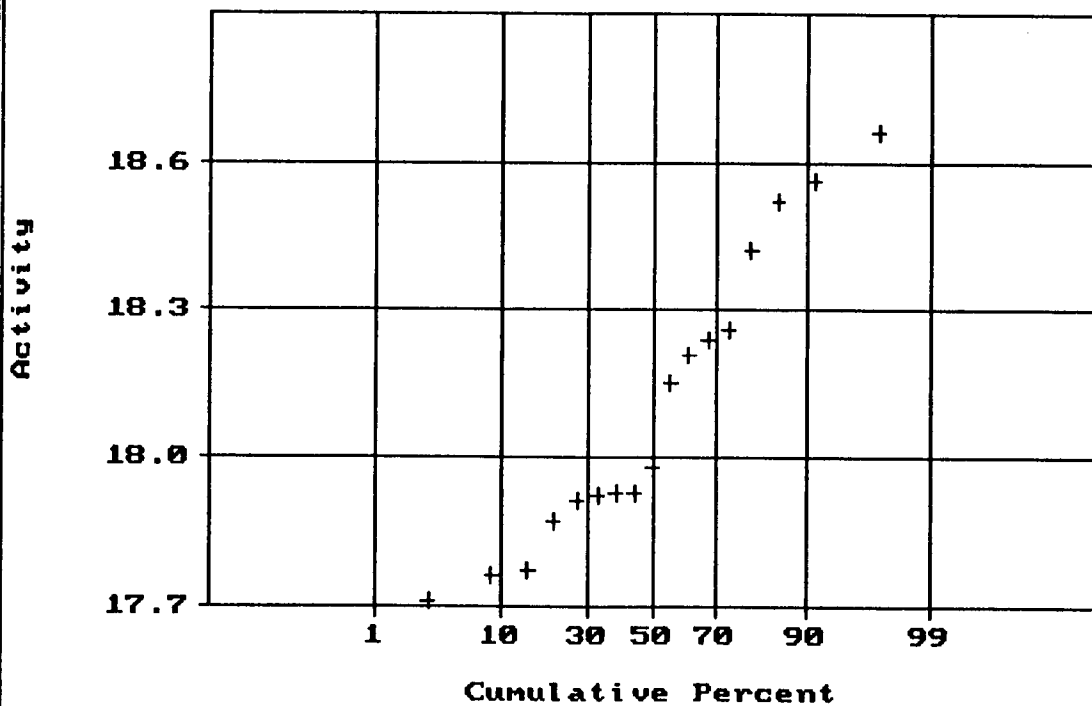
N Total	:	17
N Miss	:	0
N Used	:	17
Mean	:	18.106
Variance	:	.090
Std. Dev	:	.299
% C.V.	:	1.653
Skewness	:	.461
Kurtosis	:	1.957
Minimum	:	17.710
25th %	:	17.880
Median	:	17.980
75th %	:	18.255
Maximum	:	18.660

Normal Probability Plot for Activity
Data file: u40.dat

Statistics
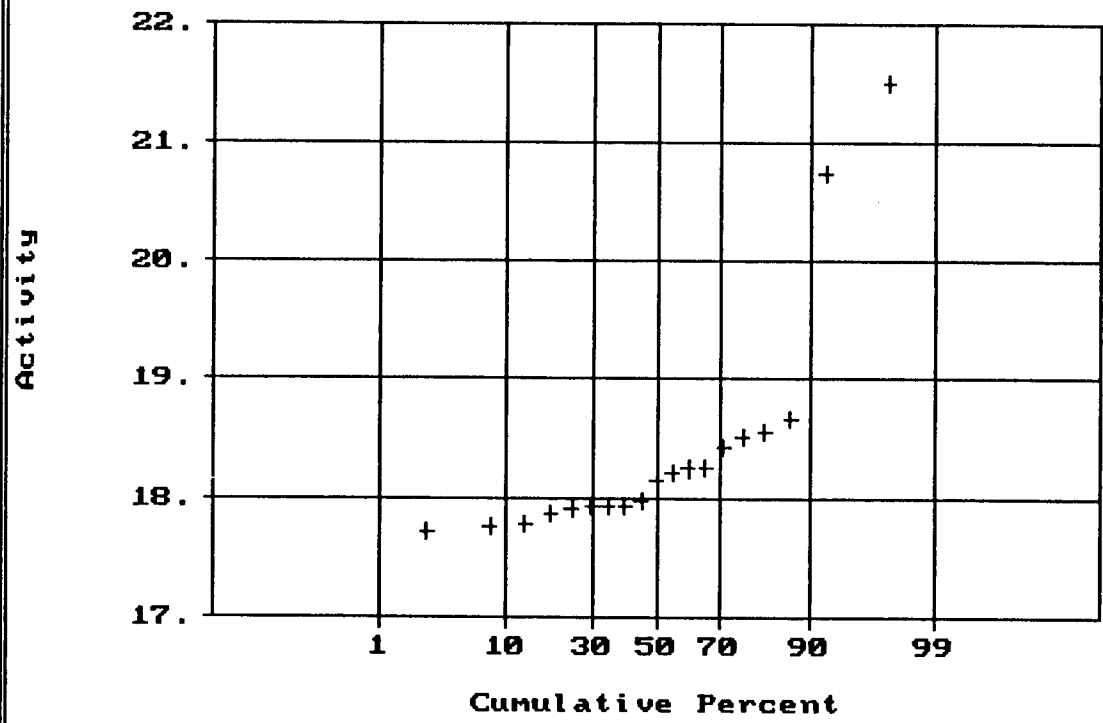
N Total	:	19
N Miss	:	0
N Used	:	19
Mean	:	18.424
Variance	:	1.001
Std. Dev	:	1.001
% C.V.	:	5.432
Skewness	:	2.277
Kurtosis	:	7.010
Minimum	:	17.710
25th %	:	17.900
Median	:	18.150
75th %	:	18.445
Maximum	:	21.500

Normal Probability Plot for Activity
Data file: u400.dat

S t a t i s t i c s
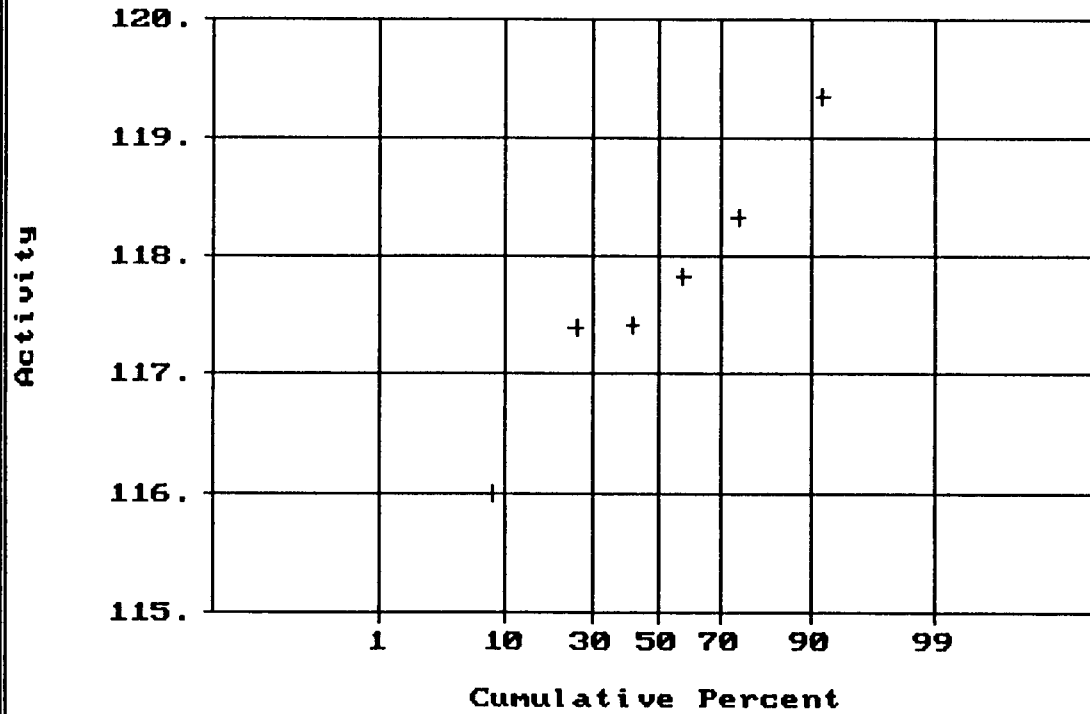
N Total	:	6
N Miss	:	0
N Used	:	6
Mean	:	117.720
Variance	:	1.232
Std. Dev	:	1.110
% C.V.	:	.943
Skewness	:	-.107
Kurtosis	:	2.498
Minimum	:	116.000
25th %	:	116.695
Median	:	117.630
75th %	:	118.080
Maximum	:	119.340

Normal Probability Plot for Activity
Data file: sr4.dat

S t a t i s t i c s
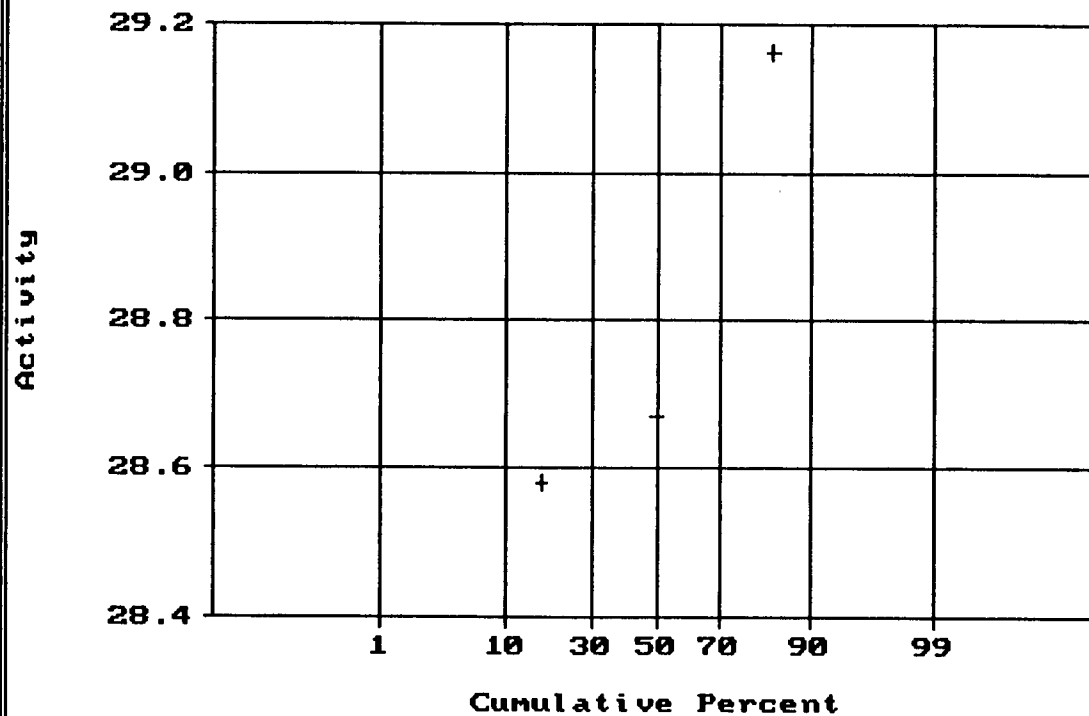
N Total	:	3
N Miss	:	0
N Used	:	3
Mean	:	28.803
Variance	:	.097
Std. Dev	:	.312
% C.V.	:	1.084
Skewness	:	.642
Kurtosis	:	1.500
Minimum	:	28.580
25th %	:	.000
Median	:	28.670
75th %	:	28.792
Maximum	:	29.160

Activity axis values: 29.2, 29.0, 28.8, 28.6, 28.4

Cumulative Percent axis values: 1, 10, 30, 50, 70, 90, 99

Cumulative Percent

Normal Probability Plot for Activity
Data file: sr10.dat

Statistics

N Total	:	6
N Miss	:	0
N Used	:	6
Mean	:	80.380
Variance	:	.405
Std. Dev	:	.636
% C.V.	:	.792
Skewness	:	.543
Kurtosis	:	1.603
Minimum	:	79.780
25th %	:	79.815
Median	:	80.160
75th %	:	80.655
Maximum	:	81.290
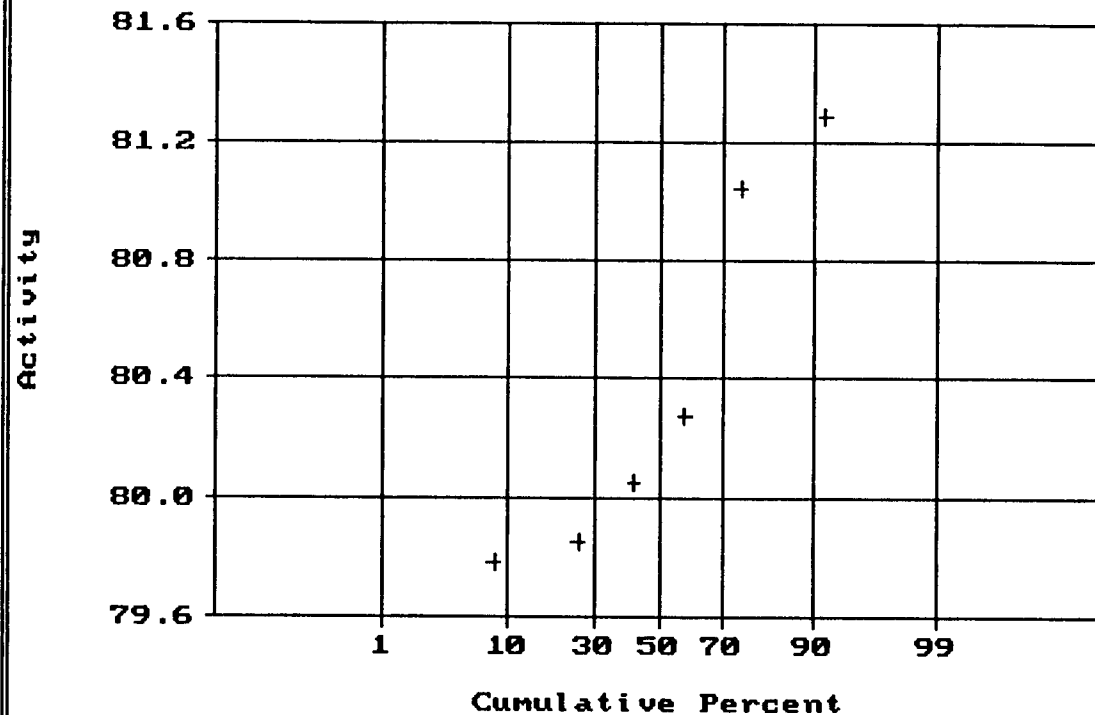
Normal Probability Plot for Activity
Data file: sr40.dat

Statistics
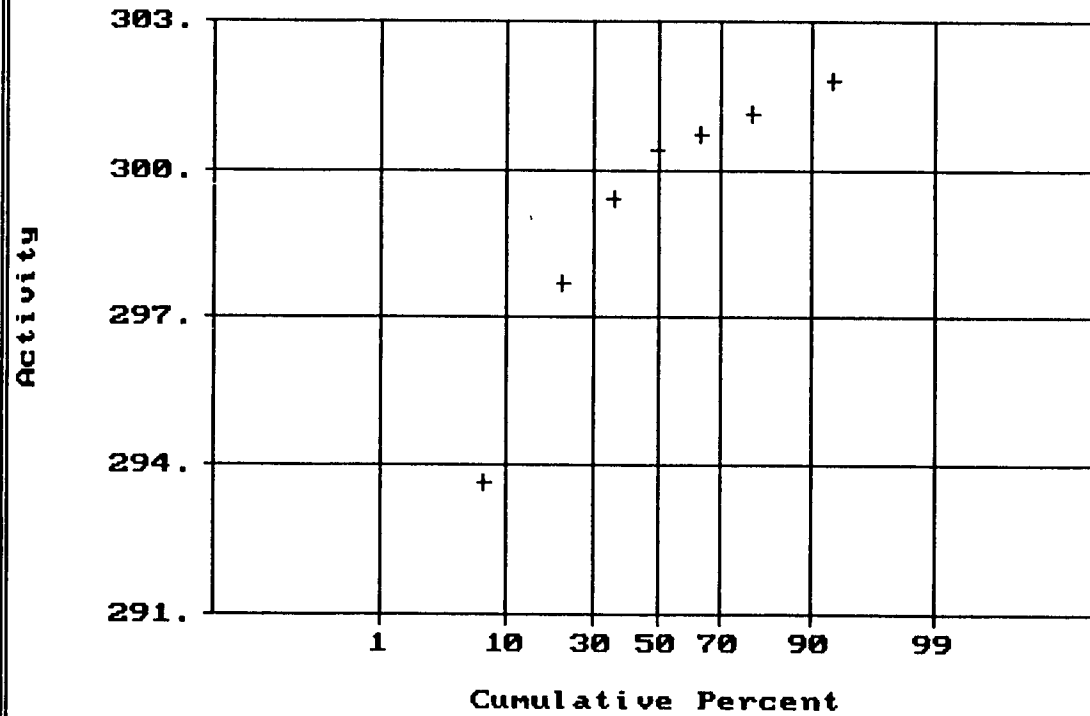
N Total	:	7
N Miss	:	0
N Used	:	7
Mean	:	299.249
Variance	:	7.885
Std. Dev	:	2.808
% C.V.	:	.938
Skewness	:	-1.232
Kurtosis	:	3.284
Minimum	:	293.650
25th %	:	296.665
Median	:	300.370
75th %	:	300.818
Maximum	:	301.810

Y-axis (Activity): 303., 300., 297., 294., 291.

X-axis (Cumulative Percent): 1, 10, 30, 50, 70, 90, 99

Normal Probability Plot for Activity
Data file: eu150.dat

S t a t i s t i c s
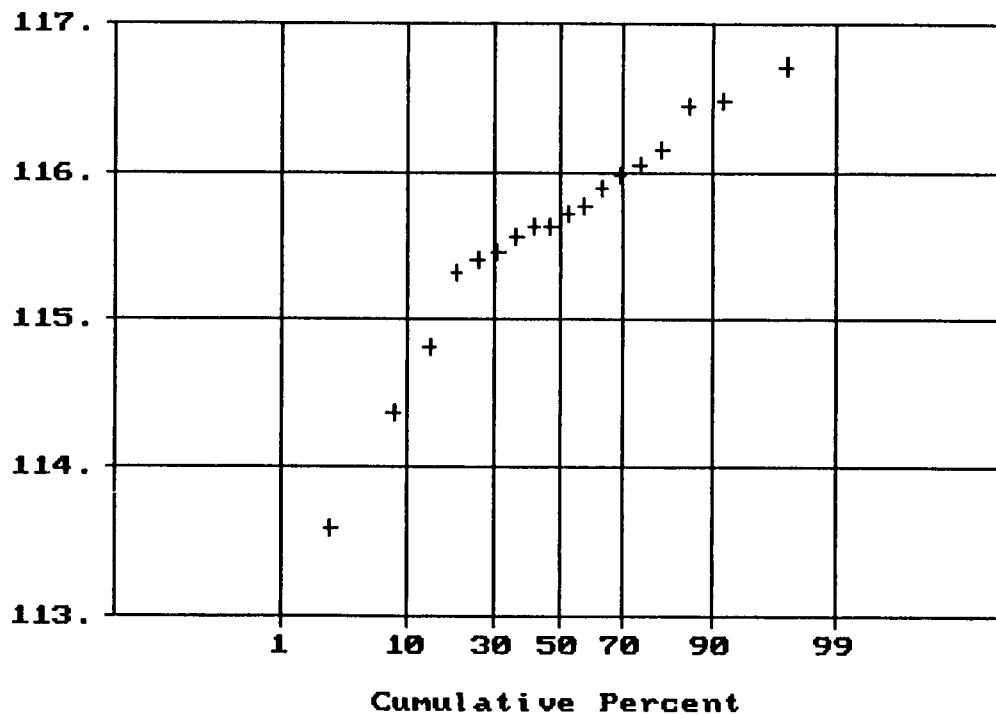
N Total	:	18
N Miss	:	0
N Used	:	18
Mean	:	115.608
Variance	:	.578
Std. Dev	:	.760
% C.V.	:	.657
Skewness	:	-1.076
Kurtosis	:	4.124
Minimum	:	113.590
25th %	:	115.360
Median	:	115.675
75th %	:	116.015
Maximum	:	116.710

Normal Probability Plot for Activity
Data file: eu400.dat

Statistics
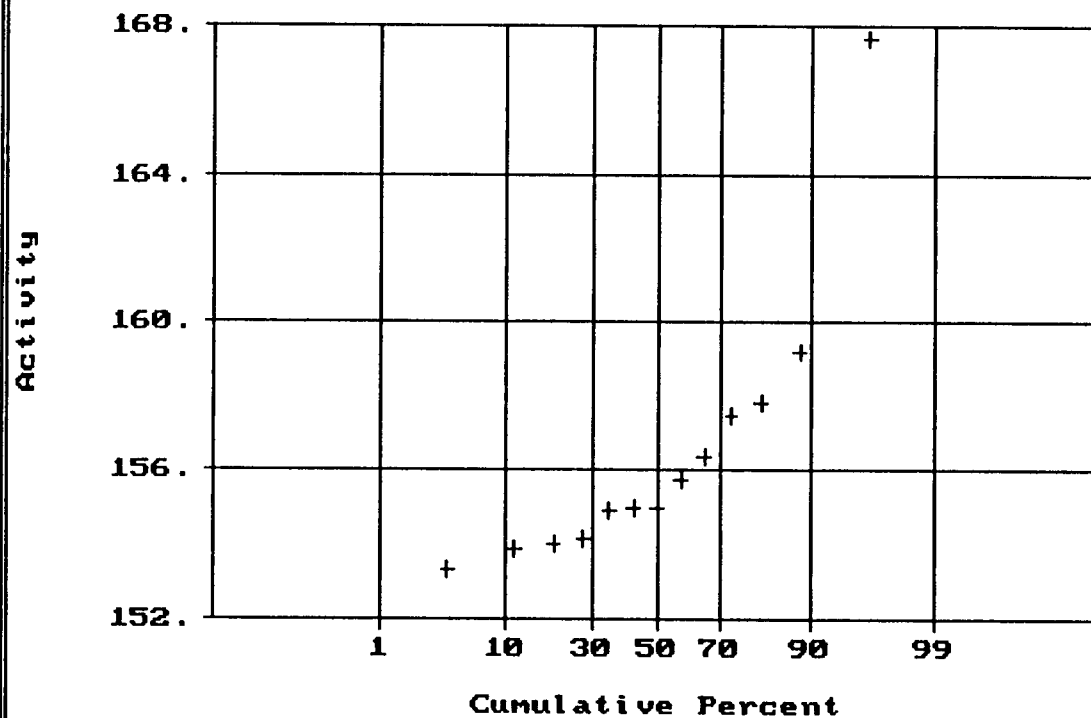
N Total	:	13
N Miss	:	0
N Used	:	13
Mean	:	156.481
Variance	:	14.247
Std. Dev	:	3.774
% C.V.	:	2.412
Skewness	:	2.121
Kurtosis	:	6.981
Minimum	:	153.300
25th %	:	154.003
Median	:	154.970
75th %	:	157.205
Maximum	:	167.620

Normal Probability Plot for Activity
Data file: eu400.1dat
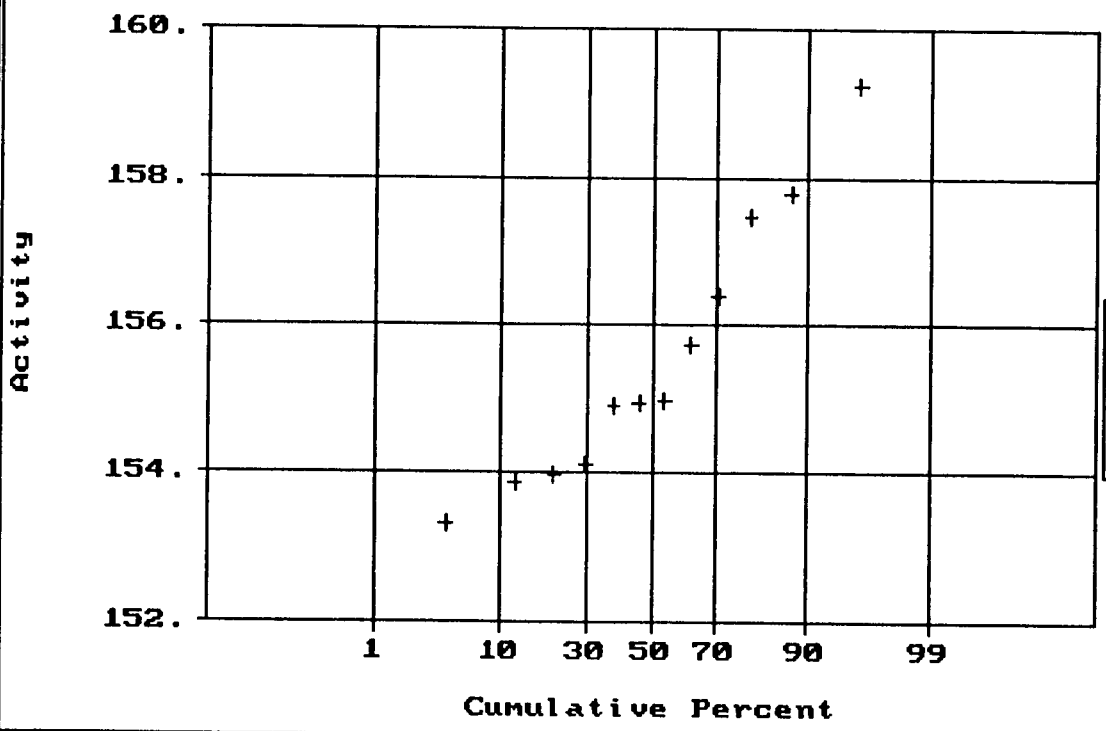
Statistics

N Total	:	12
N Miss	:	0
N Used	:	12
Mean	:	155.553
Variance	:	3.321
Std. Dev	:	1.822
% C.V.	:	1.172
Skewness	:	.696
Kurtosis	:	2.382
Minimum	:	153.300
25th %	:	153.970
Median	:	154.950
75th %	:	156.380
Maximum	:	159.220

Normal Probability Plot for Activity
Data file: eu600.dat

S t a t i s t i c s
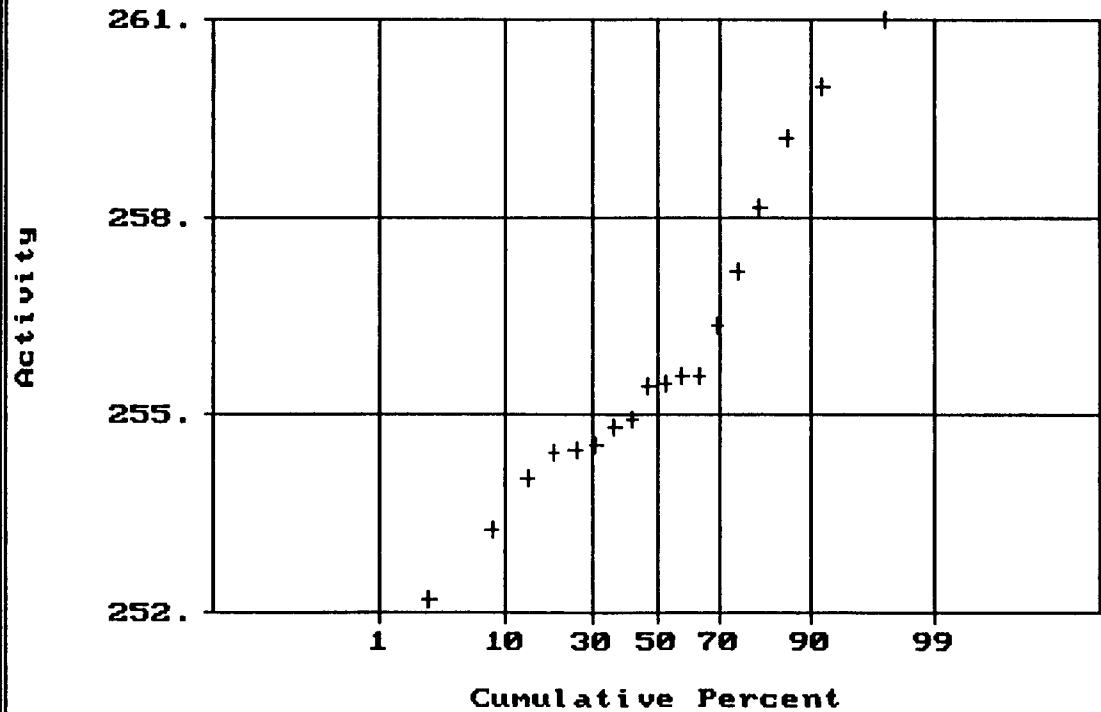
N Total	:	18
N Miss	:	0
N Used	:	18
Mean	:	255.909
Variance:		5.541
Std. Dev:		2.354
% C.V.	:	.920
Skewness:		.735
Kurtosis:		2.774
Minimum	:	252.180
25th %	:	254.420
Median	:	255.440
75th %	:	256.765
Maximum	:	261.000

Normal Probability Plot for Activity
Data file: cs100.dat

Statistics
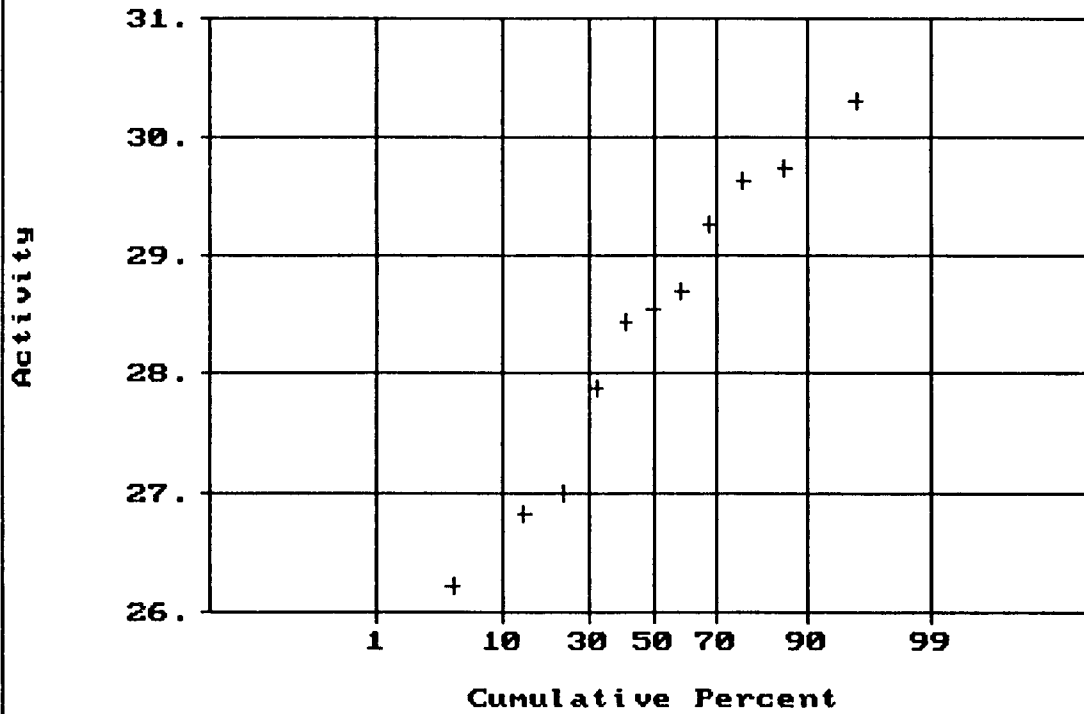
N Total :		11
N Miss :		0
N Used :		11
Mean :		28.417
Variance:		1.736
Std. Dev:		1.318
% C.V. :		4.637
Skewness:		-.278
Kurtosis:		1.923
Minimum :		26.220
25th % :		26.955
Median :		28.550
75th % :		29.362
Maximum :		30.310

Normal Probability Plot for Activity
Data file: cs200.dat

S t a t i s t i c s
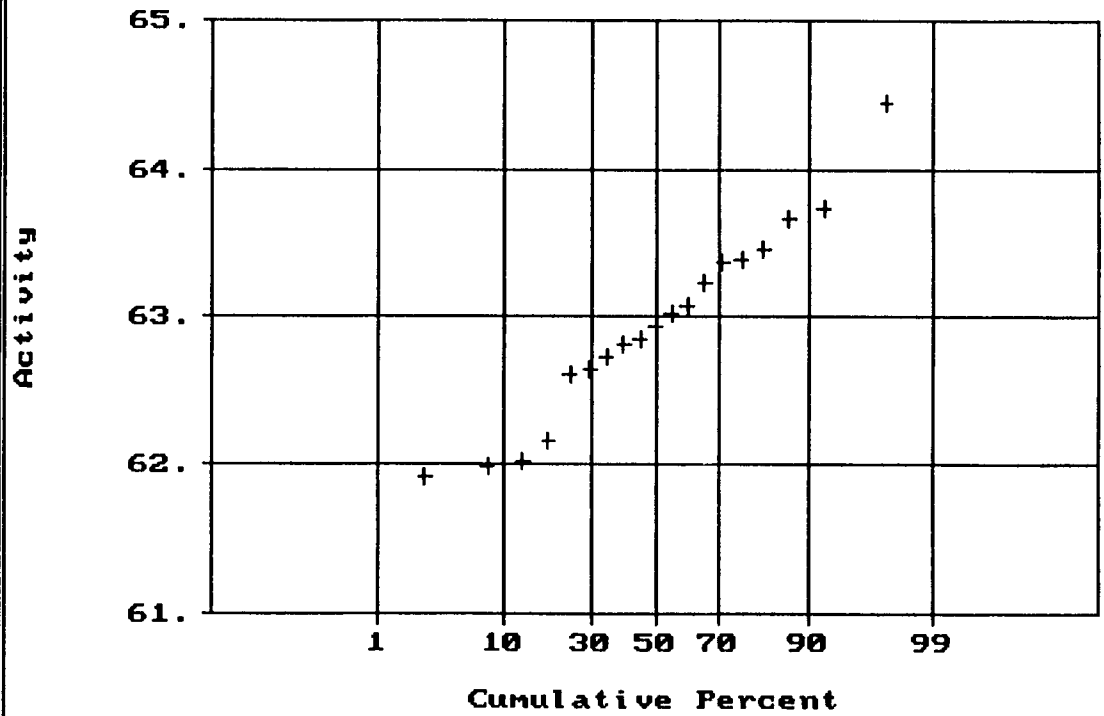
N Total :	19
N Miss :	0
N Used :	19
Mean :	62.949
Variance:	.438
Std. Dev:	.662
% C.V. :	1.051
Skewness:	.230
Kurtosis:	2.753
Minimum :	61.920
25th % :	62.487
Median :	62.940
75th % :	63.372
Maximum :	64.450

APPENDIX 3

Detector laboratory investigation collected data

4/6/95

Number	cps (Total)	Voltage	Time	Comments
Counting Background				
1	7.92 (2376)	18.08		
2	7.21 (2162)	18.08	11:27 a.m.	
3	7.47 (2241)	18.04		
4	7.73 (2219)			
5	3.36 (1008)	18.01	11:43 a.m.	
6	3.33 (1000)	17.99	11:49	
7	3.14 (941)			
8	3.3 (991)	17.96	12:00	
9	3.22 (966)			
10	3.24 (971)			
11	4.04 (1212)	17.92	12:15 p.m.	
12	7.14 (2143)			
13	7.00 (2100)			
14	6.79 (2037)	17.88	12:35	
15	5.76 (1727)			
16	3.19 (956)	17.70	13:37	
17	3.31 (994)	17.66	13:50	
18	3.59 (1078)			
#1 Module Operation (No #2)		TRIGA IN OPERATION AT 1 MW FROM 11:00 TO 14:00		
1	0			
#2 Module Operation (No #1)				
	3.46 (1037)			
Both Modules				
1	7.75 (2324)			
2	7.59 (2276)			
3	4.83 (1448)	17.55	14:40	

Number	cps (Total)	Voltage	Time	Comments
4	3.22 (967)			
5	3.46 (1039)	17.51	14:50	
6	3.59 (1078)			
7	3.64 (1091)			
10	7.75 (2326)		15:15 (5M)	After disconnecting det. from source & reconnected)
11	8.23 (2470)			
12	6.96 (2087)	17.31	15:30	
13	6.67 (2002)			
14	6.99 (2096)			
15	6.97 (2092)			
16	7.06 (2117)	17.29	15:50	
17	7.03 (2108)			
18	6.94 (2082)	17.25	16:00	
19	7.28 (2185)			
20	7.21 (2164)			
21	7.00 (2100)			
22	7.09 (2126)	17.14	16:25	
23	7.26 (2179)			
24	7.10 (2129)			
25	6.85 (2056)	17.06	16:40	
26	7.08 (2123)			

4/7/95

Number	cps (Total)	Voltage	Time	Comments
1	6.64 (1991)	17.20		
		17.14	8:05 a.m.	One minute after.
		17.09	8:09 a.m.	
2	5.86 (1757)	17.06	8:20	
3	5.33 (1600)			
4	4.81 (1444)	16.97	8:30 a.m.	
5	3.14 (943)			Disconnect from source one minute.
6	3.58 (1075)			Source on/off for about one minute.
7	3.30 (989)	16.82	8:50	
8	3.28 (980)			
1	5.51 (1653)			About 30 m later after probing with oscilloscope.
2	3.26 (977)	15.72	9:30	
3	3.36 (1007)			
1	5.79 (1736)	15.38	9:50	5 min disruption.
2	3.45 (1034)			
3	3.41 (1023)			
1	3.49 (1047)			Very short source disruption
1	7.79 (2336)	HV sources	·.	Remove cover and 5 m off.
2	7.65 (2294)		11:35	Voltage 11V.
1	9.94 (2981)	17.83	11:35	New battery. Data logger: A. Schilk
2	8.01 (2403)			
3	8.39 (2518)			
4	8.04 (2411)			
5	7.57 (2270)			
6	7.85		11:18	Date logger: JFH

Number	cps (Total)	Voltage	Time	Comments
7	8.22			
8	7.57			
9	7.77		11:43	
10	7.85	17.43	11:47	
Add 35 pCi/g U sand (15 min mix in drum). Sand uniformly distributed in tray, depth-- 1.5 cm				
1	25.75		11:50	Cover off detector. Data logger: JFH
2	25.21			
3	26.24			
4	25.72	17.24	12:17	
5	25.43			
6	25.27	17.06	12:33	
7	27.41			
8	25.26		12:39	
9	25.33 (7599)			
10	25.76(2092)	16.00	12:51	Data logger: AS
11	25.17	14.85	12:58	
12	25.60	14.26	1:04	
		avg 25.68		
1	7.88	17.61	1:17	Bench bkgd. New battery.
2	7.75	17.56	1:23	Data logger: AS
3	7.33	17.51	1:29	Add empty tray. Data logger: JFH
4	7.46	17.46	1:34	Data logger: AS
5	7.42	17.40	1:40	
6	7.56	17.33	1:48	
7	7.66	17.25	1:55	
8	8.47	17.17	2:01	Remove tray.

Number	cps (Total)	Voltage	Time	Comments
9	9.82	17.08	2:07	
Add 5 pCi/g U sand, as before.				
1	12.97	14.91	2:30	Data logger: AS
2	13.13	14.37	2:36	New battery at 2:40
3	13.23	17.51	2:45	Data logger: FMB
4	12.65	17.48	2:50	
5	13.27	17.44	2:55	
6	13.26	17.40	3:05	
7	13.53	17.37	3:10	
8	13.17	17.35	3:15	
		avg 13.15		
Background with no tray.				
1	10.83	17.29	3:25	Sand on the window.
Add 15 pCi/g U sand, as before.				
1	17.63	17.25	3:30	Data logger: FMB
2	17.45	17.23	3:35	
3	17.45	17.19	3:40	
4	17.59	17.16	3:45	
5	17.33	17.12	3:50	
6	17.49	17.08	3:55	
7	17.50	17.05	4:00	
8	16.18	17.00		
		avg 17.33		
1	7.27	16.93	4:15	Background. Sand on the window.
Filter paper with an activity of 3.83 pCi/cm^2 of ^{238}U				
1	8.46	16.84	4:25	Data logger: FMB
2	8.69	16.78	4:30	
3	8.28	16.71	4:35	

Number	cps (Total)	Voltage	Time	Comments
4	8.26	16.61	4:40	
5	8.34	16.31	4:48	
6	8.40	15.80	4:55	
7	8.25	14.78		

4/10/95

Number	cps (Total)	Voltage	Time	Comments
Start counts (background) at 8:00 a.m.				
1	7.17	15.73	8:00	Cover on.
2	7.47	14.84	8:05	No problem with first.
3	7.47	14.10	8:10	
4	7.22	13.78	8:15	
5	7.43	13.27	8:20	
6	7.67	13.14	8:25	
7	7.57	13.00	8:30	
8	7.74	12.89	8:35	
9	7.20	12.78	8:40	
10	7.54	17.61	8:45	New battery.
11	7.77	17.54	8:50	
Add 40.5 pCi/cm^2 of ^{238}U on filter paper (16 x 24 in^2)				
1	18.21	17.57	9:05 a.m.	
2	17.71	17.54	9:10	
3	20.75	17.50	9:15	
4	21.50	17.48	9:20	
5	18.56	17.45	9:25	
6	18.52	17.41	9:30	
7	17.93	17.38	9:35	
8	17.93	17.36	9:40	
9	18.26	17.33	9:45	
10	17.92	17.30	9:50	Determining concentration of NO$_3$H to dilute Pm^{147}.
11	17.91	17.27	10:05	
12	17.77	17.25	10:10	
13	17.98	17.22	10:15	
14	18.42	17.19	10:20	

Number	cps (Total)	Voltage	Time	Comments
15	18.15	17.16	10:25	
16	18.24	17.10	10:30	
17	17.76	17.06	10:35	
Break. Start again with no problem first count. New battery.				
18	17.87		14:45	
19	18.66	16.20	15:00	
Change to ^{90}Sr: 37.5 pCi/cm^2				
1	130.31	15.29	15:10	
2	131.06			
3	130.26	13.55	15:25	
4	129.84	12.91	15:30	
5	129.93	12.22	15:45	No batteries available (both charging).
6	--	15.99	16:30	New battery.
6	--	13.60	16:35	Counting aborted at 390 seconds.
	--		16:45	Counting aborted at 400 seconds
	--		16:55	
6	253.17	16.50	18:00	
7	200.90	16.19	18:05	
8	293.65	15.48	18:10	Detector does not behave; remove tray.
1	3.03	13.76	18:16	Counting background
2	7.18	12.35	18:21	
3	7.50	11.63	18:26	
9	290.48	15.88	18:35	Resume counting tray with ^{90}Sr.
10	290.12	14.63	18:40	

4/11/95

Number	cps (Total)	Voltage	Time	Comments
Start at 10:15 a.m.				
1		15.00	10:15	Detector stopped counting.
1	299.21	12.45	10:20	New battery.
2		15.07	10:25	Aborted at 340.
		12.54	10:41	Aborted at 484.
Too many problems with 37.5 pCi/sm^2 of ^{90}Sr that suggests detector does not behave accurately at that activity. Additionally, batteries discharge very fast as about 2V/5 min. We will remove the tray and replace it with other containing 373 pCi/cm^2 of ^{238}U. I believe that the counting is about 290 cps rather than 130 cps.				
Bkgd	7.28	11.35	10:50 a.m.	
Batteries charging. They discharge at higher rate than before in the same background scenario. Additionally, the counting must be aborted because it doesn't stop by itself. Let's leave the batteries charging at their highest possible voltage and resume counting again.				
Problems with one module.				
1	Aborted at 3965	17.33	12:30 12:35	New battery (17.40V)
2	6.74	16.82	12:45	
3	3.15	16.69	12:50	30 sec. Detector's stopped. Been disconnected from battery.
4	3.14		12:55	Disconnect and trying to awake the HVS by gently hitting them. Revise connection; keep cover away.
5	3.88	15.91	13:10	
6	3.00	15.09	13:20	
7	5.62	14.20	13:25	
8	7.57	13.67	13:30	
9				Replace cover.

Number	cps (Total)	Voltage	Time	Comments
9	3.45	12.90	13:40	
10				Remove cover.
11	7.47	11.50	13:45	New battery 17.30V.
12	224.36??	17.03	13:55	No stopped; background.
13	9.52	16.94	14:00	
14	9.35	16.86	14:05	
15	9.55	16.77	14:10	Detector is disconnected for a short time (10 sec.)
16	10.47	16.65	14:20	Stopped.
Some noise is causing the rise in the background counting.				
The filter containing 37.5 pCi/cm^2 of ^{90}Sr is put back again.				
1	299.41	16.51	14:25	It's in agreement with last set of measurements done before.
2	297.67	16.32	14:30	
3	301.81	16.03	14:35	
4	300.72	15.45	14:43	
5	300.37	15.00	14:48	
6	301.11	14.35	14:53	
7	284.67	12.50	15:00	
8				New battery 17.15V.
8	Aborted at 461 sec	16.70	15:08	
9	Aborted	16.54	15:15	
	Aborted	16.31	15:21	Disconnect detector from battery and connect it again.
8	300.80	15.68	15:30	
9	301.58	14.76	15:35	
10	299.20	14.02	15:40	

Number	cps (Total)	Voltage	Time	Comments
11	299.28	13.34	15:46	Move on to the next filter with 3.78 pCi/cm^2 ^{90}Sr.
Counting background.				
1	7.77	11:84	15:50	Consistent. (New battery 1710V)
Add the 3.75 pCi/cm^2 of ^{90}Sr.				
	Aborted at 611 sec			Disconnect and connect from batter.
1	19.49	15.24	16:15	
2	28.58	14.89	16:20	
3	25.30	13.99	16:26	
4	29.16	11.40	16:35	New battery (17.15 V)
5				Stopped.
5	17.82	16.17	16:40	
6	16.87	15.55	16:45	
Checking background to see whether this fluctuations are due to one of the modules not working.				
B1	5.71	13.60	16:50	Suggests that one module is in partial failure.
B2	3.28	11.40	16:55	
B3				New battery (16.40 V)
B3	3.68	14.33	17:15	
Battery discharged very fast. No battery available now. One is charging and the other is waiting.				

4/12/95

Start counting background with new battery (17.60 V)				
Number	**cps**	**Voltage**	**Time**	**Comments**
1	3.38	17.52	10:50 a.m.	Stopped
Remove cover and revise connections. Cover is kept away from detector.				
2	3.87	17.46	11:00	Stopped
3	aborted @ 890 sec	17.33	11:20	
4	aborted	17.28	11:25	
5	aborted			
6	aborted			
Change to betacon and sec results				
7	9.27	15.67	11:50	Cover on
8	9.01	15.07	12:00	Do beta
Replace filter containing 3.78 pCi/cm^2 of Sr^{90}				
1	23.90	14.57	12:05	Module 1 is not working
2	16.54	14.09	12:10	" " " "
3	17.86	13.76	12:15	" " " "
4	16.84	13.57	12:25	" " " "
5	16.59	13.48	12:30	" " " "
6	1.17	13.39	12:35	" " " " ; Module 2 was disconencted
7	16.54	13.30	12:45	" " " "; Module 1 only disconnected
8	16.45	13.22	12:57	
9	16.98	13.23	13:10	Stopped
10	15.33	12.87	13:15	Module 1 only
11	2.94	12.00	13:25	" " "
New Battery (17.04 V)				
Studying behavior of module 1 (Module 2 has been disconnected)				
1	225.08	17.35	13:30	#1
2	17.81	17.29	13:40	"

Number	cps	Voltage	Time	Comments
3	18.78	17.24	13:45	"
4	28.67	17.18	13:55	Both modules; #1 stopped
5	24.18	17.13	14:02	
6	18.88	17.08	14.07	Average of the accurate measurements is 28.8 cps
U^{238} filter with 373 pCi/cm^2				
1	50.17	17.02	14:20	
2	16.97	16.97	14:25	Module 1 only; stopped
3	52.63	16.89	14:30	Module 2 only
4	52.79	16.82	14:35	" " "
5	52.13	16.75	14:40	" " "
6	64.76	16.66	14:45	Module 1 only
7	65.04	16.57	14:50	" " "
8	116.00	16.45	15:05	Both modules
9	118.33	16.13	15.10	" " "
10	117.43			" " "
11	119.34	11.65	15:35	" " "
New battery (17.30 V)				
12	52.48	17.08	15:45	#1 failing again
9.89 pCi/cm^2 of Sr^{90}				
1	36.76	16.96	16:00	Both
2	36.21	16.89	16:05	Disconnect #1
3	36.89	16.74	16:15	
4	44.15	16.56	16:20	Disconnect #2
5	79.78	15.95	16:25	Both
6	80.27	15.12	16:30	"
7	81.29			
8	80.05	14.02	16:50	Both
9	79.85	13.49	16:55	" .

4/13/95

Number	cps	Voltage	Time	Comments
Rechecking activity of filter paper with 40.5 pCi/cm² of UNO₃				
1	8.01	12.66	13:25	#1 didn't work
2	0	12.41	13:30	#2 disconnected
3	0	12.22	13:40	" " "
4	0	11.90	13:45	" " "
New battery (17.20 V)				
5	0	16.80	14:00	
6	0	16.17	14:05	
7	0			
Experiments postponed until detector gets fixed				

It's been noticed so far that module #1 performs better than module #2 when it behaves. Some experimental data show:

9.88 pCi/cm² of ^{90}Sr

#1	#2	
44.15	36.21	⇒ 17%
	36.84	

3.78 pCi/cm² of ^{90}Sr

#1	#2	
17.81	16.54	⇒ 9%
18.78	16.45	

Detector sent to Richland.

4/19/95

Resume experiments again. Counting background.				
Number	**cps**	**Voltage**	**Time**	**Comments**
1	10.06	14.11	14:00	TRIGA (1 MW)
2	10.27	13.09	14:10	" " "
3	10.44	11.47	14:17	" " "
4	9.76	17.38	14:30	New battery
5	9.97	17.33	14:35	
6	10.09	17.28	14:40	TRIGA stopped at 15:15
We placed **4 sources of** ^{90}**Sr** (35 nCi as of 10/1/92)				
1	456.56	17.17	15:35	
2	449.58	17.12	15:40	
3	445.48	17.07	15:45	
4	442.91	17.02	15:50	
5	441.72	16.96	15:55	
^{90}Sr removed and counting background				
1	7.94	16.88	16:00	
2	7.88	16.72	16:10	
3	8.12	16.49	16:15	
Add 5 pCi/g of U sand (1500 cc of sand)				
1	11.95	15.98	16:20	
2	12.07	15.63	16:25	
3	11.80	15.45	16:35	
4	12.11	15.20	16:40	
5	12.24	15.00	16:45	
6	12.00	14.44	16:54	
7	11.75	12.05	17:00	
Average: 11.99 (before 13.15);New battery; back to ^{90}Sr sources				
8	aborted	18.17	17:07	
9	aborted	18.06	17:20	

4/20/95

Number	cps	Voltage	Time	Comments
New battery (18.80 V). ^{90}Sr source on.				
1	aborted	18.88	10:00	
2	aborted	18.87	10:15	
3	aborted	18.85	10:25	
Change the fuse. 4 sources of ^{90}Sr (35 nCi each)				
1	422.87	18.30	10:50	
2	421.34	18.25	10:55	
3	416.54	18.18	11:05	
4	412.73	18.14	11:10	
5	410.72	18.10	11:23	
6	411.34	17.98	11:28	TRIGA on at 11:14
Add 15 pCi/g of U sand				
1	17.46	17.90	11:35	
2	17.83	17.82	11:42	
3	17.67	17.66	11:47	
4	18.18	17.30	11:52	
5	17.73	16.79	11:59	
6	17.61	15.88	12:08	
7	18.19	15.05	12:15	
8	17.91	14.71	12:20	
9	17.56	14.54	12:25	
10	17.88	14.42	12:30	
11	18.14	14.37	12:35	
Average: 17.80 (before 17.33)				
1	10.65	14.36	12:40	Background; TRIGA on.
2	10.50	14.35	12:50	
Replace **4 Sources of ^{90}Sr**				
1	510.25	14.29	14:05	TRIGA off at 13:15

Number	cps	Voltage	Time	Comments
2	418.48	14.24	14:10	
3	416.02	14.19	14:15	
4	410.96	14.14	14:20	
5	409.36	14.10	14:25	
6	410.07	14.05	14:30	
Counting background				
1	8.22	13.99	14:42	
2	8.63	13.93	14:50	
3	8.58	13.85	14:55	
Add 35 pCi/g of U sand				
1	24.98	13.75	15:00	
2	24.55	13.62	15:05	
3	24.44	12.92	15:10	
4	24.41	11.25	15:15	
5	aborted	18.28	15:25	New battery (18.40 V)
6				
We are facing the same problem as yesterday when the battery was changed. This time we've disconnected the detector from the battery for 15 sec. and it worked.				
7	23.62	18.22	15:40	
8	23.66	18.18	15:50	
9	23.41	18.15	15:57	
10	23.09	18.10	16:10	
11	23.74	18.03	16:17	
12	23.25	18.05	16:25	
13	23.75	18.02	16:30	
14	23.72	18.00	16:35	
15	23.22	17.97	16:50	
Average: 23.83 (before 25.68)				

Eu-154

<u>5x10^{4}pCi/ml</u>

A new filter paper has been prepared containing a total activity of 1.1x10^6 pCi of ^{154}Eu

<u>1x10^5 pCi/ml:</u> 15.23 (0.1 N HCl) + 4.77 ml of solution containing ^{154}Eu
       Total activity: 1.5x10^6 pCi V_T = 15 ml
                (1x10^5 x V_T)

$$\frac{1.5 \times 10^6 \text{ pCi}}{2400 \text{ cm}^2} = 625 \text{ pCi/cm}^2$$

<u>2.4x10^4 pCi/ml:</u> 19.81 ml (0.1 N HCl) + 1.19 ml of solution with Eu-154

       Total activity: 3.6x10^5 pCi V_B = 21 ml (v_T = 15 ml)

$$\frac{5 \times 10^5}{2400} = 150 \text{ pCi/cm}^2$$

4/21/95

Start counting ^{154}Eu on filter paper (376.07 pCi/cm^2)
Total activity: 1.1×10^6 pCi $\Rightarrow \dfrac{1.1 \times 10^6}{18 \times 26}$ = 2300.427 pCi/cm^2
~ <u>376.07 pCi/cm^2</u>

Number	cps	Voltage	Time	Comments
1	167.62	17.88	16:18	
2	157.79	17.85	16:25	
3	159.22	17.82	16:30	
4	157.48	17.79	16:35	
5	156.38	17.74	16:45	
6	154.97	17.68	16:55	
7	154.93	17.64	17:00	
8	155.72	17.58	17:05	
9	153.88	17.52	17:10	
10	154.89	17.43	17:18	
11	153.30	17.29	17:25	
12	154.10	16.94	17:30	
13	153.97	16.25	17:35	
Background				
1	7.85	15.05	17:42	
2	7.74	14.44	17:48	
3	7.75	14.24	17:55	
4	7.59	14.08	18:02	

4/24/95

Counting Background				
Number	**cps**	**Voltage**	**Time**	**Comments**
1	7.36	18.12	11:30	
2	7.64	18.10	11:36	
3	7.72	18.09	11:45	
Counting ^{154}Eu in Filter paper $(1\times10^5$ pCi/cm^2 ~ 625 pCi/cm^2)				
1	261	18.08	11:55	
2	259.98	18.05	12:00	
3	259.21	18.03	12:05	
4	258.14	18.01	12:10	
5	256.34	17.80	12:45	
6	255.43	17.87	13:00	
7	257.19	17.83	13:08	
8	254.93	17.81	13:15	
9	255.57	17.79	13:20	
10	254.43	17.77	13:25	
11	254.41	17.75	13:30	
12	255.58	17.74	13:35	
13	252.18	17.71	13:40	
14	254.79	17.69	13:45	
15	254.51	17.67	13:50	
16	255.45	17.65	13:55	
17	253.22	17.64	14:00	
18	254.01	17.61	14:13	
Counting Filter Paper containing Eu-154 $(3.6\times10^5$ pCi ~ **150 pCi/cm^2**)				
1	115.63	17.59	14:25	
2	116.44	17.56	14:30	
3	115.72	17.54	14:35	
4	115.40	17.51	14:45	

Number	cps	Voltage	Time	Comments
5	116.48	17.48	14:50	
6	114.36	17.46	14:57	
7	113.59	17.44	15:03	
8	115.98	17.41	15:10	
9	116.71	17.39	15:15	
10	116.05	17.37	15:20	
11	115.89	17.34	15:25	
12	115.63	17.30	15:35	
13	115.56	17.27	15:40	
14	115.32	17.24	15:45	
15	116.14	17.21	15:50	
16	114.81	17.18	15:55	
17	115.77	17.16	16:06	
18	115.46	17.12	16:12	

Preparing Cs-137 Samples:

2.5×10^4 pCi/ml

5 ml (stock solution) + 10 ml (0.5 N ClH) = 20 ml

0.65 $\times 10^6$ pCi in 5 ml
2.5×10^4 pCi/ml x 15 ml = 4.88×10^5 pCi → 203.13 pCi/cm^2

1.64×10^4 pCi/ml of Cs-137

1.64×10^4 pCi/ml x 20 ml = 3.28×10^5 pCi/ml → 2.5 ml of stock solution

2.5 ml + 17.5 = 20 ml → 1.64×10^4 x15/2400 = 102.5 pCi/cm^2

Next filter paper with Cs-137 (4.88×10^5 pCi ~ 203.2 pCi/cm^2)				
Number	cps	Voltage	Time	Comments
1	63.74	17.07	16:20	
2	62.60	17.03	16:28	
3	64.45	17.00	16:35	

Number	cps	Voltage	Time	Comments
4	61.99	16.96	16:40	
5	62.73	16.92	16:45	
6	62.94	16.87	16:50	
7	62.02	16.82	16:55	
8	62.15	16.77	17:00	
9	62.85	16.68	17:05	
10	62.64	16.59	17:15	
11	63.46	16.42	17:20	
12	61.92	16.06	17:25	
13	62.81	15.65	17:30	
14	63.66	15.45	17:35	
15	63.38	15.29	17:40	
16	63.37	15.13	17:45	
17	63.23	15.01	17:55	
18	63.02	14.77	18:00	
19	63.08	14.36	18:08	
Adding filter paper **containing Cs-137** (2.46×10^5 pCi - **102.5 pCi/cm^2**)				
1	26.82	11.04	18:15	
2	26.22	17.74	18:35	New bottom
3	27.00	17.68	10:30	**(4/25/95)**
4	30.31	17.65	10:37	
5	29.75	17.62	10:42	
6	29.27	17.59	10:50	Main battery
7	28.71	17.56	10:55	" "
8	29.64	17.51	11:00	" "
9	28.55	17.46	11:05	" "
10	28.44	17.42	11:10	" "
11	27.88	17.30	11:15	" "
Detector stopped operation itself.				